Study of structure of unstable nuclei with nuclear moments

博士論文

Study of Structure of Unstable Nuclei with Nuclear Moments
(核モーメントを通じた不安定核の構造の研究)

島田 健司

平成 26 年

Doctoral Thesis

Study of Structure of Unstable Nuclei with Nuclear Moments (核モーメントを通じた不安定核の構造の研究)

Kenzi Shimada

November 2014

Cyclotron and Radioisotope Center,
Tohoku University

980-8578 Aoba, Aramaki, Aoba-ku, Sendai, Miyagi, JAPAN
Phone: 022-795-7794
Telefax: 022-795-7997
E-Mail: shimada@cyric.tohoku.ac.jp

Study of Structure of Unstable Nuclei with Nuclear Moments
(核モーメントを通じた不安定核の構造の研究)

Kenzi Shimada

November 2014

Abstract

Nuclear moments are nuclear observables which are genuinely independent of models for nuclear structure and yet sensitively dependent on the way of occupation of valence orbits by nucleons. Thus, they carry key information on the nuclear structure. Precise measurement of the nuclear moment for a wide variety of nuclei requires slow or stopped radioactive isotopes (SSRI) with their spins polarized. In the present study, therefore, the following four subjects are pursued:

- A model experiment where some nucleus in the region far from stability is produced, spin-polarized and subjected to a nuclear moment measurement aiming at the nuclear structure study: a study of change of nuclear structure in the *island of inversion*. The ground-state electric quadrupole moment of ^{33}Al is measured by β-NMR spectroscopy, using projectile-fragmentation reaction as a means to polarize the ^{33}Al spin.
- The method for production of SSRI: a study to improve technique of the ion-guide isotope separator on-line (IGISOL) is made.
- New method for measuring magnetic moment of the unstable nuclei: the atomic beam resonance method for SSRI is studied.
- A method to produce spin polarization using low-energy nucleon-transfer reaction: a low-energy spin-polarized ^{17}N via the inverse-kinematic reaction is discussed.

■Erosion of $N = 20$ shell in ^{33}Al investigated through the ground-state electric quadrupole moment Electric quadrupole moment Q of the ^{33}Al ground state has been measured by means of β-NMR spectroscopy using a spin-polarized ^{33}Al beam produced in a projectile fragmentation reaction. The obtained Q moment, $|Q_{\mathrm{exp}}(^{33}\mathrm{Al})| =$

132(16) $e$mb, shows a significant excess from the prediction of shell model calculations within the *sd* shell. The result indicates sizable admixing of *pf* intruder configurations in the ground state, demonstrating that the $N = 20$ shell closure certainly erodes in ^{33}Al, a nucleus located on the border of the island of inversion. Comparison was made with predictions of the Monte Carlo shell model, and also a particle-vibration coupling model treating the neutron pairing correlations in the ground state of ^{33}Al. Again, a significant admixture of *pf* intruder configurations to the ^{33}Al ground state was needed in the both theoretical approaches to explain the observed large Q.

■Development of ion-guide isotope separator on-line The Ion-Guide Isotope Separator On-Line (IGISOL) has been developed. It is a kind of ISOL specialized for unstable nuclei having short half-lives (≤ 0.5 s) and high melting temperatures (≥ 1000 K). Using the IGISOL and a conventional fast-slow coincidence method with a high-purity germanium detector and a BaF_2 detector, a half-life of an 163.82-keV excited state in ^{105}Ru was measured to be 18.0(5) ns. Its error was reduced to one sixth of the previous one. Additionally, in order to improve a mass resolving power (MRP) and yields of unstable nuclei, a sextupole ion-guide (SPIG) has been installed after the exit hole of the gas cell. The SPIG improves the vacuum around the acceleration stage of the separator, focuses the extracted ions scattered by collisions with residual molecules, and then reduces the energy spread of the extracted ions. Consequently, MRP in fwhm improved from 100 to at least 260.

■Development of atomic beam method for unstable nuclei Atomic Beam Resonance method for Radioactive Isotope (RIABR), we have been developing, is extended application of the Rabi resonance method to the unstable nuclei. Here we report development of the RIABR device consisting of an atomic beam source including a stopping cell and a neutralizer, a sextupole magnet, the NMR section including a RF cavity and a dipole magnet, a quadrupole magnet, and a RI detection device. Especially, development process of the atomic beam source of the thermalized and neutral unstable nuclei is reported in detail, due to the most important part of the RIABR device.

■low-energy spin-polarized ^{17}N New scheme of producing spin-polarized RI ^{17}N via the inverse-kinematics reaction has been developed for application of the spin-polarized RI beam to condensed matter physics including impurity and electronic dynamics in semiconductors. The ^{17}N beam was produced by bombarding a thin Be target with ^{18}O having energy beam of 7.0 AMeV and intensity of 240 pnA. Next, the spin polarization was measured with β-NMR by selecting it emission angle and momentum using the CRIB. A result obtained absolute polarization equal to 0.4 %, which looks like rather small. The calculation according to the Brink's matching condition shows the possibility to rise $|P|$ as the energy of the primary beam increases.

As described above, the nuclear moment is one of the most fundamental physical quantities revealing the nuclear structure. The production method of the SSRI leads to technique of the most precise measurement using the stopped unstable nuclei. Thus,

it is important development as well as the experiment with the in-flight method vigorously developed in recent years. The precise measurement of the nuclear structure with the SSRI is one of the best experimental candidate bringing out the microscopic collective system of the many-body system of the nucleons.

Study of Structure of Unstable Nuclei with Nuclear Moments (核モーメントを通じた不安定核の構造の研究)

島田 健司

2014 年 11 月

論文概要

原子核は陽子と中性子から成る二成分フェルミ粒子の少数多体系であるという意味でユニークであると共に，実験的にも崩壊を利用した分光や反応の運動学を駆使したさまざまな微視的計測技術が適用できる研究対象でもある．また，加速器を用いた核反応によって生成した中性子過剰な不安定核の研究では，軽核領域において，安定核では見ることのできない中性子ハロー核や魔法数の消失など画期的な事実が姿を現わした．このようなの安定領域から離れるにしたがって露わになってきた新しい原子核の様相は，単一粒子軌道の順序の入れかわりなど，核の微視的構造の根本的変化を示唆する．そこではバレンス核子がどの単一粒子軌道を占めるかなど，核構造模型に依存しない物理量である核モーメントが提供する情報が本質的に重要な役割を演ずると考えられる．

そこで本研究では不安定核の核モーメントの測定とそれに不可欠な偏極ビームの生成を中心に据えて，

- 入射核破砕反応と β 核磁気共鳴法 (β-NMR) を用いた逆転の島における核構造の変化の研究，すなわち ^{33}Al の基底状態の電気四重極モーメントによる $N = 20$ 殻の侵食の検証，
- 不安定核の生成のための高周波イオンガイド型オンライン同位体質量分離装置の改良，
- 核モーメント測定法である原子線共鳴法の不安定核への応用，
- 逆運動学核子移行反応を用いた低速高偏極ビーム生成法の開発

を行った．

■^{33}Al の基底状態の電気四重極モーメントによる $N = 20$ 殻の侵食の検証　原子核の磁気モーメントと電気四重極モーメントにはそれぞれ核子の配位と $E2$ 集団運動性が反映されており，これらを系統的に測定することにより，核子数に依存した核構造の変化や発展を追うことが可能である．また，β-NMR は放射性同位体 (RI) の核モーメントの測定方法である．不安定核が β 崩壊の際に放出する β 線の角度分布はスピンの方向に依存しているため，スピン偏極した RI からの β 線はその分布に偏りを持つ．β-NMR では結晶中に打ち込

んだスピン偏極した RI に対し高周波 (RF) を照射し，それと同時に β 線の分布の変化を検出することにより NMR を判別する手法である．これにより，共鳴周波数を決定することが可能となり，すなわち核モーメントを決定することが可能となる．また，入射核破砕反応では in-flight で RI の分離することが可能であるため，β-NMR の原理的な適用下限である 1 ms オーダーを下回る非常に短寿命な不安定核まで生成可能である．2 次ビームの放出角度分布と運動量分布には反応経路の情報が含まれているため，これらを適切に選択することにより，特定の反応経路を経て生成された不安定核を選択的に収集することできる．このような不安定核ビームは大きくスピン偏極することが期待される．

本研究では Al 同位体の基底状態の核モーメントを系統的に比較し，その核構造の変移を調べるため，β-NMR 法を用いて ^{33}Al の電気四重極モーメントを測定した．核図表上において Ne, Na, Mg の同位体で中性子数が魔法数である 20 を持つものの近傍は “逆転の島” と呼ばれている．安定核領域では殻構造における *sd* 殻が埋まったあと *pf* 殻に属する軌道へと中性子は配位されていくと考えられていたが，ここでは *pf* 軌道のエネルギー準位が下り *sd* 殻へと侵入しているがために準位の逆転や混合が起っているものと考えられる．Al の同位体は逆転の島の境界に位置しており，これを用いて核構造の変化を追った．その結果，^{33}Al の基底状態においてかなり大きな軌道の混合が起っていることが示唆された．これは $N = 20$ の閉殻構造が ^{33}Al にて壊れかかっていることを示している．また，モンテカルロ殻模型による理論値と粒子–振動模型による理論値との比較からも同様の結果を得た．

■高周波イオンガイド型オンライン同位体質量分離装置の改良　開発中の高周波イオンガイド型オンライン同位体質量分離装置 (RF-IGISOL) は他の手法では生成の難しかった中性子過剰な中重核領域に属する短寿命で高融点元素の不安定核をオンラインで迅速に分離し，測定系へ輸送する事が可能とする装置である．最終目標はこれを用いて，より多くの原子核を対象に系統的な物理量の測定行い，理論を構築・補正するためのデータを蓄積することである．

IGISOL を用いた実験の概要を述べる．不安定核の生成には加速された陽子ビームとウラニウム・トリウム標的による核分裂反応を用いる．標的は 3 kPa の He が充填された大容量のガスセルの中に設置されており，反跳により標的から放出された不安定核はこのなかに広がって停止し，熱化される．この際に He はイオン化ポテンシャルが最も高い元素であるため，不安定核はそれと衝突してもイオンのままでいることが期待される．このような熱化されたイオンを RF-IGISOL では静電場と RF 電場を用いて，ガスセルの壁へと衝突させずに，出口穴へ輸送し，真空領域へ引き出す．この後，差動排気された静電加速領域を通過させることにより，30 keV エネルギーを持つビームを形成する．これにより磁場を用いた運動量分析を行うことが可能となり，単一の質量数をもつ不安定核だけを分離し，標的から離れた場所へ迅速に輸送することが可能になる．また，低バックグラウンドな環境にて γ 線摂動角相関法（γ-PAC）や交差偏極移行法，原子線共鳴法を用いて寿命が 1 秒以下の不安定核の核磁気モーメント測定を行うことができる．

我々の IGISOL の特徴としてはガスセルが従来のものに比べて 1000 倍も大きいことがあげられる. これにより，より多くの不安定核を He ガス中に停止することができるようになったが，従来のようにガスの流れだけでは効率良く引き出すことが難しくなったため，静電場や RF 電場を印加するための電極が必要となった．このため構造が非常に複雑であることも特徴の一つである．

最近の IGISOL を用いて実施された実験のひとつに ^{105}Ru の 163.82 keV の準位の半減

期測定がある．IGISOL により質量分離した ^{105}Tc を用いて，高純度 Ge 検出器と BaF_2 で fast-slow coincidence 法により半減期を測定した．その結果 18.0(5) ns を得た．この誤差は Holland によって報告されている値の 1/6 に改善された．また Holland に倣い，pairing-plus-quadrupole 残留相互作用を考慮した半経験的殻模型による値と比較をした．結果は Holland の主張を支持するものであった．

さて，PAC 法による磁気モーメントの測定手法を確立するためには 10^4 cps 以上の RI の収量が必要となるが，現状では多い RI でも 10^3 cps であり強度が足りない．よって，改良が必要となった．収量増加のための一つの解として質量分解能の向上が挙げられる．現在の分解能 $M/\Delta M$ は 100 程度である．これは焦点面での分散の広がりととらえることもでき，事実，測定位置までの輸送効率は 25 % 程度である．電場の強さと収量はある閾値まで比例するが，一方で電場の強さと分解能は反比例する．このため，分解能を犠牲にしながら閾値を越えるような電位を印加する必要がある．これは RI イオンが高圧ガスセルの出口穴から真空領域へ引き出され，電場にて加速される際に，残留ガスとの衝突により散乱する，もしくは運動エネルギーの分布の幅が広がるためである．これを解決するためには排気能を向上し，残留ガスが残るような領域を短くすること，そして，そのような領域に印加する電位を小さくすることが必要である．そのために高周波六重極イオンガイド (SPIG) を導入した．SPIG は 6 本のロッドに交互に逆位相の RF を印加することにより，方位角方向の閉じ込め電場を形成する．これによりイオンを低い電位で出口穴から引き出し，拡散することなく高真空な領域まで輸送し，残留ガスと衝突させることなく加速させることが可能となった．また出口とスキマーの間隔が広がることから差動排気領域のコンダクタンスが大きくなるため，ガスセルの He 気圧を大きくすることが可能となる．これはターゲットから反跳で放出される RI をより多く He ガス中に停止させることを意味しており，これも収量の増加へつながる．また，分解能の向上は RI ビームの純度の改善を意味するため，S/N の良い測定を行うことも可能になる．

開発の進度としては，SPIG の導入することにより，ガスセル中へ混合した Xe ガスを用いたオンライン実験により $M/\Delta M$ は 260 以上となり，質量数 130 程度の粒子に対しても単一アイソバービームをビームライン末端まで輸送することができることを確認した．一方で RI ビームに関しては未だ引き出しを確認できていない．原因のひとつとして RI がガスセル中で熱化する際に H_2O などと複合分子イオンを形成し，いくつかの質量へ分散してしまったことにより，質量分析後の収量が減った疑いがある．また，ガスセル中で出口穴へとドリフトする際に不純物との衝突により中性化することはスキマーシステムでも同様であったが，これが SPIG 導入の際にガスセル内に意図しない変更が起こり，これによりスキマーシステム時よりも中性化の確率が上ってしまった可能性がある．

■不安定核を対象とする原子線共鳴法の開発　原子線共鳴法は I.I. Rabi によって開発された電磁モーメントの測定法である．これまで安定線近傍の核種に適用されてきたが，そこから離れた不安定核に適用された例は非常に少ない．そこで本研究では入射核破砕反応を用いた不安定核ビームへ原子線法を適用するための装置，及び実験手法の開発を行った．

原理的には装置はまず低速ビーム生成装置，その下流に設置した 2 つ並べた磁場勾配，その間に設置した超微細共鳴装置，そして最下流に設置した検出器からなる．磁場勾配を通過する際に受ける力はスピンの大きさに比例するため，低速ビーム生成装置から放出された原子は二つの磁場勾配を通過する際にスピン状態ごとに軌道が変化する．その結果，あるスピン方向を持った原子だけが検出器によって計数される．ここで共鳴部にて共鳴が起こり，ス

ピン状態が変化し，その向きがフリップすると，二つ目の磁場勾配を通過する際の軌道に変化が起り，検出器まで到達する原子の数が変化する．このように計数の変化により共鳴の有無を感知することができる．磁場勾配の形状と検出器の位置を適切なものに換えると共鳴を起したものだけを集めることが可能になり，これにより高偏極ビームを生成することも可能となる．

原子線法装置の開発状況としては，非均一磁場生成のための磁石の開発と真空槽の作成といった大枠は完了した．そして，本装置の前半にあたる破砕片停止 · 収集 · 引き出し部の開発を主に進め，約 0.2 % の効率で収集 · 真空部への引き出しが可能であることがわかった．

今後の展開としては，入射核破砕片を利用した低速ビームの生成法は我々の開発した装置では効率が低く，また，研究開始当時に比べて加速器を用いた研究を取り巻く環境が変化したため開発のためのオンライン実験の機会を得ることも難しい．これを用いて原子線法の開発を行うことは非常に困難である．そこで，不安定核源を IGISOL へと変更し，研究をすすめる準備を行っているところである．

展望として本手法の学術的な特色・独創的な点及び予想される結果と意義を述べると，低エネルギー不安定核ビームの核スピンを偏極させるというのは新規のアイデアで，これが実現できれば基本的対称性に関わるような基礎物理，核構造研究，表面・界面物理など幅広い応用が期待できる．例えば β-NMR では原理的に次のような不安定核には適用できないが，原子線共鳴法を利用した測定法ではこれらの困難は全て克服できる．1. β 崩壊しない，2. β 線のエネルギーや β 線の角度分布の非対称度，偏極度が非常小さい，3. 固体中でのスピン緩和時間が短く，もしくは寿命が長く，崩壊するまでの間偏極を維持できない．

また、対称性の研究においては大きくスピン偏極した放射性原子核自体の存在が無かったため，それ自体ブレークスルーになる．例えば，真空中や希薄気体中，または飛行中のスピン偏極した放射性核が β 崩壊する際の反跳核と β 線のエネルギーと角相関を効率良く測定することが可能となる．これにより，時間反転対称性の破れなどの基礎的な物理学の研究にインパクトを与えることができると考えられる．

結晶成長過程における表面・界面の構造の研究への不安定核の応用としては μSR 法や γ-PAC などが挙げられるが，偏極ビームにより γ-PAC より格段に感度の良い β-NMR を利用することが可能になる．また使用する核種の選択もそれに比べ大幅に増加し，結晶構成元素の同位体を利用することにより希望の結晶位置へ置換させることができるため，従来の研究をさらに発展させる可能性がある．

■逆運動学反応による低エネルギー偏極 ^{17}N ビームの生成　これまで挙げた研究は核モーメントの測定を通して原子核構造を研究するためのものであったが，この研究はそれの物性物理への応用を見据えたものである．核磁気共鳴の条件は核モーメントとそれが感じる電磁場に依存するため，既知の核モーメントをプローブとすることにより未知の結晶構造の局所的な電磁場を決定することができる．このような研究では様々な条件下で測定を行い，その変移を追うため，一つの条件を短時間で測定できなければならない．そのためには高偏極かつ高純度，高収量なビームが必要となる．

さて，本研究では核子移行反応における逆運動学反応を用いた効率の良い偏極ビーム生成法の確立を目指した．逆運動学反応では出射核の分布が実験室系で前方に集中するため，高い収率が見込まれるのみならず，質量分析器を通過させることにより，純度の高いビームが得られる．加えて，核標的から離れた場所へ生成したビームを輸送できるため，S/N の良い実験ができる．2 次ビームの放出角度分布と運動量分布には反応経路の情報が含まれている

ため，これらを適切に選択することにより，特定の反応経路を経て生成された不安定核を選択的に収集することできる．このような不安定核ビームは大きくスピン偏極することが期待される．

実験は CNS の低エネルギー不安定核ビーム分離装置 CRIB を用いて行った．^{9}Be(^{18}O,^{17}N) 反応によって生成した ^{17}N に対し出射角の依存性を測定した結果，実験室系の -0.6~$-0.28°$ において，$-0.53(13)$ % の偏極度を得ることに成功した．このときのビーム強度は 10^5 cps であった．

得られた偏極は似かよった順運動学の核子移行反応から生成したスピン偏極に比べて偏極が非常に小さい．偏極度を大きくするためにはさらに入射エネルギーの依存性を調べる必要があると考えられる．

■ 以上で述べたように，核モーメントはその値が核構造模型を決定する最も基本的な物理量である．ここで述べた IGISOL や SPIG, そして理研で開発されている SLOWRI や PALIS などの低速不安定核ビームを生成する技術は対象となる不安定核を停止した状態で精密に測定することを可能とする技術へとつながるため，現在急速に発展した in-flight での実験と同様に重要な開発課題である．低速・停止不安定核 (Slow Stop RI, SSRI) による原子核構造の超精密測定は核子多体系という微小世界での集団系の解明に向けた扉のひとつでもある．

Table of Contents

Chapter 1

Introduction

1.1 Study of structure of unstable nuclei

A nucleus is an unique physical entity that represents a many-body system of strongly interacting fermions consisting of protons and neutrons. Furthermore, it is an attractive subject of study which incorporates microscopic measurements, such as α-, β- and γ-spectroscopy and nuclear reactions. The studies of light-mass neutron-rich unstable nuclei have revealed their exotic nature, *e.g.* formation of the neutron halo, disappearance of the conventional magic numbers and appearance of the new magic numbers. Such information on the nuclei far from the β stability indicates essential change of a microscopic nuclear structure, *e.g.* intruder configurations from the upper orbits. Nuclear moments are dependent on occupation of valence orbits by nucleons, as well as quantities independent of the nuclear structure models. Thus, their information plays important roles in the study of nuclear structure.

Precise measurement and wide application of the nuclear moment require Slow or Stopped Radioactive Isotopes (SSRI). The production method of SSRI, such as the Ion-Guide Isotope Separator On-Line (IGISOL) that we have been developed at CYclotron RadioIsotope Center (CYRIC) located in Tohoku University, and the slow radioactive nuclear ion beam facility (SLOWRI) and the PArasitic Laser Ion-Source (PALIS) developed in RIKEN [1, 2], leads to technique for the most precise measurement using slow or stopped unstable nuclei. Thus, it is important development as well as the experiment with the in-flight method vigorously developed in recent years, such as the projectile fragmentation at RIPS [3] and the in-flight fission at BigRIPS [4] in RIKEN. The precise measurement of observables embodying the nuclear structure is one of the best experimental strategies bringing out the microscopic collective aspects of the many-body system of nucleons.

1.1.1 Known nuclear moments

Nuclear magnetic dipole and electric quadrupole moments are sensitive respectively to nucleon configuration and to $E2$ collectivity. Thus, systematic studies of nuclear moments can reveal the evolution of the nuclear structure.

Figure 1.1 shows known magnetic moments of ground and excited states taken from the compilation by Stone [5]. Most of known nuclear moments, that are not only magnetic moments but also electric quadrupole moments, belong to light-mass,

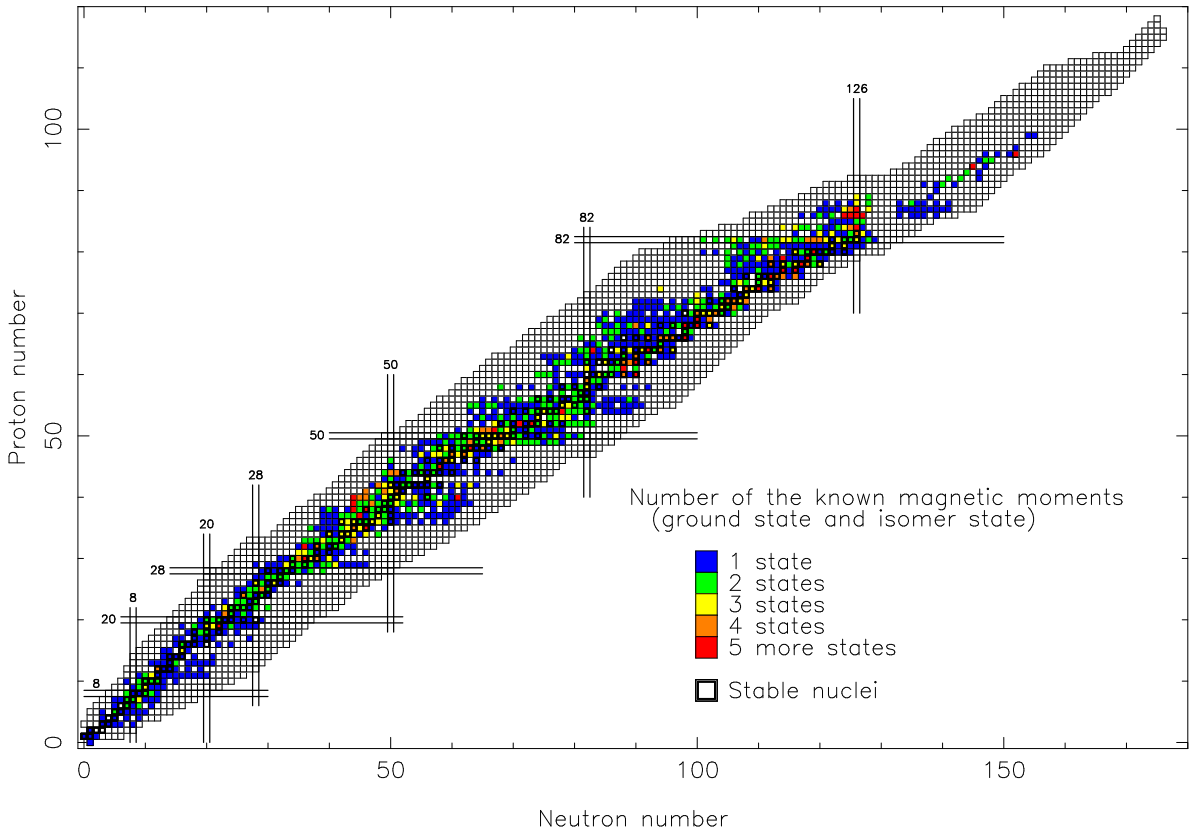

Fig. 1.1 Known magnetic moments of ground state and excited state. The data were taken from the compilation by Stone [5].

alkali, alkaline-earth, heavy-mass proton-rich, mirror or stable nuclei.

Recently, we have been paying attention to two blank regions in the neutron-rich side of the nuclear chart presented in Fig. 1.1.

The first region is the region of nuclear chart which consists of neutron-rich Ne, Na, and Mg isotopes around the neutron number $N = 20$, known as the *island of inversion*, where the nuclear ground states are dominated by intruder configurations from the upper *pf* orbits and are known to be considerably deformed [6].

The second is the A =100–130 region, where ^{132}Sn is known to be spherically shaped due to the double-closed shell while ^{100}Zr is to be strongly deformed, though the difference in proton number between Sn and Zr is only ten. Thus, neutron-rich Ru and Rh isotopes located in a region between Zr and Sn would be right in the middle of transition in nuclear structure, that would appear as a phenomenon of the shape-coexistence in low-lying states [7, 8].

1.2 Study of unstable nuclei with nuclear moments

1.2.1 Application of in-flight method with high-energy beam: electric quadrupole moment of ^{33}Al and border of *island of inversion*

Three contradictory results are reported as for ^{33}Al belonging to a border of the *island of inversion*. One is the μ-moment measurement of the ground state [9], where it is suggested that the mixture of *pf* intruder configurations could explain an observed difference, $\Delta\mu(^{33}\mathrm{Al}) = 3.9\,\%$, between the experimental $\mu(^{33}\mathrm{Al})$ moment and a shell-model calculation within the *sd* model space. Second is the β-γ spectroscopic work [10], which indicates that the observed β-decay properties of ^{33}Al are well described by the sd shell model calculations, suggesting that the ground state of this nucleus lies primarily outside of the *island of inversion*. Contrary to this, finally, the β-decay study [11] indicates a sizable admixture of intruder configurations in the ^{33}Al ground state.

It would be worth noting here that, although most of theoretical analyses of the nuclear structures arising in the *island of inversion* are based on the consideration of strong nuclear deformations [12, 13], the possibility of other mechanisms may also be important. For instance, the importance of the neutron pairing correlation instead of nuclear deformation [14] and a picture of quadrupole-shape fluctuations which dominate both the ground and the excited $I^\pi = 0^+$ states [15] were proposed to describe the ^{32}Mg nucleus.

In the present work [16], the ground-state Q moment of ^{33}Al has been measured by means of β-ray-detected nuclear magnetic resonance (β-NMR) [17] with incorporation of the technique of fragmentation-induced spin-polarized radioactive isotope beams [18, 19]. Comparing the obtained $Q(^{33}\mathrm{Al})$ with those reported for other neutron-rich aluminum isotopes, possible evolution of nuclear structure around ^{33}Al will be signified due to its high sensitivity to the collectivity such as deformation and paring correlation. Details are given in Chap. 2.

1.2.2 Advance of nuclear-moment experiment: more precise, more applicable

Production of Slow or Stopped Radioactive Isotope (SSRI): Ion-guide Isotope Separator On-line

The Ion-Guide Isotope Separator On-Line (IGISOL) is a kind of the ISOL specialized for unstable nuclei having shorter half-lives (≤ 0.5 s) and higher melting temperatures (≥ 1000 K) [20, 21]. The principle of IGISOL is the following: radioactive ions recoil out of the thin target after the nuclear reaction, and are thermalized in a helium buffer gas after many collisions. These ions are transported out of the target chamber by a helium flow, and guided into the mass separator by an electric field.

The radio-frequency ion-guide type ISOL has been developed in CYRIC located at Tohoku University, named "Tohoku RF-IGISOL". It has following unique properties: 1) the nuclear reaction is a proton-induced fission of a thin uranium target, 2) a volume of the gas cell is larger and a pressure of the helium gas filling the target chamber is higher than a conventional IGISOL in order to enlarge an acceptable range of recoiled fragments, and then 3) a combination of DC and inhomogeneous RF electric fields are applied to collect recoiled fragments to an exit hole of the gas cell [22–25].

Using Tohoku RF-IGISOL, some experimental programs have been carried out, such as measurements of g-factor of the 225.98-keV excited state in ^{109}Rh [24], the half-life and the magnetic moment of the 49.72-keV excited state in ^{132}I [26], and the half-life of the 163.82-keV excited state in ^{105}Ru described in Chap. 3.

Chapter 3, additionally, explains a improvement of Tohoku IGISOL. In order to improve a mass resolving power and yields of unstable nuclei, a SextuPole Ion-Guide (SPIG) [27] has been installed after the exit hole of the gas cell. The SPIG improves the vacuum around the acceleration stage of the separator and reduces the energy spread of the extracted ions. Consequently, the mass-separated ions are well focused at a measuring device, and the RI ions employed to the measurement increase.

Application of SSRI: Atomic beam method for unstable nuclei

A number of nuclear moments have been measured by using spin-polarized Radioactive Isotope (RI) beams from the projectile-fragment reaction combined with the nuclear magnetic resonance *via* change in the angular distribution of β-rays (β-NMR method). This approach, however, requires several conditions to be fulfilled. One

is to find a suitable host material in which the spin polarization of the implanted RI can keep long enough, since the spin relaxation time is very sensitive to the chemical properties of combination of an implanted atom and the host material. Another important factor is degree of the β-ray asymmetry parameter which largely determines the performance of the measurement.

To overcome the difficulties forecasted in such requirements when the measurements of the nuclear moments are extended to the heavier mass region, we attempt to develop a new method which involves a low-energy spin-polarized RI beam, named the Atomic Beam Resonance method for RI (RIABR). This method is extended application to the unstable nuclei of the Rabi resonance method [28–30]. This has an advantage that neither special host material nor a large β-ray asymmetry is required, since the magnetic resonance is performed in-flight and the resonance is detected simply *via* change of a position of the unstable nuclei reaching at the end of the apparatus. Chapter 4 describes a development of the RIABR apparatus in detail.

Development of production method of low-energy spin-polarized ^{17}N via inverse-kinematics reaction

An application of spin-polarized RI beam is not only nuclear physics but also condensed matter physics including magnetism in metals and insulators, impurity and electronic dynamics in semiconductors, and superconductivity. In addition, the spin-polarized RI beam may even be an exclusive tool to investigate surfaces, layers and nano-sized structures, if energy and spatial distribution (spot size) of the beam can be controlled with sufficient precision. Production of the RI beam via inverse-kinematics reactions may be one of the most appropriate methods to obtain such spin-polarized RI beams. In the low-energy nucleon-transfer reaction, selection in both the recoil angle and the a kinetic energy of the product nuclei may bring a spin polarization to the RI beam. In the inverse-kinematics arrangement, the distribution in the recoil angle in the normal kinematics shows up as a sharply focused angular dispersion of the RI beam, and thus facilitating a very efficient transportation of the RI beam. Yet, the narrow but finite widths of the angular and energy distribution of the RI beam preserve the memory of the recoil angle and energy, and consequently, by selecting a certain region of emission angles and energies of RI beam, the RI beam will be spin-polarized. In addition, in the inverse-kinematics arrangement an in-flight mass separator could be available, and it provides separation based on momentum

analysis and facilitates formation of a well-focused RI Beam. Therefore, new scheme of producing low-energy spin-polarized RI beam via the inverse-kinematics reaction has been developed, as given in Chap. 5.

Part I

Application of In-flight Method using High-energy Heavy Ion Beam

Chapter 2

Erosion of $N = 20$ Shell in ^{33}Al Investigated through Ground-state Electric Quadrupole Moment

2.1 Introduction

The region in the nuclear chart consisting of neutron-rich Ne, Na, and Mg isotopes around the neutron number $N = 20$ is known as the *island of inversion*, where the nuclear ground states are dominated by intruder configurations from the upper *pf* orbits and are considerably deformed [6]. Among the $N = 20$ isotones, numerous studies have been conducted for nuclei inside the *island of inversion* [6, 31–35], but not much effort has been devoted to their neighbors, such as ^{33}Al. In the systematic mass measurements around $A \simeq 32$ [12, 13], from which the anomalously tight binding of nuclei in this region was recognized, no remarkable feature was found for ^{33}Al [36, 37].

Nuclear magnetic dipole (μ) and electric quadrupole (Q) moments are sensitive respectively to the nucleon configuration and to the $E2$ collectivity. Recently, the μ-moment measurement of the ^{33}Al ground state has been reported [9], where it is suggested that the mixing of *pf* intruder configurations could explain the observed difference, $\Delta\mu(^{33}\mathrm{Al}) = 3.9\,\%$, between the experimental $\mu(^{33}\mathrm{Al})$ moment and a shell-model calculation within the *sd* model space. This observation contradicts a β-γ spectroscopic work carried out on ^{33}Al [10], which reports that the observed β-decay properties of ^{33}Al are well described by the *sd* shell model calculations, suggesting that the ground state of this nucleus lies primarily outside of the *island of inversion*. Contrary to this, a β-decay study [11] indicates a sizable admixture of intruder configurations in the ^{33}Al ground state.

It would be worth noting here that, although most of theoretical analyses of the nuclear structures conducted for nuclei in the *island of inversion* are based on the consideration of strong nuclear deformations [12, 13], the possibility of other mechanisms may also be important. For instance, the importance of the neutron pairing correlation instead of nuclear deformation [14] and a picture of quadrupole-shape fluctuations which dominate both the ground and the excited $I^\pi = 0^+$ states [15] were proposed to describe the ^{32}Mg nucleus.

In the present work [16], the ground-state Q moment of ^{33}Al ($I^\pi = 5/2^+$, $T_{1/2}$= 41.7(2) ms) has been measured by means of β-ray-detected nuclear magnetic resonance (β-NMR) [17] with incorporation of the technique of fragmentation-induced spin-polarized radioactive isotope beams [18, 19]. Comparing the obtained $Q(^{33}\mathrm{Al})$ with those reported for other neutron-rich aluminum isotopes, possible evolution

of nuclear structure around ^{33}Al will be signified due to its high sensitivity to the collectivity such as deformation and paring correlation. So far, the μ moments of $^{30-34}$Al [9, 38–40] and the Q moments of ^{31,32}Al [41–43] have been measured.

2.2 Experiment

The experiment was carried out at the Grand Accélérateur National d'Ions Lourds (GANIL). A beam of ^{33}Al was obtained from the fragmentation of ^{36}S projectiles at $E = 77.5\,A$MeV on a $0.22\,\mathrm{g/cm^2}$ thick ^{9}Be target. In order to produce spin-polarized ^{33}Al, fragments emitted at finite angles, $\theta_{\mathrm{Lab}} = 1$ to $3\,^\circ$, from the primary beam direction were introduced to the fragment separator LISE. The primary beam was deflected by 2° with respect to the target located at the spectrometer entrance. A range of momenta p/p_{b} =1.026–1.041 was selected with slits placed at the momentum-dispersive intermediate focal plane. Here, $p_{\mathrm{b}} = 11.7\,\mathrm{GeV/c}$ is the fragment momentum corresponding to the projectile velocity. With a 2-μA intensity of the primary $^{36}S^{16+}$ beam, LISE provided the beam of ^{33}Al with a purity of 75 % and intensity of 1300 particles/s. The spin-polarized ^{33}Al fragments were transported to a β-NMR apparatus [44] located at the final focus of LISE, and were implanted in a stopper of hexagonal $\alpha-Al_2O_3$ single crystal (corundum). A static magnetic field $B_0 = 497.62\,\mathrm{mT}$ was applied to the stopper in order to preserve the ^{33}Al spin polarization. The layout of the β-NMR apparatus is shown in Fig. 2.1. The $\alpha-Al_2O_3$ crystal was cut into a $25.5 \times 28 \times 1\,\mathrm{mm^3}$ slab, and was mounted in a stopper chamber so that the c-axis was oriented parallel to the B_0 field. The stopper was kept in vacuum and cooled to a temperature $T \simeq 80\,\mathrm{K}$ to suppress the spin-lattice relaxation of ^{33}Al during the β-decay [41].

The Q moment interacts with an electric field gradient eq acting at the site of the implanted nucleus in a single crystal stopper. The eqQ interaction causes energy shifts in the individual Zeeman magnetic sublevels. Under the present situation of the experiment, where the angle between the c-axis and the B_0 field was set at $\theta = 0\,^\circ$, the resonance frequency $\nu_{m,m+1}$ between magnetic sublevels m and $m+1$ ($m = -I, -I+1, \ldots, I-1$) of the nuclear spin $I = 5/2$ is given by

$$\begin{aligned}\nu_{m,m+1} &= \nu_{\mathrm{L}} - \nu_{\mathrm{Q}} \left(3\cos^2\theta - 1\right) \frac{3(2m+1)}{8I(2I-1)} \\ &= \nu_{\mathrm{L}} - \frac{3}{40}(2m+1)\nu_{\mathrm{Q}}, \end{aligned} \tag{2.1}$$

where ν_{L} denotes the Larmor frequency, $\nu_{\mathrm{Q}} = eqQ/h$ the quadrupole coupling constant, and eq the electric field gradient along the c-axis. Q and h denote the Q moment and the Planck's constant, respectively. If the true value for ν_{Q} is inserted in

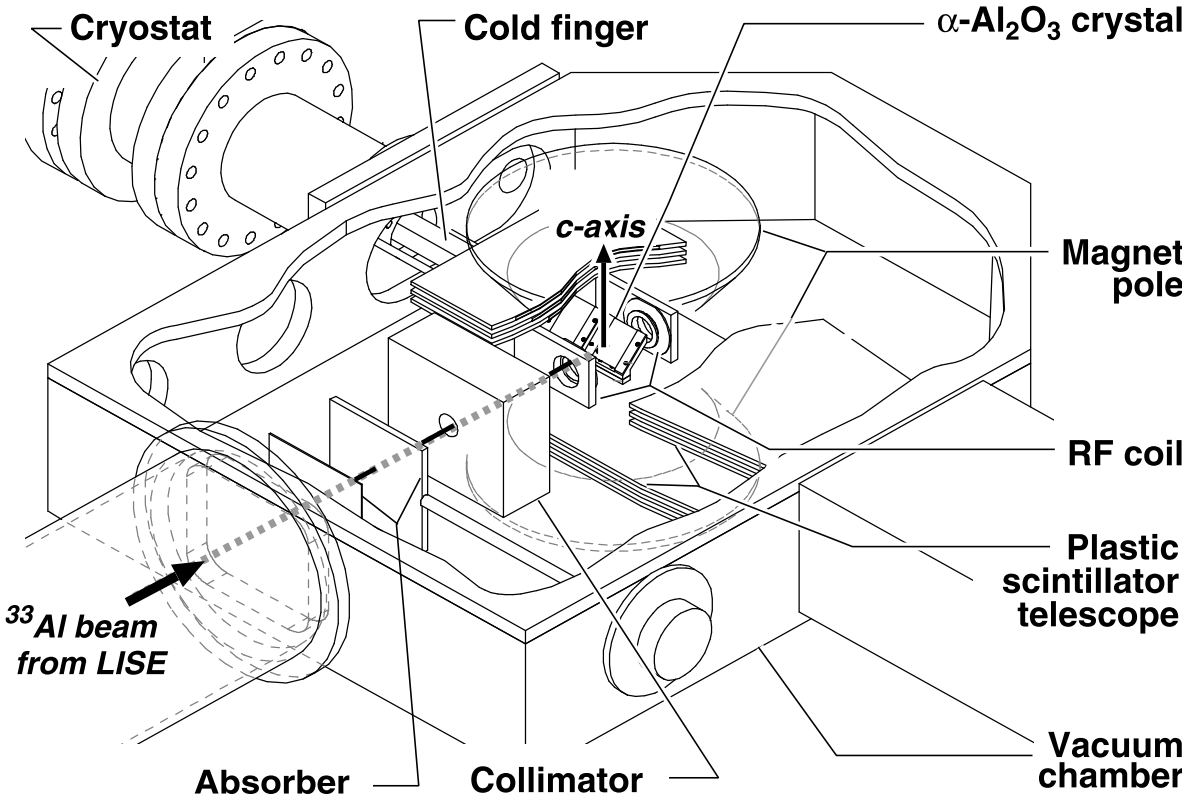

Fig. 2.1 Schematic layout of the β-NMR apparatus. Details are given in Ref. 44.

Eq. (2.1), the application of an oscillating magnetic field B_1 whose frequency is swept across $\nu_{m,m+1}$ (ν_Q) should lead to a reversal of the population between sublevels m and $m+1$ (the adiabatic fast passage technique (AFP) [45]). Application of a B_1 field having all these five (=2I) different $\nu_{m,m+1}$ frequency components ensures that through scanning the single parameter ν_Q, the fulfillment of $\nu_Q = eqQ(^{33}\mathrm{Al})/h$ could be detected through the simultaneous occurrence of all the $2I = 5$ resonances, which consequently leads to collective alteration of the spin polarization [41]. Note that the full reversal of spin requires a sequence of stepwise reversals between two contiguous sublevels. The B_1 field was applied in $I(2I+1) = 15$ steps in the same sequence as described in Ref. 46. In each step the frequency ν was swept from $\nu_{m,m+1}$ $\left(\nu_Q{}^{\mathrm{lower}}\right)$ to $\nu_{m,m+1}$ ($\nu_Q{}^{\mathrm{upper}}$) with $\nu_Q{}^{\mathrm{lower}}$ and $\nu_Q{}^{\mathrm{upper}}$ denoting the lower and upper bounds of the searched ν_Q region.

Thus, the ν_Q resonance was detected as a change in the β-ray asymmetry (we hereafter denote this technique of β-ray detected NMR spectroscopy in a non-cubic crystal by the β-NQR method). The β-rays emitted from the implanted ^{33}Al nuclei were detected with scintillator telescopes located above and below the stopper. They were

housed inside the vacuum chamber, each consisting of three 1-mm-thick plastic scintillators. The up/down ratio R of the β-ray counts is written as

$$R = a\frac{1 + v/c \cdot A_\beta P}{1 - v/c \cdot A_\beta P} \simeq a(1 + 2A_\beta P), \tag{2.2}$$

where a is a constant factor representing asymmetries in the counter solid angles ($\Omega_\beta \sim 4\pi \times 0.22\,\mathrm{sr}$ each) and efficiencies, v/c the velocity of the β particle, A_β the asymmetry parameter, and P the ^{33}Al nuclear spin polarization. The primary branch of the ^{33}Al β-decay is to the ground state of ^{33}Si with a branching ratio of ∼ 89 % [10] and decay Q value $Q_\beta = 11.990\,\mathrm{MeV}$ [47]. Since a β particle looses part of its energy in penetrating the materials around the stopper before entering the β-raytelescope, only those β particles with $E_\beta \geq 1600\,\mathrm{keV}$ [48] (or $v/c \geq 0.97$) were counted. Thus, the ratio R in Eq. (2.2) is well approximated by the second expression setting $v/c \approx 1$. By taking a double ratio R/R_0, where R_0 is the value for R measured without the B_1 field, the change in the R/R_0 ratio of the β-ray yields upon the NQR is given as

$$\frac{R}{R_0} \simeq \frac{a(1 - 2A_\beta P)}{a(1 + 2A_\beta P)} \simeq 1 - 4A_\beta P, \tag{2.3}$$

if the fragment spin polarization is fully reversed from P to $-P$. Since the constant a is canceled out in Eq. (2.3), the alternation of the spin polarization can be detected as the deviation of R/R_0 from the unity. The resonance frequency is derived from the position of a peak or dip in the R/R_0 spectrum. The experiment was done with a pulsed beam with typical beam-on and beam-off periods of 20 and 109 ms, respectively. In the beam-off period, the sequence of the B_1-field for the nuclear magnetic resonance was applied in the first 9 ms duration, and then the β-rays were counted in the remaining 100 ms duration.

2.3 Data analysis

Fig. 2.2(a) shows a β-NMR spectrum obtained for ^{33}Al in a cubic Si crystal in runs prior to the NQR measurements, using the same apparatus and B_0 setting for the ν_L determination. The spectrum was analyzed based on a least-χ^2 fitting procedure with a Gaussian function

$$G_\sigma(\nu) = a \exp\left(-\frac{\left(\nu - \nu^{(0)}\right)^2}{2\sigma^2}\right) + 1. \tag{2.4}$$

Here a and $\nu^{(0)}$ are the parameters that were varied during the fitting procedure, while σ was kept constant at values obtained from a numerical simulation, in which a time-dependent Schrödinger equation of the spin motion in the AFP spin reversal process was solved under the actual B_0 and B_1 magnetic field settings. The resulting fitting curve is also shown in Fig. 2.2(a). From the peak frequency ν_L = 6217(3) kHz, a result μ = 4.097(2) μ_N was deduced. The error quoted here included an error in the B_0 field calibration, performed for the present β-NMR setup with a proton NMR probe, of $\Delta B_0 \ll 0.01$ mT, which was in fact negligibly small. The presently obtained μ value agrees with the reported value μ = 4.088(5) μ_N [9] within the experimental error. From the resonance amplitude the spin polarization of ^{33}Al was determined to be $P \sim -2.0(5)$ %, assuming $A_\beta \sim 0.89$, as deduced from the experimentally known β-decay branching ratios [10].

In Figs. 2.2(b) and (c) the measured R/R_0 ratios for the ^{33}Al in $\alpha-Al_2O_3$ single crystal are shown as a function of the quadrupole frequency ν_Q (the β-NQR spectrum). In principle, the resonance width of AFP-NMR spectra becomes approximately a bin width of the swept frequency. The observed widths of the obtained NQR spectra are, however, much broader than $\Delta\nu_Q$ = 485(176) kHz of a wide (narrow) ν_Q-window scan. By fitting the spectrum of the wide ν_Q-window scan shown in Fig. 2.2(b) to a Gaussian function $G_\sigma(\nu_Q)$ of Eq. (2.4), a substantially broader width 1.3(2) MHz (FWHM), calculated from the resulting σ = 564(97) kHz, was obtained, where σ, as well as a and $\nu_Q{}^{(0)}$, were treated as free parameters to be determined through the fitting. The obtained parameter $\nu_Q{}^{(0)}$ = 2116(73) kHz represents the position of the peak, from which the quadrupole coupling constant eqQ/h will be deduced. According to a numerical simulation, σ_{AFP} = 209 kHz is expected as a width caused by the AFP spin reversal process, in which further line-shape broadening effects, e.g.,

due to the fluctuation of an electric field gradient q are not included. As a result, an extra broadening $\sigma_{\mathrm{extra}} = 524\,\mathrm{kHz}$ is needed in order to reproduce the observed $\sigma = 564\,\mathrm{kHz}$. The origin of σ_{extra} has not yet been well understood. Although an externally implanted Al ion would most likely stop at the site of the same element in the host crystal, there may be a possibility that some fraction of the implanted ions stop at other, metastable, sites. Also, some of the implanted ions might stop at a site of ^{27}Al atom that is accompanied by a near-by lattice defect produced by implantation, thus leading to a shifted NQR resonance. In these cases the NQR spectrum would show a broadened peak. In the present analysis such effects are expressed as a non-zero value of σ_{extra}. We therefore took into account the extra width determined in the fitting, $\sigma_{\mathrm{extra}} = 524\,\mathrm{kHz}$, as an independent systematic error. Thus, an experimental error $\delta\nu_Q{}^{(0)} = \pm 77\,(\mathrm{stat}) \pm 524\,(\mathrm{sys})\,\mathrm{kHz}$ was assigned to the peak frequency $\nu_Q{}^{(0)} = 2116\,\mathrm{kHz}$, where an uncertainty from the eq value, $\delta\nu_Q{}^{(0)} = 14\,\mathrm{kHz}$, and that from a θ setting error, 1.1 kHz, were also included. The same fitting procedure was then applied to a narrow ν_Q-window scan spectrum shown in Fig. 2.2(c), with a resulting peak frequency $\nu_Q{}^{(0)} = 2159(46)\,\mathrm{kHz}$. For the obtained peak an extra broadening effect was observed again with $\sigma = 263\,\mathrm{kHz}$ at this time, and was regarded to represent a systematic error in the obtained $\nu_Q{}^{(0)}$. Thus, the peak frequency was determined to be $\nu_Q{}^{(0)} = 2159 \pm 46\,(\mathrm{stat}) \pm 263\,(\mathrm{sys})\,\mathrm{kHz}$. The $\nu_Q{}^{(0)}$'s determined from the wide and narrow ν_Q scans agree very well. We have obtained a quadrupole coupling constant $|\nu_Q{}^{(0)}| = |eqQ/h| = 2.16(27)\,\mathrm{MHz}$ from the narrow ν_Q scan, in which the observed extrabroadening effect is smaller. The Q moment of ^{33}Al is deduced from the relation $|Q(^{33}\mathrm{Al})| = |Q(^{27}\mathrm{Al}) \cdot \nu_Q(^{27}\mathrm{Al})/\nu_Q(^{27}\mathrm{Al})|$, where $Q(^{27}\mathrm{Al})$ and $\nu_Q(^{27}\mathrm{Al})$ denote the Q moment of ^{27}Al and the quadrupole coupling constant of ^{27}Al in $\alpha{-}\mathrm{Al_2O_3}$, respectively. By inserting the reported values $Q(^{27}\mathrm{Al}) = 146.6(10)\,e\mathrm{mb}$ [49] and $\nu_Q(^{27}\mathrm{Al}) = 2389(2)\,\mathrm{kHz}$ [50], the ground-state Q moment for ^{33}Al has been determined as $|Q_{\mathrm{exp}}(^{33}\mathrm{Al})| = 132(16)\,e\mathrm{mb}$.

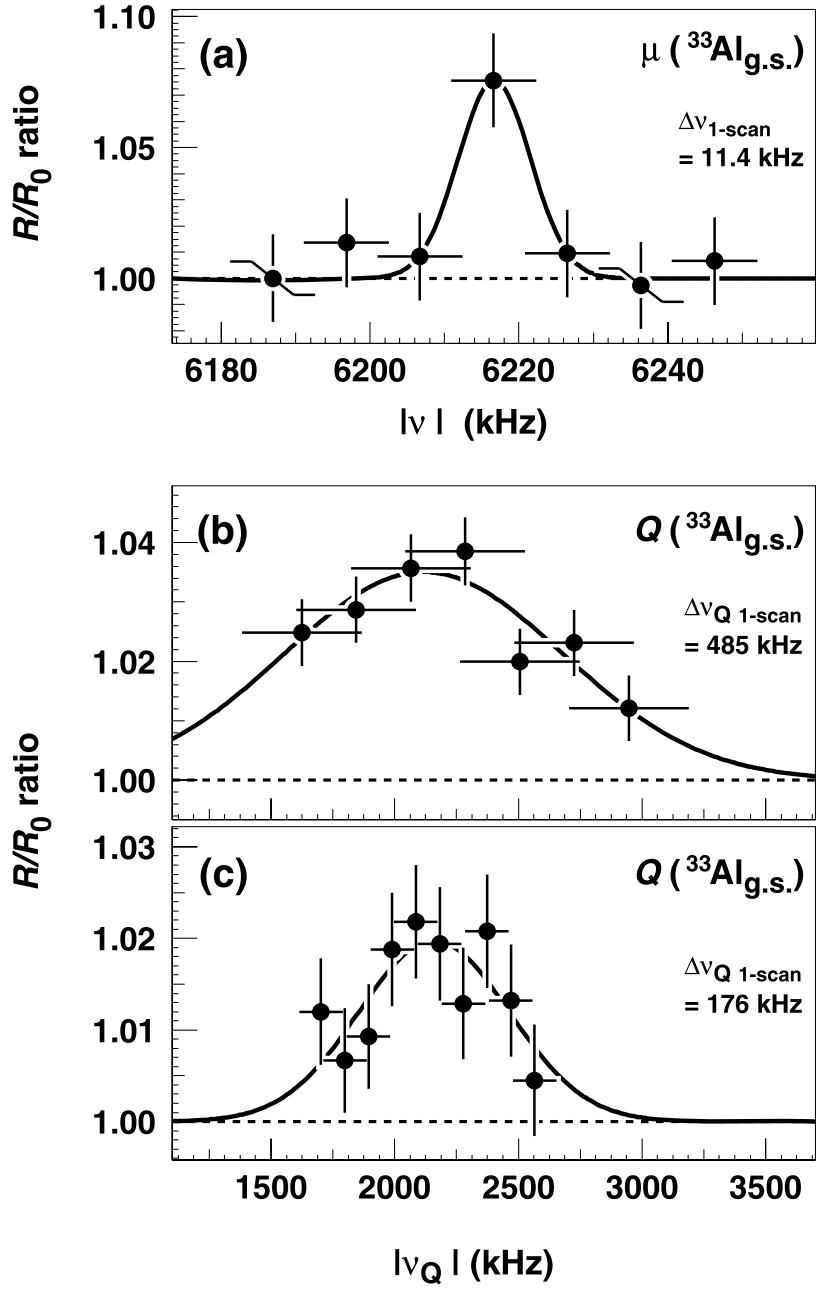

Fig. 2.2 (a) The NMR spectrum obtained for the ground state of ^{33}Al in a Si crystal. (b), (c) The NQR spectra obtained in an $\alpha-Al_2O_3$ crystal with wide and narrow ν_Q-window scans. The ordinate of each spectrum shows a double ratio R/R_0, where R denotes the up/down ratio of the β-ray counts measured with application of the B_1 field for the quadrupole coupling frequency ν_Q, and R_0 the up/down ratio without the B_1 field. The vertical bar attached to the data point represents the statistical error due to β-counting statistics, while the horizontal bar indicates the width of the $\nu(\nu_Q)$ frequency sweeps. The results of the least-χ^2 fitting analysis are shown by solid curves.

2.4 Discussion

Before turning to a closer examination of $|Q_{\rm exp}(^{33}{\rm Al})|$, a few remarks should be made concerning its μ moment. In the study of the μ-moment measurement of ^{33}Al [9], $\mu_{\rm exp}(^{33}{\rm Al})$, it was reported that $|\mu_{\rm exp}(^{33}{\rm Al})|$ differs from the theoretical μ of the shell-model calculation with the USD interaction [51] by 3.9 %, and that this difference can be explained by the admixture of *pf*-intruder configurations of at least 25 %. This statement is also supported by a large scale shell model calculation in the Monte Carlo Shell Model (MCSM), with the SDPF-M interaction [52]. This calculation reproduces $|\mu_{\rm exp}(^{33}{\rm Al})|$ within a 0.4 % difference, in which the admixture of 63 % intruder configurations is predicted. The above observation also indicates that $\mu_{\rm exp}(^{33}{\rm Al})$ is rather insensitive to the *pf* admixture. This insensitivity seems reasonable if configurations, in which two neutrons are excited to the *pf* orbit, are considered. The contribution from these configurations to the μ moment is a second-order correction, while the contribution to the Q moment is a first-order effect. Reflecting this, the theoretical value of $Q(^{33}{\rm Al})$ in the SDPF-M model largely differs from that in the USD model, by $\Delta Q(^{33}{\rm Al}) = 41\,\%$, in contrast to the small difference $\Delta\mu(^{33}{\rm Al}) = 4.3\,\%$[*1] in the theoretical values of $\mu(^{33}{\rm Al})$ between the two models. A similar example is the case of ^{29}Na, in which both the USD and SDPF-M calculations well reproduce the experimental μ moment, while their theoretical Q moments differ by 30 % from each other. The experimental Q agrees well with the SDPF-M prediction [54].

The obtained $|Q_{\rm exp}(^{33}{\rm Al})|$, together with those reported for other odd-aluminum isotopes [41, 43, 49], is plotted as a function of mass number in Fig. 2.3(a). The values of the ^{27,31}Al and ^{33}Al $I = 5/2$ ground states are all very similar, around 130 to 140 $e$mb. However, if $N = 20$ is a well-developed shell gap, then one would expect a much smaller quadrupole moment for ^{33}Al, as its quadrupole moment would be only determined by the odd-proton configuration (thus including only proton-proton correlations). No mixing of neutron configurations in the ground state wave function can occur if the $N = 20$ shell is completely filled and excitations across $N = 20$ are excluded. When opening the $N = 20$ shell, as in ^{27}Al and ^{31}Al, an increase in the quadrupole moment occurs due to proton-neutron and neutron-neutron correla-

[*1] The quoted value of difference $\Delta\mu(^{33}{\rm Al}) = 4.3\,\%$ is for a case when the free-nucleon M1 operators are adopted, as in Ref. 9. If instead the effective operators of Ref. 53 are adopted, $\Delta\mu(^{33}{\rm Al})$ becomes 6.7 % which is still small compared to $\Delta Q(^{33}{\rm Al})$.

tions in the *sd* shell. This is nicely shown by the USD shell model calculations [51], which are performed in the *sd* shell model space for both protons and neutrons. As in our earlier studies [41, 43, 55] isospin-dependent effective charges were used for protons and neutrons [56].*[2] Independent on the used effective interaction (USD, USDA or USDB [57]), a similar trend is predicted for the odd-Al quadrupole moments, in agreement with the observed values for ^{27}Al and ^{31}Al. However, the predicted value for ^{33}Al (95 $e$mb) is much smaller than the observed one (132(16) $e$mb), suggesting that neutron-neutron and/or neutron-proton correlations are required to reproduce the increased ^{33}Al quadrupole moment. Thus opening up the *sd* shell is needed, and excitations of neutrons into the fp shell, across the $N = 20$ gap, need to be taken into account.

In Fig. 2.3(a) theoretical Q moments predicted by the MCSM, with the SDPF-M interaction [52] and the constant effective charges adopted in the study of Na isotopes [54], are shown by a dotted line (i). Also, the probability for the *pf* intruder configuration predicted by the MCSM is shown in Fig. 2.3(b). In fact, the predicted *pf* intruder probability increases from 5–10 % for the cases of $^{29-32}$Al to 63 % for the ^{33}Al case, suggesting a weakening of the $N = 20$ shell closure. Accordingly, the theoretical Q moment for ^{33}Al is large, $Q_{\mathrm{MCSM}}(^{33}\mathrm{Al}) = 166\,e$mb. The observed Q, $\left|Q_{\mathrm{exp}}(^{33}\mathrm{Al})\right| = 132(16)\,e$mb, falls in between the USD and MCSM values. We note, however, that MCSM well reproduces $|Q_{\mathrm{exp}}(^{33}\mathrm{Al})|$ if we adopt the above noted isospin-dependent effective charges, as shown by a dotted line (ii). The situation is definitely different from the neighboring nucleus ^{31}Al, for which the μ [38] and Q [41, 43] moments as well as the level structure [38] are well reproduced by the *sd* shell model.

The above observation indicates that the ^{33}Al ground state is mixed with *pf*-intruder configurations whereas the ^{31}Al ground state is not. In a next step, we can investigate whether the admixture of *pf*-intruder configurations is caused by a static nuclear deformation. Assuming an axially symmetric static deformation with the nuclear spin along the symmetry axis, the spectroscopic quadrupole moment Q is related to its intrinsic quadrupole moment Q_0 through a relation:

$$Q = \frac{3K^2 - I(I+1)}{(I+1)(2I+3)} Q_0 \tag{2.5}$$

*[2] Specifically, we took effective charges of proton (neutron) e_{p} (e_{n}) = 1.10 (0.56), 1.09 (0.53), 1.07 (0.44), and 1.05 (0.38) for ^{27,29,31,33}Al isotopes, respectively.

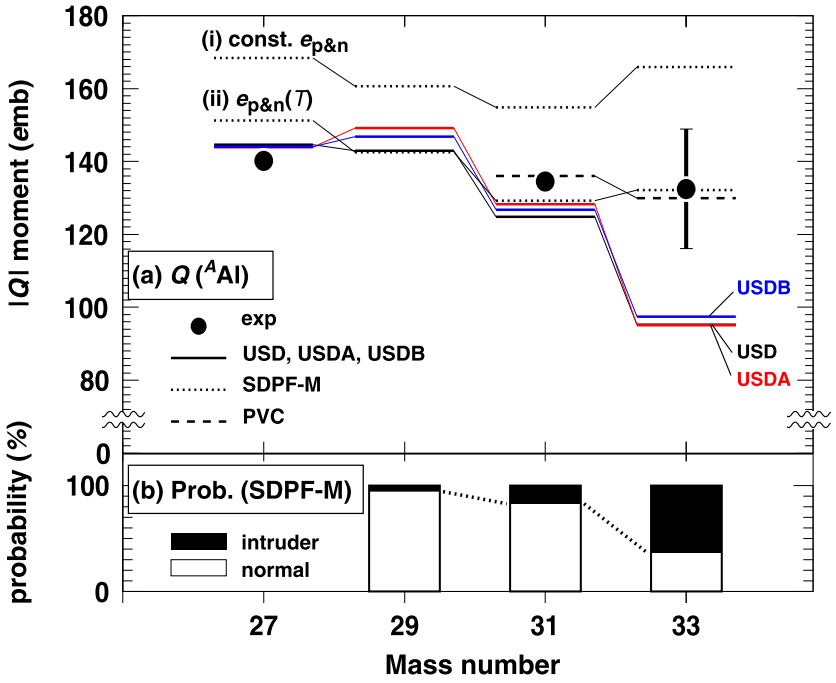

Fig. 2.3 (a) Experimental (solid circles) and theoretical (lines) Q moments of odd-mass neutron-rich aluminum isotopes as a function of mass number. The data for $A = 31$ is plotted by taking a weighted average of the results from Refs. 41 and 43. Theoretical values are obtained from shell model calculations with USD interactions using isospin-dependent effective charges (solid line). Theoretical values of Monte Carlo Shell Model (SDPF-M), for which (i) constant effective charges and (ii) isospin-dependent effective charges are adopted, and a particle-vibration coupling model (PVC) are also shown by dotted and dashed lines, respectively. (b) The probabilities for normal and intruder configurations predicted by SDPF-M are shown.

with K the projection of the nuclear spin I on the deformation symmetry axis (thus $K = I$). The intrinsic quadrupole moment of an ellipsoidal charge distribution can then be related to the quadrupole deformation parameter β as follows:

$$Q_0 = \frac{3}{\sqrt{5\pi}} ZR^2\beta \left(1 + 0.36\beta + \cdots\right)$$
$$\left(R = 1.2A^{1/3}\right) \tag{2.6}$$

Using these expressions, we find similar deformation parameters for ^{31}Al and ^{33}Al, respectively $\beta = 0.25$ and 0.24. This similarity between these β values suggests that the admixture of pf-intruder References configurations in ^{33}Al does not receive significant influence of the nuclear deformation, since such an admixture is considered to be small in ^{31}Al.

Fig. 2.3(a) includes the prediction from the mean field approach [58] as indicated by a dashed line: The structure of ^{33}Al was treated in a microscopic particle-vibration coupling (PVC) model in which the coordinate-space Skyrme-Hartree-Fock-Bogoliubov and quasiparticle-random-phase approximations were employed. In this model, the ^{33}Al ground state was described as a proton single-hole state $(\pi d_{5/2})^{-1}$ coupled to a ^{34}Si core to form $I^\pi = 5/2^+$.

The PVC Hamiltonian is diagonalized in a model space consisting of the $(\pi d_{5/2})^{-1}$ hole state coupled to the quadrupole vibrational states in ^{34}Si. The resulting ^{33}Al ground-state wavefunction involves a substantial neutron mean occupation number in the *pf* orbit of ≈ 0.8. This feature is inherited from the $I^\pi = 0^+$ core state of ^{34}Si. It is interesting to note that a spherical shape is predicted for the ^{34}Si core state in spite of the substantial amplitude of intruder configurations, where the neutron pairing, instead of the static deformation, associated with the weakening of the $N = 20$ magic number plays an important role. Also, a predicted theoretical Q moment $Q_{\mathrm{PVC}}(^{33}\mathrm{Al}) = 130\,e\mathrm{mb}$ [58] with this wavefunction reproduces excellently the presently obtained $|Q_{\mathrm{exp}}(^{33}\mathrm{Al})|$.

2.5 Summary

In summary, the ground-state Q moment of ^{33}Al has been determined by the β-NQR method using the fragmentation-induced spin polarization. The obtained Q moment, $\left|Q_{\mathrm{exp}}(^{33}\mathrm{Al})\right| = 132(16)\ e\mathrm{mb}$, shows a significant excess from the prediction of the USD shell model calculation. The large Q is a clear signature that the $N = 20$ shell closure erodes in ^{33}Al. The structure of the ^{33}Al ground state was then investigated through the obtained $|Q_{\mathrm{exp}}(^{33}\mathrm{Al})|$ by comparing with theoretical values predicted from the large scale shell model MCSM and a particle-vibration coupling model treating the neutron pairing correlations in the ground state of ^{33}Al instead of the static nuclear deformation. A significant admixture of *pf* intruder configurations to the ^{33}Al ground state was needed in both theoretical approaches to explain the observed large Q.

Part II

Development for Slow or Stopped Radioactive Isotopes

Chapter 3

Development of Radio-Frequency Ion-Guide Isotope Separator On-Line (RF-IGISOL)

3.1 Introduction

■Ion guide isotope separator on-line The Isotope Separator On-Line (ISOL) is playing an important role in studying unstable nuclei far from the β-stability line, where the ability of the target-ion-source combination has a great influence on the success of an ISOL experiment. Up to date, all possible efforts have been exerted to obtain better target-ion sources having higher efficiency and faster release time for as many elements as possible, and as a result the number of known nuclei is gradually increasing. However, it seems that the front-line for discovering unknown nuclei is in some kind of a deadlock, particularly with regard to proton-rich nuclei. This situation is caused by the properties of the remaining unknown nuclei, *i.e.*, they have shorter half-lives (≤ 0.5 s) and higher melting temperatures (≥ 1000 K). Under these circumstances, the ion-guide method has appeared as one of the candidates for making a breakthrough.

The ion-guide method (Ion Guide Isotope Separator On-Line, abbreviated as IGISOL) was first developed by the group of the University of Jyväskylä on the basis of the He-jet technique [20, 21, 59]. The principle of IGISOL is following: radioactive recoil ions, being in a multiple-charge state, recoil out of the thin target after the nuclear reaction, and are thermalized in helium buffer gas after many collisions. The important point is in the fact that some fraction of these thermalized atoms are still in 1+ charge state, since the ionization potential of He atom has a larger value than the heavier atoms. That is an astonishing fact from point of view of the atomic and molecular physics on a gas phase. Therefore, the IGISOL-system does not need to re-ionize the thermalized atom of unstable nucleus. The ions are transported by a helium flow out of the target chamber and are guided into the mass separator by an electric field. The distinct features of the ion-guide method are simple construction, versatility, stability and room-temperature operation, which are due to the fact that there is no transfer tube, no evaporator and no ionizer.

■Brief history of studies of nuclear physics related to or using Tohoku IGISOL Since 1978, researches have been conducted on the nuclear structure and the fundamental physics using the ion beam accelerated by the 680 cyclotron of $K = 50$ MeV at CYclotron RadioIsotope Center (CYRIC) located in Tohoku University. The following is a brief history.

The first achievement is the measurement of the mirror transition of $^{57}_{29}Cu_{28}$ using a high-speed target-rotation device (TARO) [60–62].

More precise measurement required low background radiation environment using a mass-separated ^{57}Cu, so that development of an ion-guide type isotope separator on-line (IGISOL) had been started [63–67], and the present report stands in this line. The IGISOL has been developed in the second target room (TR2) in CYRIC, named "Tohoku IGISOL".

Ion beams produced at the IGISOL are low in energy and well-focused, and thus very suitable to be stored and trapped. A high-resolution laser microwave double-resonance spectroscopy of trapped Sr^+ ions was developed and was employed to measure a whole undeveloped hyperfine structure of the strontium isotopes [68, 69]. This was achieved for the stable Sr isotopes, so that measurement of the unstable Sr had been planned using the IGISOL.

During 1998–2001, the 680 cyclotron has been replaced to a 930 cyclotron of K = 110 MeV and, simultaneously, the new project for the improvement of Tohoku IGISOL has been started [22, 23]. In order to expand the elements of the obtained unstable nuclei to the neutron-rich A=100–130 region, the nuclear reaction was changed from the nucleon-transfer reaction to the proton-induced fission reaction of the thin uranium and thorium target. In order to increase the yields of the obtained unstable nuclei, this IGISOL has following unique properties: to enhance an acceptable range of recoiled fragments, the volume of the target cell was larger and the pressure of the helium gas filling the target cell was higher, and to collect recoiled fragments to an exit hole, a combination of DC and inhomogeneous radio-frequency (RF) electric fields applied in the target gas cell [22–25]. This radio-frequency ion-guide type ISOL was named "Tohoku RF-IGISOL".

■Studies using Tohoku RF-IGISOL and outline of this section A design and a performance of the present Tohoku RF-IGISOL are described in Sec. 3.2.

Using Tohoku RF-IGISOL, some experimental programs have been carried out, such as measurements of g-factor of the 225.98-keV excited state in ^{109}Rh [24], the half-life and the magnetic moment of the 49.72-keV excited state in ^{132}I [26], and half-life of the 163.82-keV excited state in ^{105}Ru explained in Sec. 3.3.

The result of the last experiment realized that the yield of the ^{105}Tc was not enough for measurement of the g-factor of the excited state in ^{105}Ru. In order to improve a mass resolving power and yields of unstable nuclei, a sextupole ion-guide (SPIG) [27]

has been installed into the skimmer region. The SPIG improves the vacuum around the acceleration stage of the separator and reduces the energy spread of the extracted ions. Section 3.4 explains a development of the SPIG.

3.2 Design and performance of Tohoku RF-IGISOL

The radio-frequency ion-guide type isotope separator on-line system is located in the second target room (TR2) of CYRIC at Tohoku University, and named "Tohoku RF-IGISOL". The most important features of Tohoku RF-IGISOL are a large gas cell including the reaction target and an RF carpet surrounding the exit hole. In order to enhance the stopping capability for fission products, the volume of the gas cell is enlarged to $10^4\,\mathrm{cm}^3$ which is 1000 times larger than the volume of the previous IGISOL [64]. Meanwhile ions of fission products stopped and thermalized widely in the gas cell. In order to maintain a high extraction efficiency for the ions the RF carpet is introduced, which applies DC and RF electric fields to the ions to guide to the exit hole without collisions with walls of the chamber.

3.2.1 Design of Tohoku RF-IGISOL

Target chamber

A target chamber consists of the gas cell and a skimmer region, and is connected to a mass separator. A photo of an outside of the target chamber is shown in Fig. 3.1. The gas cell consists of the target, a cylindrical electrode, the RF carpet, and a gas inlet. The skimmer region is the volume between the exit hole and a skimmer electrode, and is evacuated using a mechanical-booster pumping system composed of two pumps (40 000 l/m and 10 000 l/m at 50 Hz) and a rotary pump (1600 l/m) connected in series [64].

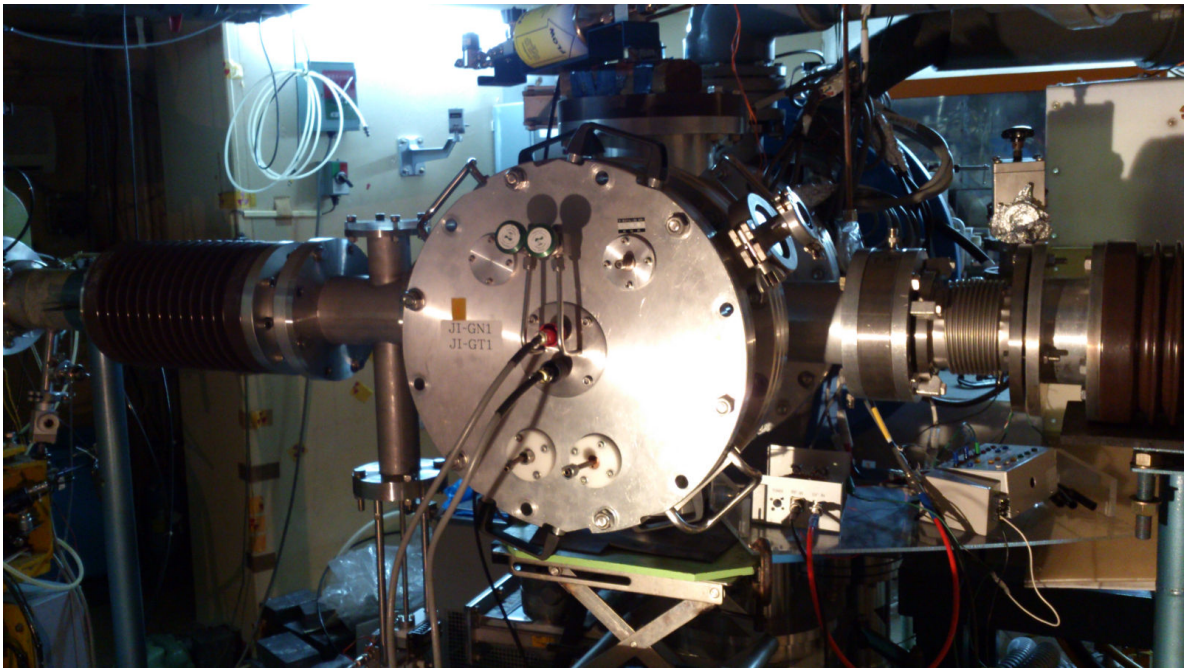

Fig. 3.1 Photo of outside of target chamber.

Target

The target of the proton-induced fission consists of natural uranium and thorium plates of 20 mg/cm^2 thick tilting at 6° angle to an axis of the primary beam and, thus, the effective thickness is 190 mg/cm^2. Number of both the uranium and the thorium plates is five, and the size of each is 10 mm in diameter. Some plates are wrapped by an aluminum foil of 6 µm. All the ten plates align in a row (the uranium plates are upstream and the thorium plates are downstream) in an aluminum holder as shown in Fig. 3.2, and the cross section of the target to the primary beam is about 10×10 mm^2. The holder is wrapped by a molybdenum mesh and the aluminum foil of 6 µm which obstruct that the secondary electrons originated from the primary beam diffuse and the target plate goes out when unfortunately releasing from the holder. Photos of the target assembly set to the gas cell are shown in Fig. 3.3.

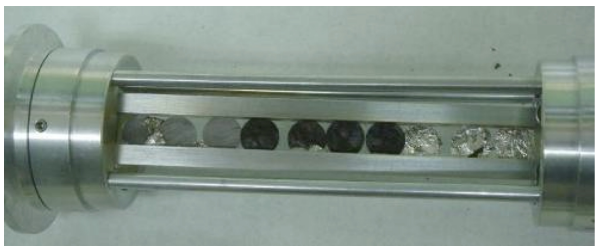

Fig. 3.2 Photo of thin target of uranium and thorium.

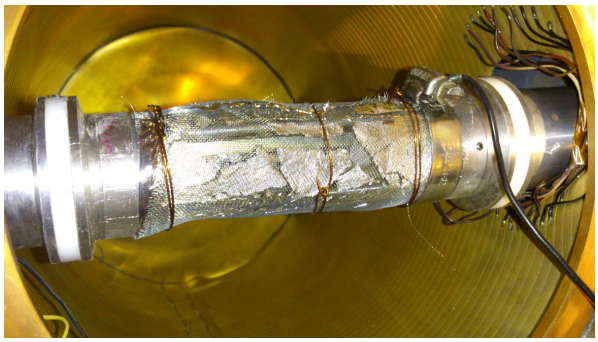

Fig. 3.3 Photo of target assembly set to gas cell. The cylindrical electrode and the RF carpet are also shown in the back.

Cylindrical electrode

A cylindrical electrode forms a side wall of the gas cell and consists of 60 electrode rings. Each of the electrode rings is 5.2 mm long, is aligned at interval of 0.2 mm and is connected by a chip resistor. The whole size is 220 mm in diameter and 320 mm long.

The cylindrical electrode is fixed on an inner wall of a copper cylinder. On an outer wall of the copper cylinder a cooling/heating pipe is brazed. One can flow a heating medium liquid controlled at −15 to 80 °C by a constant temperature liquid circulating device. The flow of the cooled liquid cools the copper cylinder and the cylindrical electrode, that suppresses the heat of the electrode and the circuit and gives rise to a purification of the helium gas filling the gas cell by an adsorption of gas impurities by the cooled copper plate. Meanwhile, the flow of the heated liquid bring about release of the absorbed gas molecules from the components of the gas cell. The heating medium liquid used is the Fluorinert FC77 of the 3M Company, which is non-conductive with a high dielectric strength (40 kV), and is a thermally and chemically stable fluid with a wide liquid range (−125 to 95 °C). The constant-temperature liquid

circulating device used is the TRL-N11L of the Thomas Kagaku Company.

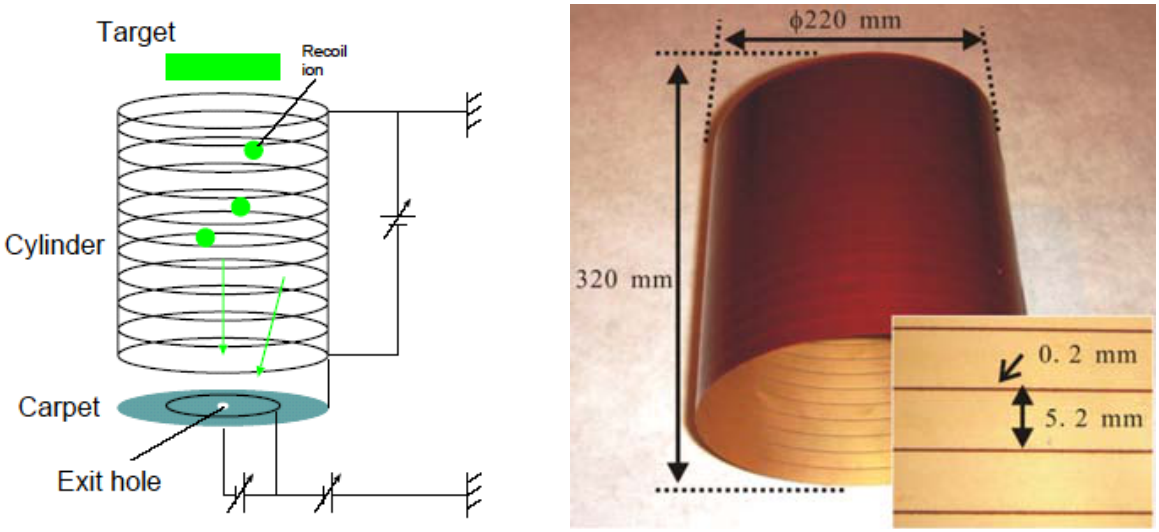

Fig. 3.4 cylindrical electrode of gas cell.

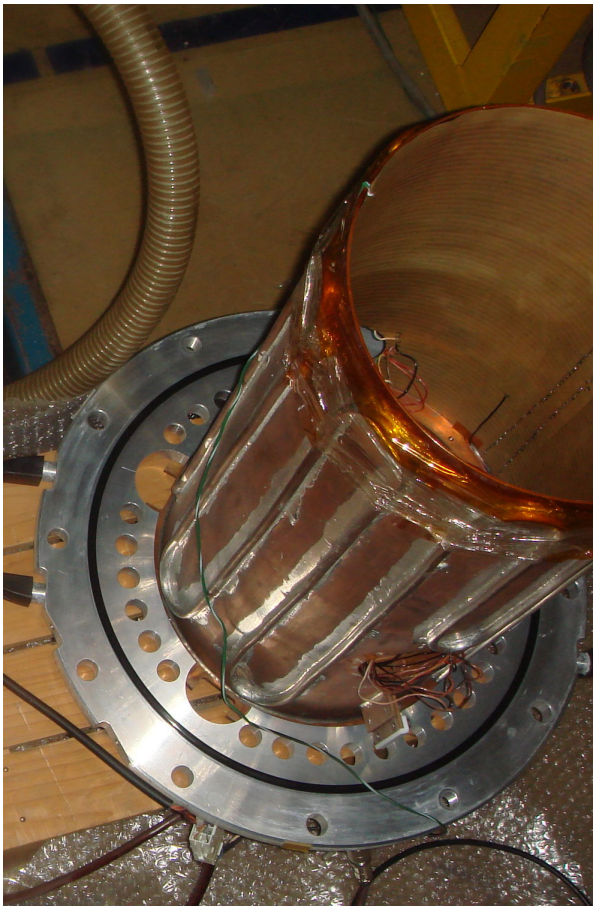

Fig. 3.5 Photo of cylinder-electrode assembly.

RF carpet and exit hole

The RF-carpet consists of a planar polyamide printed circuit board (PCB) 220 mm in diameter and 50 µm thick, 364 concentric ring electrodes, 0.15 mm each with a pitch of 0.3 mm, and an exit hole 1.2 mm in diameter bored at the center of the board as shown in Fig. 3.6.

A photo of the RF carpet installed into the gas cell is presented in Fig. 3.7.

A photo of the RF carpet assembly as seen from downstream is presented in Fig. 3.8. A back plate of the RF carpet is too weak to keep a high pressure, so that the RF carpet swells when the gas fills to the gas cell.

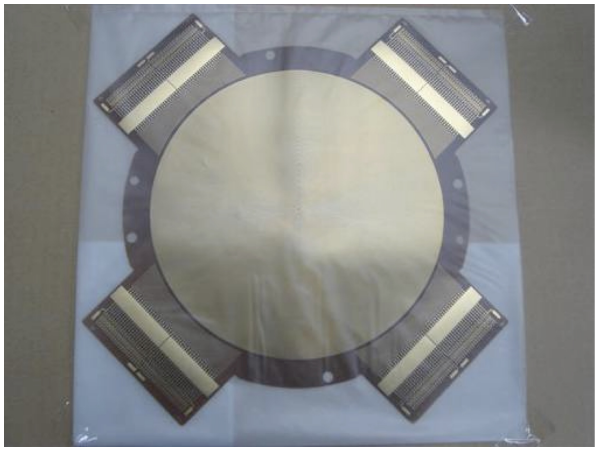

Fig. 3.6 Photo of RF carpet.

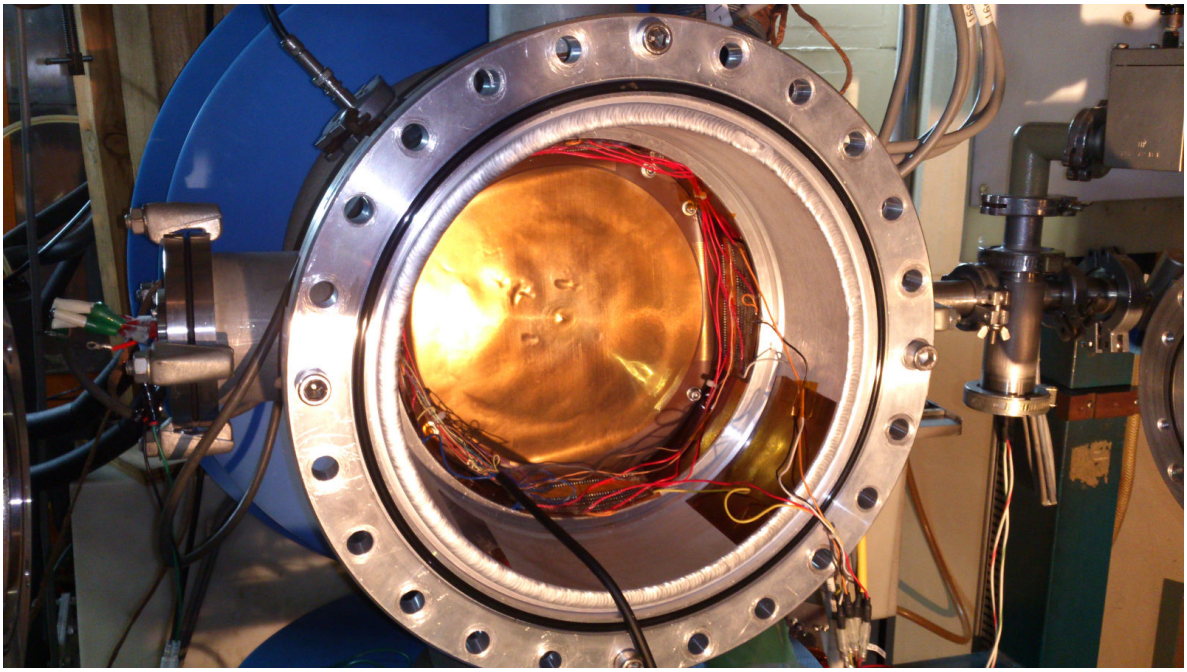

Fig. 3.7 Photo of RF carpet installed into gas cell.

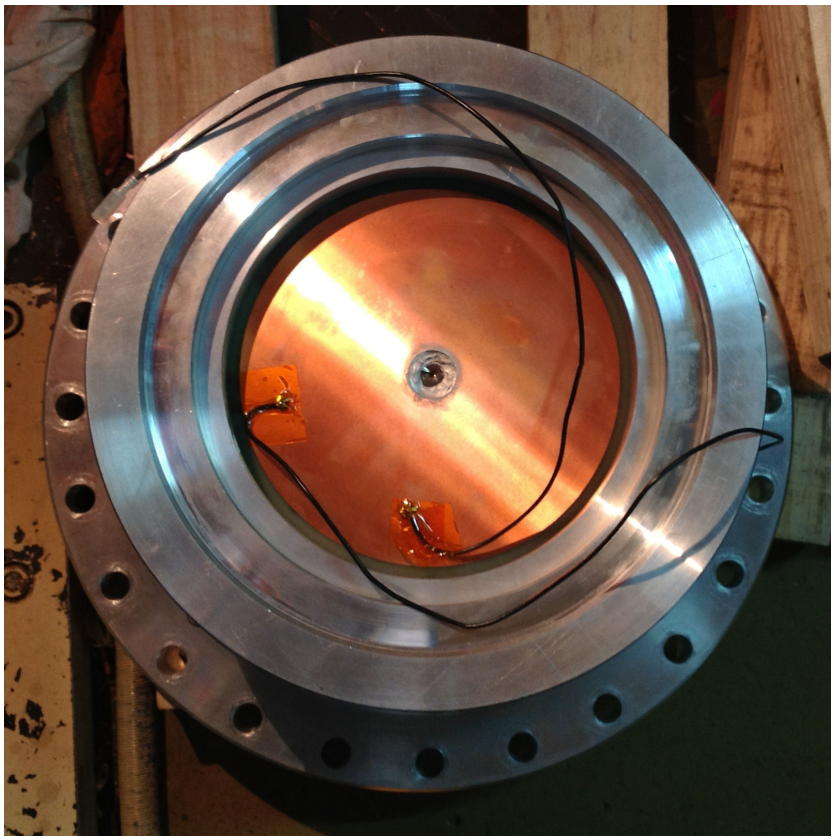

Fig. 3.8 Photo of RF carpet assembly as seen from downstream.

Skimmer electrode

A shape of the skimmer electrode is a cone of 10 mm long with an inlet hole of 1.2 mm in diameter. The skimmer electrode is fixed on a linear moving devices of which the range is from 0 to 10 mm. A photo of the skimmer assembly is presented in Fig. 3.9.

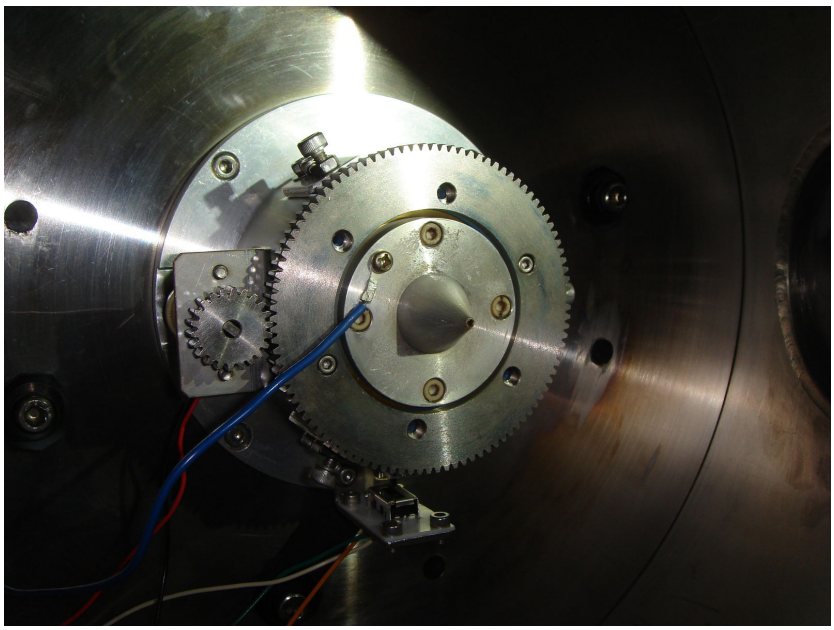

Fig. 3.9 Photo of skimmer assembly. A schematic view focused to the positions of the exit hole, skimmer electrode and extractor electrode is shown in Fig. 3.29.

Mass separator

The isotope separator is of the Scandinavian type, having a magnet with 55° deflection and 1.5 m radius-of-curvature. The original mass separator is DANFYSIK 9000-T shown in Fig. 3.10. The ion source located at the top right has been replaced with a target chamber involving the gas cell.

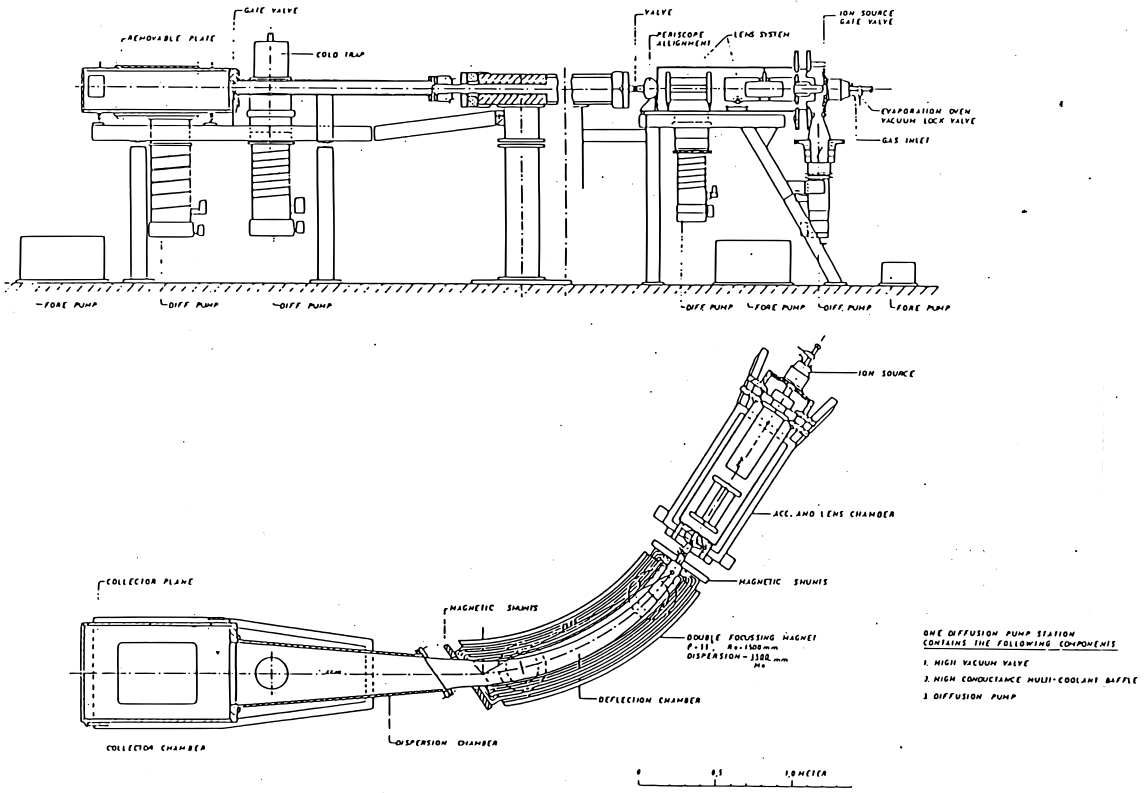

Fig. 3.10 Drawing of original mass separator, DANFYSIK 9000-T. Ion source located at the top right has been replaced with a target chamber involving the gas cell.

Typical parameters

Table. 3.1 shows typical parameters of Tohoku RF-IGISOL for $A = 105$, and Figure. 3.11 shows a DC potential of electrodes of Tohoku RF-IGISOL.

Table 3.1 Parameters of Tohoku RF-IGISOL for the $A = 105$ beam. A reference voltage in the gas cell and the extract region is the acceleration voltage, and one in the mass separator and beam transport region is the ground.

Primary beam	
Nuclei	proton
Energy	50 MeV
Current	1 μA
Gas cell and extract region	
Acceleration voltage	30.0 keV
Cylinder voltage	−30.0 V
Outer voltage	−40.0 V
Inner voltage	−30.0 V
RF Carpet-Radiofrequency	2.85 MHz
RF Carpet-RF Amplitude of the function generator	80 mV (160 mV_{pp})
Gas cell pressure	3.1 kPa (31 mbar)
Skimmer voltage	−600 V
Extractor voltage	−4.0 kV
Mass separator and beam transport region	
Lens 1 voltage	14.2 kV
Lens 2 voltage	13.0 kV
Y-def-up voltage	750 V
Y-def-down voltage	off
Dipole magnet current	69.34 A
Dipole magnetic field	169.85 mT (1.6985 kG)
Pressure at IG1	3.3×10^{-3} Pa (2.5×10^{-5} Torr)
Pressure at IG3	2.3×10^{-4} Pa (1.7×10^{-6} Torr)

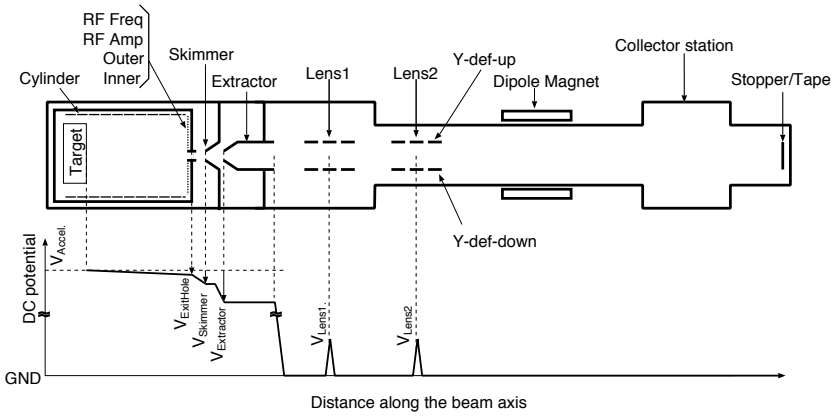

Fig. 3.11 DC potential of electrodes of Tohoku RF-IGISOL.

3.2.2 Performance of Tohoku RF-IGISOL

Yield

Yields of radioactive nuclei with Tohoku RF-IGISOL and the fission product cross section is shown in Fig. 3.12.

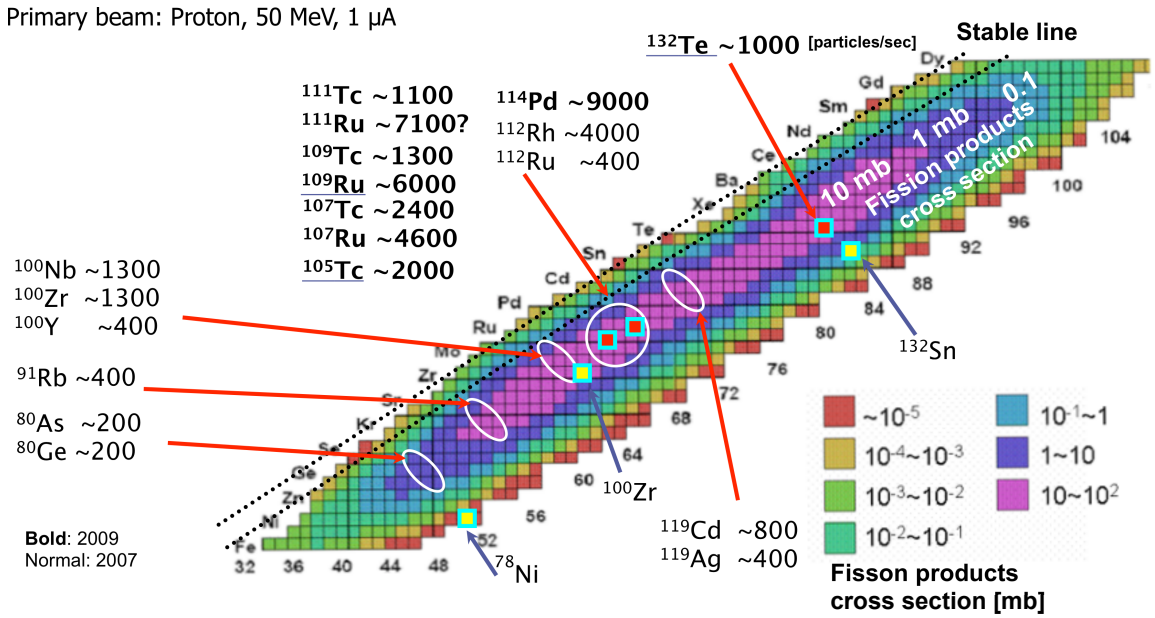

Fig. 3.12 Yields of radioactive nuclei with Tohoku RF-IGISOL and fission product cross section.

Mass resolving power

A mass spectrum in the $A \sim 110$ region with the skimmer-system RF-IGISOL is shown in Fig. 3.13. The average of the width of the distributions of $^{109-112}$Rh at fwhm is 1.7 mT, and thus the mass resolving power $M/\Delta M$ is 100.

The dispersion of $A \sim 110$ beams are 26 mm/mT at the end of the beam line using the acceleration voltage of 30 kV. The width of the transfer tape is 12 mm corresponding to 0.46 mT. Therefore, the average of the width of spatial distribution of an $A \sim 110$ beam is 1.7 mT at fwhm as shown in Fig. 3.13, so that at most 25 % of the extracted unstable nuclei were subjected to the measurement using the tape-transfer system.

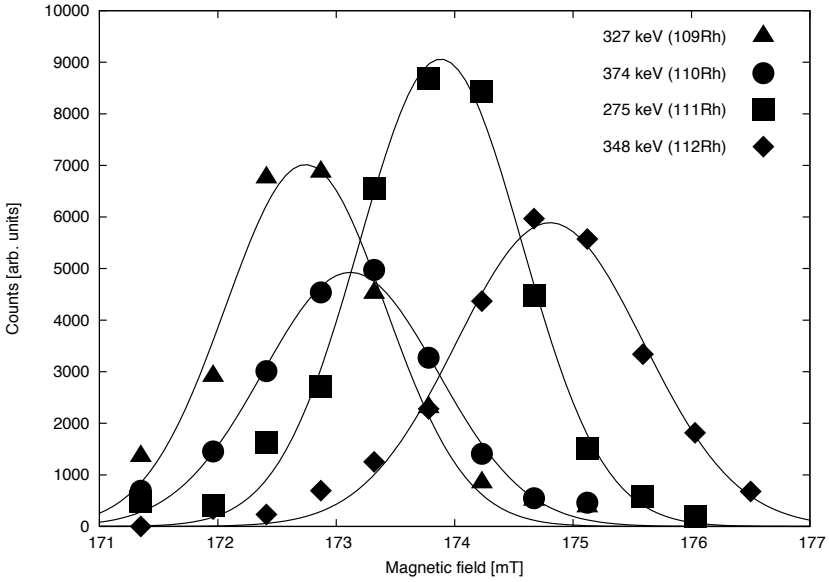

Fig. 3.13 Mass spectrum in $A \sim 110$ region with skimmer-system RF-IGISOL. The γ ray count with the HPGe placed at the end of the beam line with the Gaussian fits (solid lines) is plotted as a function of the magnetic field of the dipole of the mass separator. The average of the width of the distribution (fwhm) is 1.7 mT, and thus the mass resolving power $M/\Delta M$ is 100.

3.3 New result with Tohoku RF-IGISOL: half-life of isomeric state in ^{105}Ru

3.3.1 Introduction

It is interesting that Ru and Rh isotopes located in a region between Zr and Sn have been predicted to show shape-coexistence [7, 8]. ^{132}Sn is known as spherically shaped due to the double-closed shell while ^{100}Zr is strongly deformed, though difference in proton number between Sn and Zr is only ten. Thus, Ru and Rh would be right in the middle of transition in nuclear stricture, that would appear as a phenomenon of the shape-coexistence in low-lying states. It is originated from the following questions: which of a paring interaction or a quadrupole one becomes predominant and how many nucleons occupy individual orbits in the open shell. The paring interaction acts between two nucleons in the open orbits and tends to maintain the spherical-shape, while the quadrupole-quadrupole interaction acts between a particle and a hole and tends to make the shape deformed.

In the neutron-rich region the ratio between the number of protons and that of neutrons is very different, so that interactions between proton and neutron, usually ignored in the stable region, would become stronger. In a light-mass neutron-rich region it arises as a disappearance of the conventional magic number and an appearance of a new magic number [70, 71]. This fashion will become more apparent in a middle-mass neutron-rich region. Such studies require systematic and precise measurements of excitation energies, transition probabilities, half-lives, masses and nuclear moments.

Miyashita measured the g-factor of a 225.98-keV excited state in ^{109}Rh using Tohoku RF-IGISOL [24] and the method of perturbed angular correlation of γ-rays (γ-PAC), and obtained $g = 0.78^{+0.17}_{-0.03}\ \mu_{\mathrm{N}}$. This result indicates that a main configuration of the excited state is described by a single proton in a $g_{7/2}$ state coupled to a 2^+ rotational state of the deformed ^{108}Ru core. More detail discussion requires the systematic studies of magnetic moments around the ^{109}Rh such as one in Sec. 2.4. However, known magnetic moments in this region are rare except for those of alkali elements, alkaline-earth elements and stable nuclei, as shown in Figs. 1.1 and 3.24.

This section reports the measurement of the half-life of an 164-keV excited state in ^{105}Ru performed in the preparation work for the magnetic-moment measurement.

According to the low-lying excited states in ^{105}Ru shown in Fig. 3.14, the 164-keV excited state has suitable half-life, spin and cascade γ-rays for the nuclear-moment measurement using the γ-PAC.

3.3.2 Measurement of half-life of 164-keV excited state in ^{105}Ru

The setup and the diagram of electronics are shown in Figs. 3.15 and 3.16, respectively. Radioactive isotopes were produced by proton-induced fission and were separated using Tohoku RF-IGISOL, parameters of which are listed in Table 3.1. A coaxial high-purity germanium detector (HPGe) was placed at the end of the beam line for the particle identification of the mass-separated beam through measured γ-rays. The yield of ^{105}Tc ($T_{1/2}$=7.6 min) was evaluated from the yield of γ-rays of ^{105}Ru counted by the HPGe as shown in Fig. 3.17, A ^{105}Tc yield of 2×10^3 particle per second (pps) was obtained.

The measurement of half-life was performed by a conventional fast-slow coincidence method. A BaF_2 scintillation detector and a planar HPGe were placed face to face with a distance of 2 cm, and the tape moved through between the detectors. Sizes of the BaF_2 detector and the HPGe detector were 2 inch in diameter by 2 inch long and 21 cm^2 by 1 cm long, respectively. As shown in Fig. 3.16, an anode signal of a PhotoMultiplier Tube (PMT) of the BaF_2 detector and a timing signal of a preamplifier of the planar HPGe were sent to the logical AND operation through Constant Fraction Discriminators (CFD), Ortec 934. The fast event trigger consisted of a coincidence between those outputs from the CFD's. The outputs from the CFD's were also

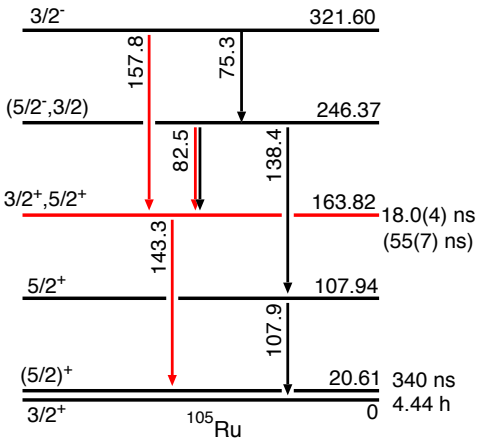

Fig. 3.14 Energy levels and life of isomers of ^{105}Ru.

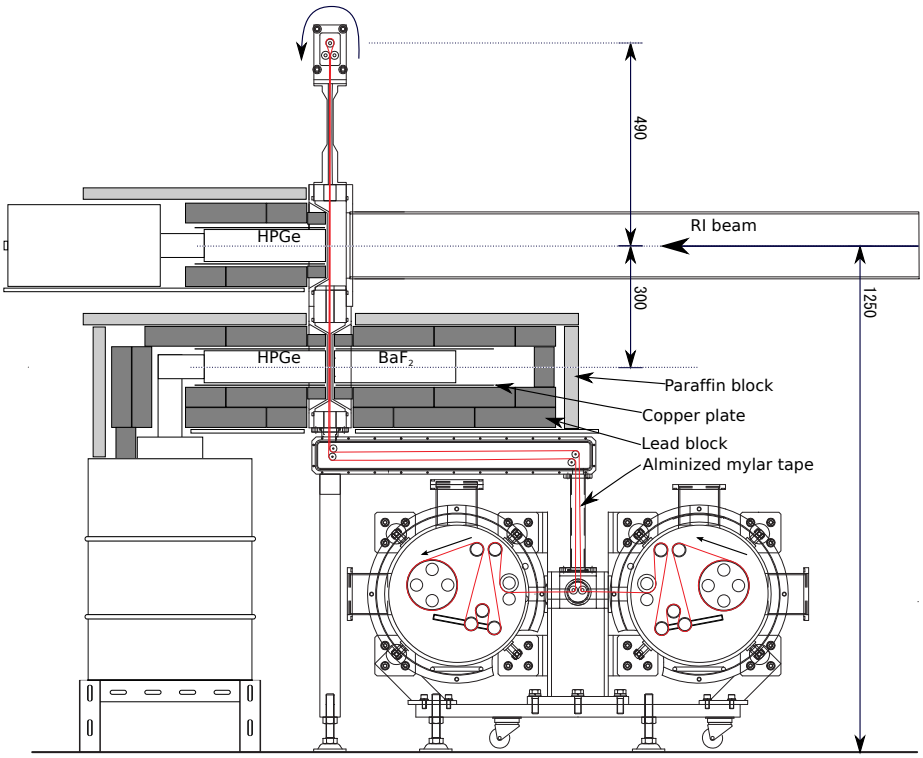

Fig. 3.15 Setup of ^{105}Ru half-life measurement.

sent to Time-to-Amplitude Converters (TAC), Ortec 566 and Ortec 567. The signals from the TAC's were then sent to an Analog-to-Digital converters (ADC) of the Labo MCA, MPS-1600. A dynode signal of the BaF_2 was sent to a preamplifier and then to a delay-line amplifier, while an energy signal of the planar HPGe was send to a shaping amplifier Ortec 671. Their signals were then sent to the ADC's.

The mass-separated beam of $A \sim 105$ nuclei including ^{105}Tc was implanted into an aluminized mylar tape for 600 s, and then delivered to a measuring position at a distance of 1280 mm in 4 s. For the succeeding 600 s the γ-ray counting was carried out, and at the same time the beam was implanted for the next cycle of measurement. The implanting and measuring times, both of 600 s, were set to be approximately twice the mean life of ^{105}Tc.

Typical γ-ray spectra taken with the BaF_2 scintillator and the HPGe detector without any gates are shown in Figs. 3.18 and 3.19, respectively. The data were analyzed under three gating conditions listed in Table 3.2. Gates of for signals from the HPGe detector and the BaF_2 scintillator were set to select the peaks of 82.5, 143.2 or 157.6 keV in Fig. 3.14. Lower limits of gates of the time spectra were set to the 3.5σ of the

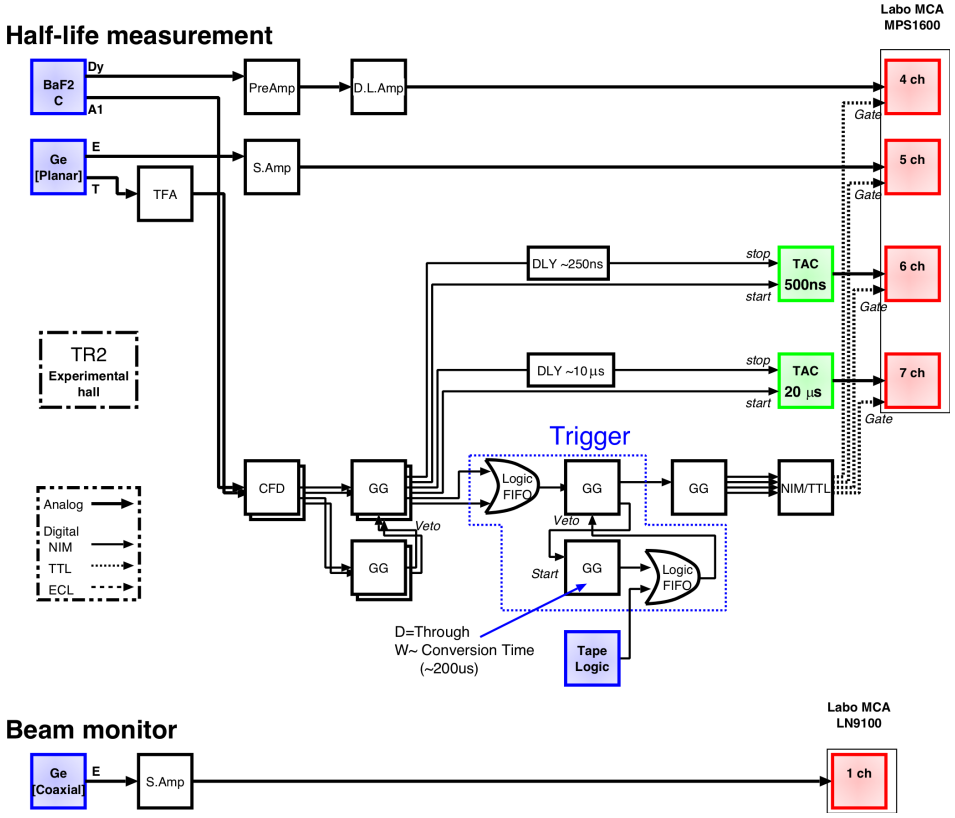

Fig. 3.16 Electronics diagram of ^{105}Ru half-life measurement.

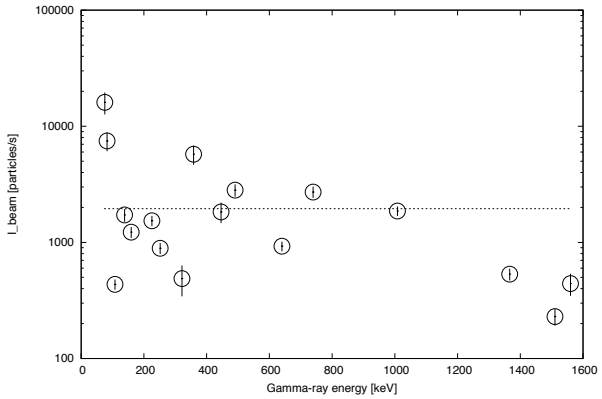

Fig. 3.17 Yield of ^{105}Tc. The intensity of each γ rays is evaluated by the counts of the beam-line-end HPGe. A dashed line is a weighted average, 2×10^3 particles per second.

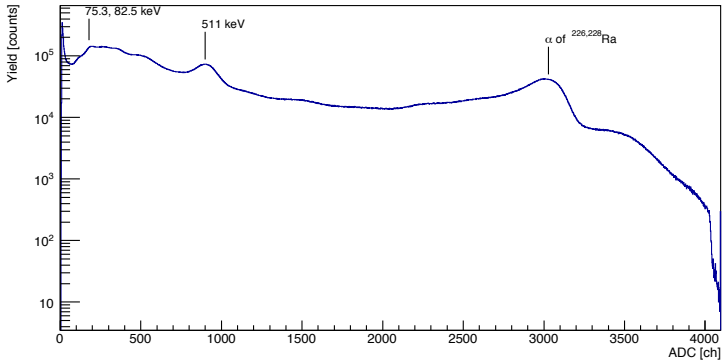

Fig. 3.18 Typical γ-ray spectrum of BaF_2 scintillator without any gates. A large peak near 3000 ch corresponding to 1600 keV is the background caused by radium impurities, which are always present as radium and barium are homologous elements [72]. Its main components are α rays emitted from ^{226}Ra and ^{228}Ra, so that there are no peaks near 1600 keV in the spectrum of HPGe, e.g. Fig. 3.19.

Table 3.2 Gating conditions and half-lives in Fig. 3.20. In addition, timing gates 18.1 to 232.4 ns corresponding to the fitting ranges were applied.

Case	start	gate [keV]	stop	gate [keV]	Half-life [ns]
(a)	HPGe	82.5 ± 3.0	BaF_2	100 to 160	18.2(5)
(b)	BaF_2	50 to 100	HPGe	143.3 ± 3.0	19.5(5)
(c)	HPGe	157.8 ± 3.0	BaF_2	110 to 180	17.8(6)

prompt peak from the prompt position, 18.1 ns. Triple coincidences of these two γ rays and the TAC signal of these two detectors were collected as true events to generate the time spectrum. The obtained γ-ray spectra and time spectra are shown in Fig. 3.20. A single exponential curve with a constant term was applied as a fitting function to the data with the maximum-likelihood method. The data within the 3.5σ of the prompt peak from the prompt position was excluded from the fit. The solid red lines are the best fits to the experimental data. Obtained half-lives were listed in Table 3.2. In the case of (b), the obtained half-life is different from the others more than 3σ, because BaF_2 was unable to distinguish the 75.3- and 82.5-keV γ rays so that the time difference spectrum (b2) in Fig. 3.20 shows mixed decays of the 163.8- and 246.4-keV excited state. Thus the half-life of the 163.8-keV excited state in ^{105}Ru is obtained as 18.0(4) ns as a result of taking the weighted average between (a) and (c).

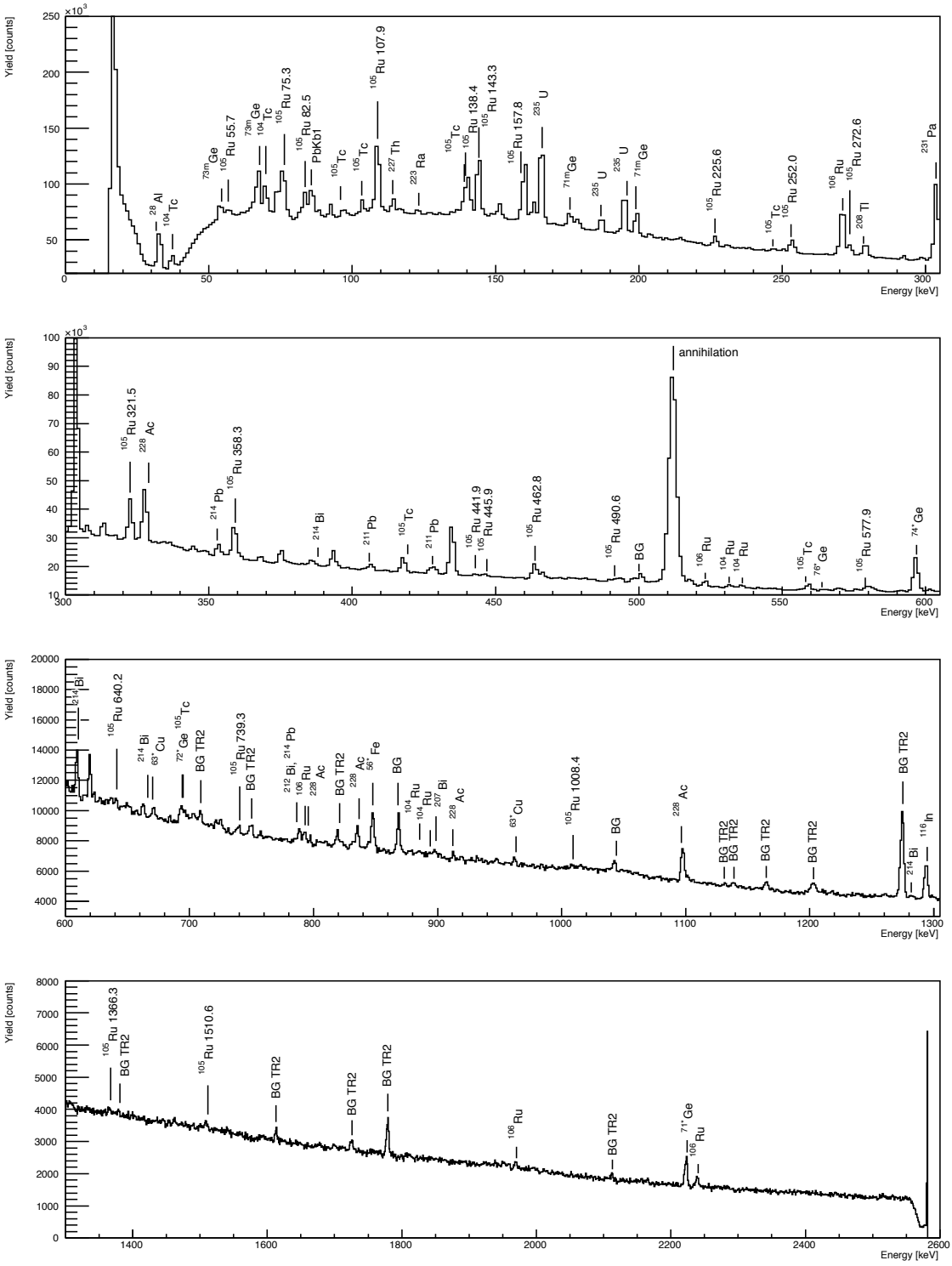

Fig. 3.19 Typical γ-ray spectra of HPGe detector without any gates.

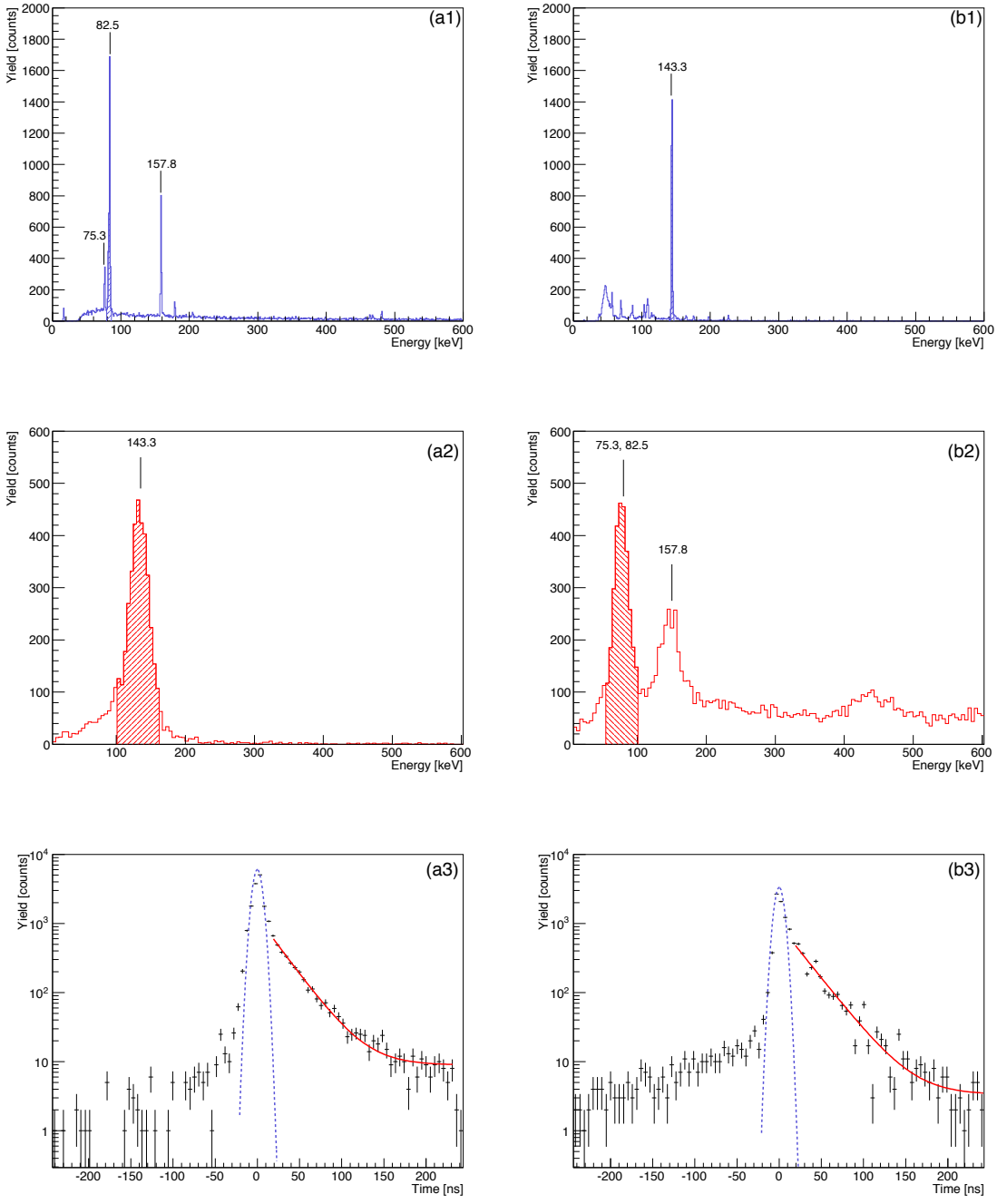

Fig. 3.20 γ-ray spectra from HPGe (1) and BaF_2 (2), and time difference spectra (3) under different gating conditions. The gating conditions (a–c) are shown in Table 3.2. Hatched areas indicate range selected by the individual gates. See text for details.

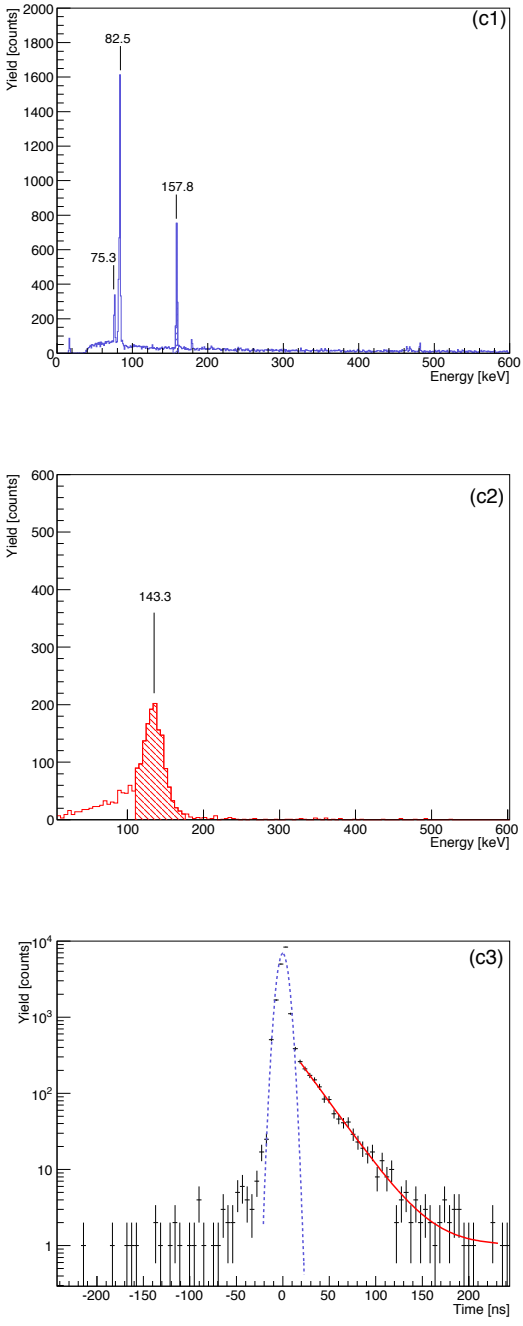

Fig. 3.21 Continued from Fig. 3.20.

3.3.3 Comparison with Holland's report

The lifetime measurements on a number of isomeric states in odd-neutron nuclei including ^{105}Ru was previously reported by Holland [73], and simultaneously compared with a semiempirical prediction based on the shell model with a pairing-plus-quadrupole residual interaction [74, 75]. In this model the residual interaction consists of a short-range part and a quadrupole-quadrupole interaction. The short range part is approximated by a pairing interaction between two neutrons and that between two protons, separately, and leads to an approximate seniority spectrum. The quadrupole-quadrupole interactions between the valence particles associate the particle motions with the collective state. The Bogoliubov canonical transformation was used to introduce the pairing force, by which only the state of zero angular momentum (seniority zero) is affected for two particles in a j level. The Quasi-particle Random Phase Approximation (QRPA) was used to introduce the phonon, which approximately accounts for the the quadrupole-quadrupole interaction between quasi-particles.

The Holland's measurements were an in-beam γ-ray spectroscopy with a pulsed beam from the Argonne tandem Van de Graaff. A schematic illustration of the setup is shown in Fig. 3.22. The obtained half-life of the 164-keV excited state in ^{105}Ru was 55(7) ns.

Our measurement introduced various improvements from the Holland's measurement. Especially,

1) A suppression of the background radiation: In the case of the in-beam γ spectroscopy, there was strong background radiation from a reaction target even if beams were pulsed. In our case, RIs were separated from the target and transported to the measuring position far from the target. Although the low mass resolution caused an unclear separation and a mass-mixed beam 105 ± 2 u, the tape transport system compensated for the unclear separation by the half-life selection.
2) A better time resolution of the TAC: In the Holland's experiment the time resolution was 50 ns/bin while in ours 5.19 ns/bin.

Holland's comparison of the experimental results with a semiempirical prediction was as follows. The $B(E2)$s were calculated from the obtained half-lives using fol-

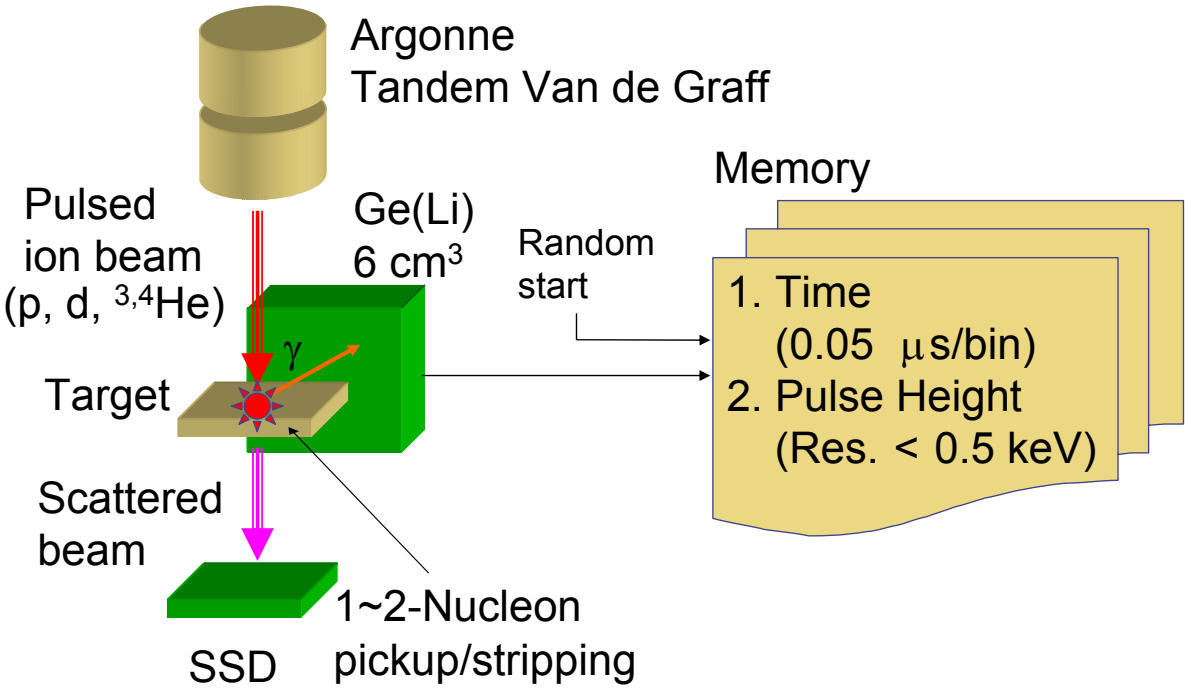

Fig. 3.22 Setup of Holland's half-life measurement.

lowing relations,

$$T(\sigma\lambda) = \frac{\ln 2}{T_{1/2}} = \frac{8\pi\,(\lambda+1)}{\lambda\,[(2\lambda+1)!!]^2}\frac{1}{\hbar}\left(\frac{E_\gamma}{\hbar c}\right)^{2\lambda+1} B(\sigma\lambda), \tag{3.1}$$

$$B(\sigma\lambda; I_i \to I_f) = \frac{1}{2I_i+1}\left|\left\langle I_f \left\| \sigma\lambda \right\| I_i \right\rangle\right|^2, \tag{3.2}$$

$$= \frac{\ln 2}{T_{1/2}}\frac{\lambda\,[(2\lambda+1)!!]^2}{8\pi\,(\lambda+1)}\hbar\left(\frac{\hbar c}{E_\gamma}\right)^{2\lambda+1}. \tag{3.3}$$

Meanwhile, the Hamiltonian of the pairing-plus-quadrupole model was presented by Kisslinger and Sorensen [74]. In this model it is assumed that the low-lying states of spherical nuclei can be treated in terms of two basic excitations, quasiparticles and phonons. For the most part these are treated as separate models of motion. Assuming the residual interaction mixing a one-quasiparticle state with one-quasiparticle-one-phonon states, and ignoring terms involving more complicated states, it was given by Sorensen [75] that

$$\left\langle 0\left|\alpha_j\left|H_{\rm int}\right|(B^\dagger{\alpha_{j'}}^\dagger)_j\right|0\right\rangle = -\bar{\chi}\left(\frac{5}{4\pi}\right)^{\frac{1}{2}}\left\langle j\left|r^2\right|j'\right\rangle C^{2\ j\ j'}_{0\frac{1}{2}\frac{1}{2}}(-1)^{j-j'}(U_jU_{j'}-V_jV_{j'}), \tag{3.4}$$

where ${\alpha_j}^\dagger$ is a quasiparticle creation operator of a j state, $B^\dagger$ is a phonon creation operator, $\bar{\chi}$ is an effective quadrupole-interaction strength, $C^{2\ j\ j'}_{0\frac{1}{2}\frac{1}{2}}$ is the Clebsch-Gordan

coefficient, V_j is the occupation probability of a particle, and U_j is the occupation probability of a hole. The wave function in Sorensen's notation now becomes

$$\psi_j = C_{j00}{}^j \alpha_j^\dagger |0\rangle + \sum_{j'} C_{j'12}{}^j (B^\dagger \alpha_{j'}^\dagger)_j |0\rangle + \cdots . \tag{3.5}$$

The coefficient $C_{j'12}{}^j$ should be obtained by diagonalizing the system Hamiltonian and should not be confused with the Clebsch-Gordan coefficient of Eq. (3.4). That means one needs to have all quantities V_j for the shell under consideration. Assuming the first-order perturbation theory, the one-phonon matrix element is given by

$$C_{j'12}{}^j = \left(\frac{5}{4\pi}\right)^{-\frac{1}{2}} \bar{\chi} \left\langle j \left| r^2 \right| j' \right\rangle C^{2\ j\ j'}_{0\frac{1}{2}\frac{1}{2}} \frac{U_j U_{j'} - V_j V_{j'}}{\Delta E} \tag{3.6}$$

$$= (-1)^{j-\frac{1}{2}} \bar{\chi} \left[B(\text{s.p.}; j \to j')\right]^{\frac{1}{2}} \frac{U_j U_{j'} - V_j V_{j'}}{\Delta E}, \tag{3.7}$$

where $B(\text{s.p.}; j \to j')$ is the single-particle $B(E2)$ for transition $j \to j'$, and ΔE is approximately the phonon energy which we have taken from the energy of the first 2^+ level in the adjacent even-even nucleus. Therefore Sorensen's expression is written for the $E2$ reduced transition rate as

$$B(E2; j_i \to j_f) = B(\text{s.p.}; j_i \to j_f) \left(1 + \frac{2}{5}\chi \frac{B(E2; 0 \to 2)}{\Delta E}\right)^2 \left(U_i U_f - V_i V_f\right)^2, \tag{3.8}$$

where only transitions between one-quasiparticle-one-phonon states and between one-quasiparticle-zero-phonon states are considered. Holland has approximated $\bar{\chi}$ by $\chi \left[B(E2; j_i \to j_f)\right]^{1/2}$.

In Fig. 3.23 is shown a plot of the ratio of the reduced transition rate $B(E2)$ to the single-particle $B(\text{s.p.})$ versus a parameter, derived from the pairing-plus-quadrupole model. The point of ^{105}Ru in Fig. 3.23 is updated by the present result,

$$\frac{B(E2)}{B(\text{s.p.})} = 1.36 \times \frac{55\,\text{ns}}{18.0\,\text{ns}} = 4.16, \tag{3.9}$$

which approaches to the diagonal line. If the relationship Eq. (3.8) accurately represented the data, then one would expect the points to cluster around the diagonal line. However, that is hindered by the large horizontal error arising principally in determination of $\left(U_i U_f - V_i V_f\right)^2$. The relative error in the experimental determination of this quantity increases as $\left(U_i U_f - V_i V_f\right)^2$ decreases. Accordingly, for the points on the left side of the figure the error is probably about 10 times the abscissa. In addition, a noticeable systematic displacement of the data to the lower part of the

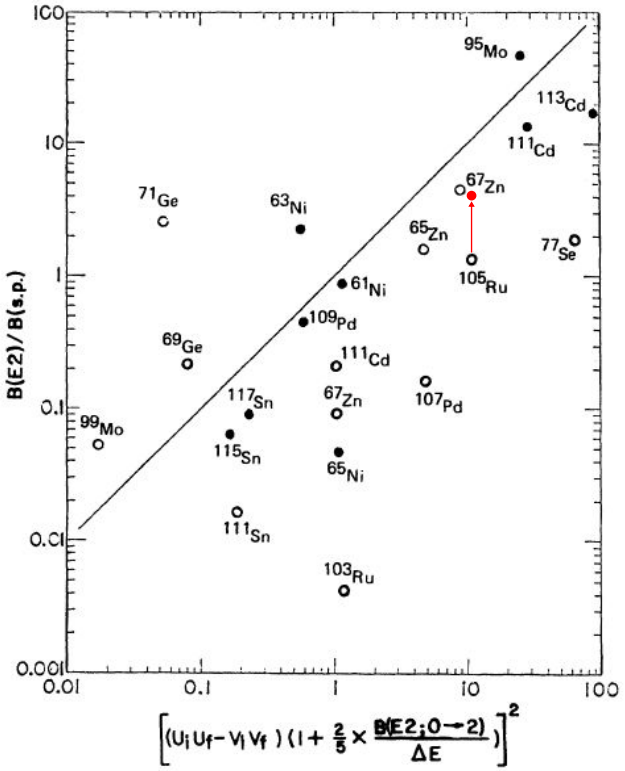

Fig. 3.23 Plot of the ratio of the reduced transition rate $B(E2)$ to the single-particle B(s.p.) versus a parameter, derived from the pairing-plus-quadrupole model, which was obtained from experimentally determined values. (Holland, *et al.* [73]) These were the occupation numbers ${V_j}^2$ from (d,p) and (d,t) reactions, the energy ΔE and $B(E2, 0 \rightarrow 2)$ of the transition in the adjacent even-even isotope, and the quadrupole-coupling constant χ. The diagonal line is given by Eq. (3.8). A closed circle was plotted from transitions for which both (d,p) and (d,t) data exist for determining ${V_j}^2$ and ${U_j}^2$. An open circle was plotted for transitions in which the data were more fragmentary. According to the present result, the point of ^{105}Ru is replotted following the arrow.

diagonal line is caused by both of the systematic error in the quadrupole coupling constant χ and the perturbation theory used by Holland. That is also supported by the present result.

3.3.4 Summary and outlook

■Summary The half-life of the 164-keV excited state in ^{105}Ru was precisely measured for the preparation of the magnetic-moment measurement. The yield of ^{105}Tc produced with the RF-IGISOL at Tohoku University was 2×10^3 pps. The half-life of this level was determined to be 18.0(4) ns of which error was reduced by 6 times. The present result supported the Holland's arguments.

For the γ-PAC measurement the obtained yield of ^{105}Tc is not enough, so that we decide to introduce the sextupole ion-guide (SPIG) [27] into the RF-IGISOL to increase yields of RI beams. Its details are described in Sec. 3.4.

■Procedure of γ-PAC experiment We will measure the magnetic moment of the isomeric state in ^{105}Ru after the introduction of the SPIG. A procedure of the measurement of the nuclear moment of the isomeric state using the perturbed angular correlation of the γ-rays (γ-PAC) is as follows:

1) measurement of the yield of parent nuclei,
2) measurement of the γ-ray yield,
3) measurement of the half-life,
4) measurement of the angular correlation function, $A_{22}^{\rm exp}$, or at least confirmation that $A_{22}^{\rm exp} \neq 0$,
5) selection of material for the stopper and strength of the magnetic filed, and
6) measurement of nuclear moment by γ-PAC.

Just before the above, a measurement of energy levels may need to be measured, but the low-lying energy levels of most nuclei produced using the RF-IGISOL have already been known. 3) is inevitably necessary in the case of the time-integral perturbed angular correlation method, which depends on the precise half-life. 4) also works as a test of the measuring system, and $A_{22}^{\rm exp}$ is necessary for the estimation of required beam time. $A_{22}^{\rm exp}$ for the 82.4–143.2 keV cascade in ^{105}Ru was reported to be $-0.112(8)$ in the case of Ref. 76. For 5) several γ-PAC experiments should be performed with different stopper materials and magnetic fields to obtain a reasonable precession of an unknown magnetic moment in the life. In the case that the necessary magnetic field is up to several tesla a permanent magnet is available as well as Ref. 24. Meanwhile, if the field needs to be more then several tesla, one can use the internal

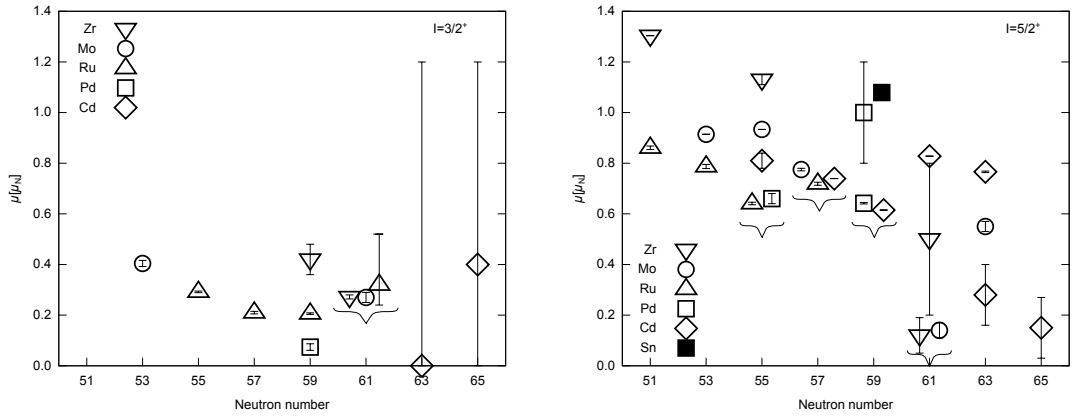

Fig. 3.24 Magnetic moments of $3/2^+$ (left) and $5/2^+$ (right) neutron states in neutron number $A \sim 100$ ($N \sim 60$) region.

field of ferromagnetic material. In the case of Ru, an internal field of 49 T is available in Fe [77, 78].

■Proposal Hinfurtner summarized the g-factors and the magnetic moments of $3/2^+$ and $5/2^+$ states in the mass region $A \sim 100$ [78]. We add recent results listed in Ref. 5 to it and shows new systematic trend of the magnetic moment of $3/2^+$ ($\nu d_{3/2}$) and $5/2^+$ ($\nu d_{5/2}$) states in Fig. 3.24*[1]. According to Fig. 3.24, g-factor of the 164-keV excited state in ^{105}Ru ($N = 61$) might approximately be 0.3 for $3/2^+$ or 0.14 for $5/2^+$. Its γ-PAC measurement might be very similar to that of the 90-keV excited state in ^{99}Ru [79], because its half-life and spin are 20.7(3) ns and $3/2^+$, respectively. The time-pattern of the angular-correlation precessing obtained in Ref. 79 is shown in Fig. 3.25 as the reference of that of ^{105}Ru.

*[1] These magnetic moments are only used for a prediction of the g-factor of the excited state in ^{105}Ru, though that of the nuclei in a vicinity of $N \sim 60$ would be related to the sub-shell close.

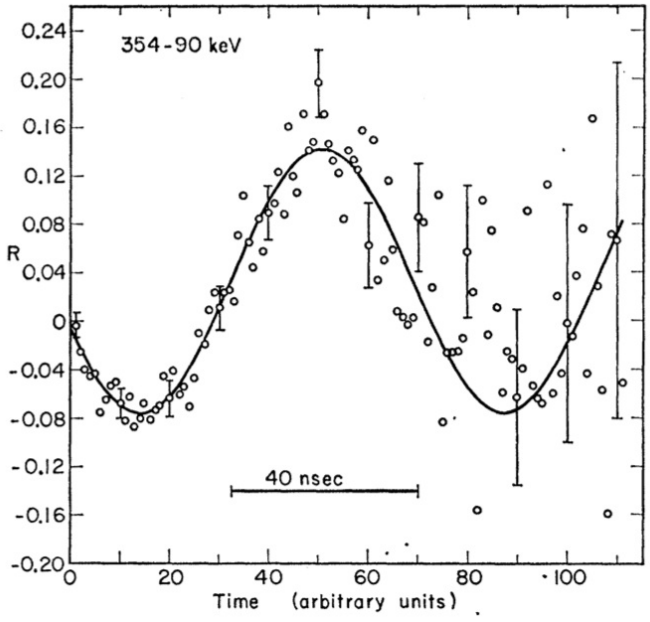

Fig. 3.25 Time-pattern of angular-correlation precessing of 90-keV excited state in ^{99}Ru in external magnetic field of 41.6 kG using liquid source. (Matthias, *et al.*[79])

3.4 Development of sextupole ion beam guide for improvement of RF-IGISOL

3.4.1 Introduction

■Motivation Yields of unstable nuclei with the previous skimmer-system IGISOL were several thousands particles per second (pps) as shown in Fig. 3.12, and insufficient for actual magnetic-moment measurements. To determine the g-factor of an excited state in Radioactive Isotopes (RI) using the perturbed angular correlation of γ-rays (γ-PAC), multiple measurements should be performed with different stopper materials and magnetic fields to obtain a reasonable precision of for the magnetic moment in their own life. To achieve such a measurement the yield should be at least one order of magnitude higher. For example, on the measurement of g-factor of an isomeric state in ^{109}Rh performed by Miyashita using Tohoku RF-IGISOL [24] the yield of ^{109}Ru was 6×10^3 pps, with which the experiment required three times beam-time of five days. In another case, in Sec. 3.3 the 2000-pps ^{105}Tc beam gave only the half-life measurement of the isomeric state in ^{105}Ru. If the yields of the RIs listed in Table 3.3 multiply, their magnetic moments will be able to be measured with Tohoku RF-IGISOL and γ-PAC.

One of the solutions to increase the yield is to improve the Mass Resolving Power (MRP), because these experiments employ at most 25 % of the mass-separated RI beam for spatial distribution of the beam was larger than acceptable width of the measuring device as described in Sec. 3.2.2. In the case of IGISOL a deterioration of the MRP are brought by collisions with a residual gas molecules during acceleration and transportation from an exit hole of the high-pressure gas cell to a high-vacuum region through a skimmer electrode with an electric field. In order to increase the yield one have to apply a sufficiently strong electric field to the skimmer region at the expense of MRP, because of both threshold of the electric field to well focus the extracted ions as shown in Fig. 3.26 and deterioration of the MRP proportional to a ratio of the skimmer voltage to the acceleration voltage as shown in Fig. 3.27. In order to overcome such difficulties the distance between the exit hole and the skimmer electrode are extended to increase the evacuation conductance just downstream from the exit hole, and a SextuPole Ion-Guide (SPIG) are introduced into this region in order to extract ions with low electric fields, which converge scattering and diffusing

Table 3.3 Candidates of magnetic-moment measurement with Tohoku RF-IGISOL and γ-PAC in $A \sim 110$, except for ^{109}Rh. Yields were obtained with the skimmer-system RF-IGISOL.

Isomer	Spin Energy [keV]	Half-life	Cascade γ_1 [keV] γ_2 [keV]	Parent	Half-life of β decay	Cross section of fission reaction [mb]	Yield [pps]
^{103}Tc	$3/2^+$ 83.4	~40 ns	unknown 83.4	^{103}Mo	0.53 s	28	$\sim 10^3$
^{105}Tc	$(5/2^+)$ 85.4	20.8 ns	64.1, 218 85.4	^{105}Mo	35.6 s	20	not evaluated
^{105}Ru	$3/2^+, 5/2^+$ 163.8	18.0 ns	82.5 143.2	^{105}Tc	7.6 m	21	2×10^3
^{107}Ru	$(^+)$ 106.3	65 ns	70.7, 354 106.3	^{107}Tc	21.2 s	18	2×10^3
^{113}Cd	$5/2^+$ 316.2	10.8 ns	392 315	^{113}Ag	68.7 s	61	unknown
^{130}Te	$(6)^+$ 1815.4	9.8 ns	331 185	^{130}Sb	6.3 m	56	$\sim 10^3$
^{109}Rh [24]	$3/2^+, 5/2^+$ 226.0	1.66 µs	183, 116 226	^{109}Ru	34.5 s	16	6×10^3

ions and guide them to high-vacuum acceleration region through the poor vacuum region.

■Background A yield of ^{54}Co produced using Tohoku IGISOL had a threshold of the skimmer voltage as shown in Fig. 3.26, according to Ref. 64 of Yoshii. This threshold gave presumption that the ions should collide several times with residual molecules during passage from the exit hole to the skimmer electrode. Thus, an energy spread of the ions should depends on the distribution of number and positions of the collisions.

A deterioration of the MRP is proportional to the skimmer voltage as shown in Fig. 3.27. In addition, Figure 3.27 shows that the decrease tendency of the MRP could be moderate to apply much stronger electric field than the threshold but an absolute value of the MRP remained low. Such a situation is named *high-voltage extraction*.

In order to defeat the *high-voltage extraction* and to realize the high MRP, the critical requirement is simply suppression of the skimmer voltage, namely realization of the *low-voltage extraction*. Additional requirements are introduction of the focusing device of the extracted ions against scatter and diffusion in the poor vacuum region,

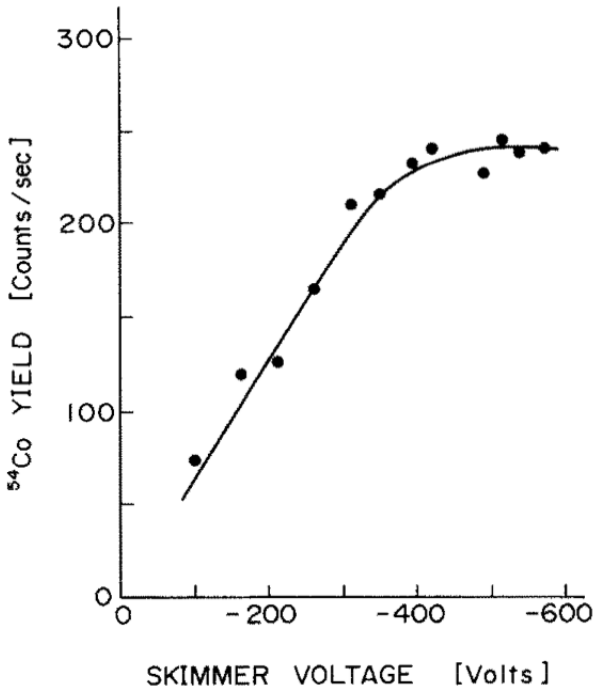

Fig. 3.26 Yield of mass-separated ^{54}Co at the tape position as a function of the skimmer voltage (Yoshii *et al.* [64]). In this case, a threshold is −400 V, for almost ^{54}Co ions were led to the acceleration section against a diffusion and a straggling as a result of collisions with residual gas molecules.

and improvement of the vacuum just downstream from the exit hole.

The *low-voltage extraction* can be achieved due to installation of a linear radio-frequency multipole ion-guide after the exit hole, where a distance between the exit hole and the skimmer electrode are extended in order to increase a evacuation conductance just downstream from the exit hole. The multipole ion-guide consists of multiple parallel rods arranged on a single circle with equal angular intervals. The ions are injected into the multipole ion-guide by the helium jet and the low electric field, and radially focused by a radial confinement field generated inside the multipole ion-guide by applying RF voltages between adjacent rods. Meanwhile the helium gas is evacuated by pumping through the spaces between the rods. The ions reaching the end of the multipole ion-guide, where it is high vacuum, are accelerated without the collisions with the helium and the residual molecules. According to Ref. 27, the optimum transport efficiency is more than 90 % and the energy spread of the transported ion beam is smaller than 1 eV.

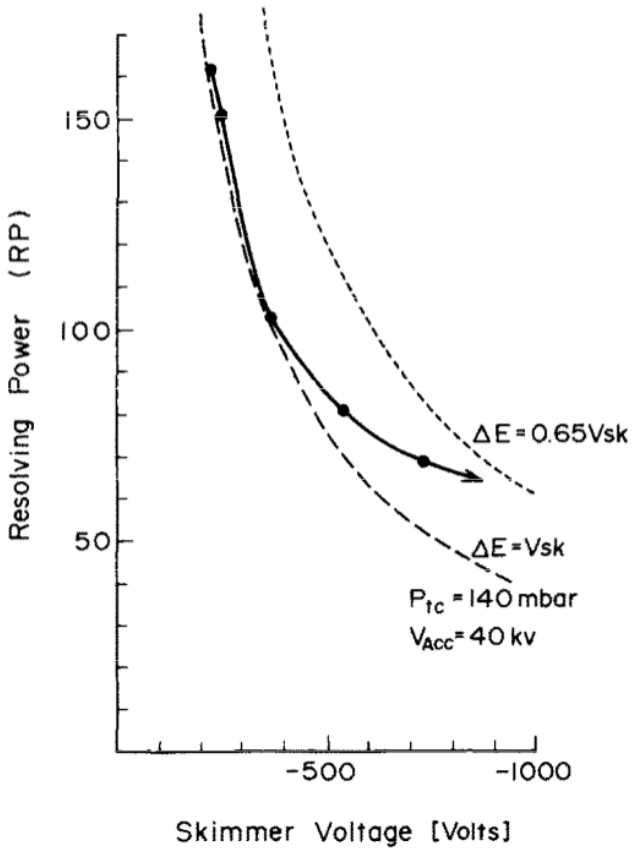

Fig. 3.27 Mass resolving power (MRP) of the $A = 16$ (O^+) beam as a function of the skimmer voltage. The MRP is defined as $M/\Delta M$ at fwhm The broken curve shows the values calculated by assuming the energy spread of the ions equal to the skimmer potential ($\Delta E = e|V_{sk}|$) while the dotted curve the value calculated by assuming $\Delta E = 0.65e|V_{sk}|$ (Yoshii *et al.* [64]). According to Fig. 3.26 and this figure, in order to increase the yield one have to apply enough strong electric field to the skimmer region at the expense of the MRP, because of both threshold of the electric field to well converge the extracted ions and deterioration of the MRP proportional to a ratio of the skimmer voltage to the acceleration voltage.

3.4.2 Principle

The potential around the central axis produced by $2N$ parallel rods supplied with RF voltages, $V_{RF}\cos(\omega t)$, in opposite phase, is represented in cylindrical coordinates by

$$U = (\frac{r}{r_0})^N V_{RF}\cos(N\theta)cos(\omega t), \tag{3.10}$$

where r is the radial coordinate, r_0 is the radius of the inscribed circle formed by the rods, V_{RF} is the amplitude of the RF voltage at frequency $\omega/2\pi$, θ is the azimuthal

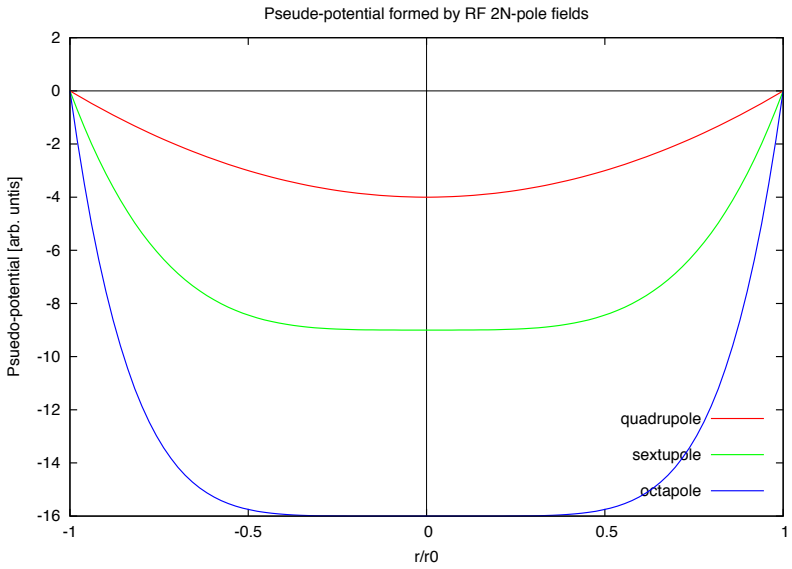

Fig. 3.28 Psudepotential formed by multipole RF field.

angular coordinate with respect to the axis of symmetry z, and t is the time. The potential shows that the RF electric field in the SPIG only affects the radial motion of charged particles and never affects the drift motion along the z-axis of the SPIG. The radial motion of the particle is conveniently divided into a fast oscillatory part and a slow average part. When the frequency ω is high enough, the fast oscillatory part becomes negligible and the slow average part is close to an exact trajectory. The average trajectory is described by a simple periodic motion under the action of a conservative force field derived from the effective potential U_{eff} given by

$$U_{\text{eff}} = \frac{N^2}{4m\omega^2}\left(\frac{V_{\text{RF}}}{r_0}\right)^2\left(\frac{r}{r_0}\right)^{2(N-1)}. \tag{3.11}$$

The concept of the effective potential is useful in understanding the physical characteristics of the multipole ion-guide. The maximum potential depth with the same r_0 and V_{RF} increases as N increases, as presented in Fig. 3.28. Thus, we will introduce the ion-guide with higher N after tests of the present SPIG is finished.

3.4.3 Design

The SPIG consists of six molybdenum rods of 1.0 mm in diameter and 106.5 mm long which are mechanically supported on a single circle with equal angular intervals and electrically insulated by three glass ceramics (photoveel) as shown in Figs. 3.29 and 3.30. A diameter of the inner circle r_0 of the SPIG is 1.8 mm. The SPIG is fixed on

a linear moving devices of which a maximum range is 7 mm. A distance between the exit hole of the RF carpet and the SPIG is sat to 0.5 mm. The rods are supplied with alternating RF voltages between adjacent pairs with opposite phases. Typical RF voltage is approximately 50 V at 2 MHz. The geometry of the RF carpet, the SPIG assembly and the extractor electrode is shown in Fig. 3.29, and a photo of the SPIG assembly is shown in Fig. 3.31.

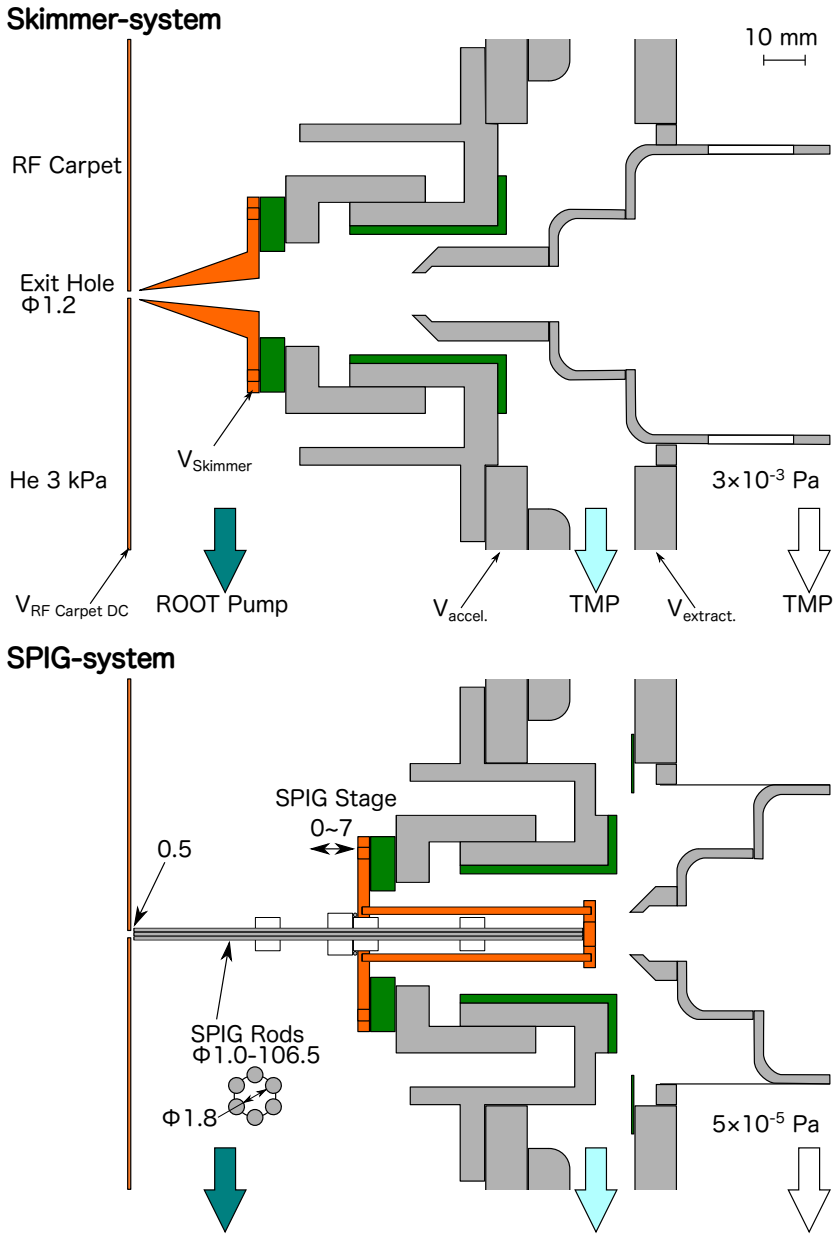

Fig. 3.29 Structures of the RF-IGISOL with the skimmer system and the SPIG system.

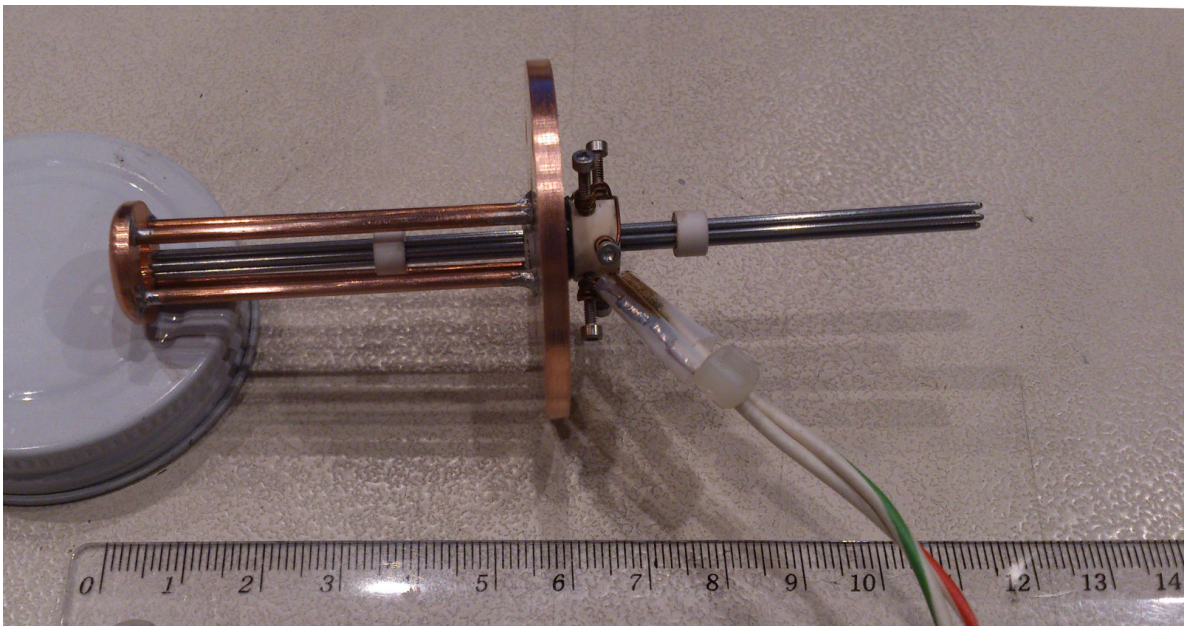

Fig. 3.30 Photo of SPIG electrode, end electrode and ceramic holders.

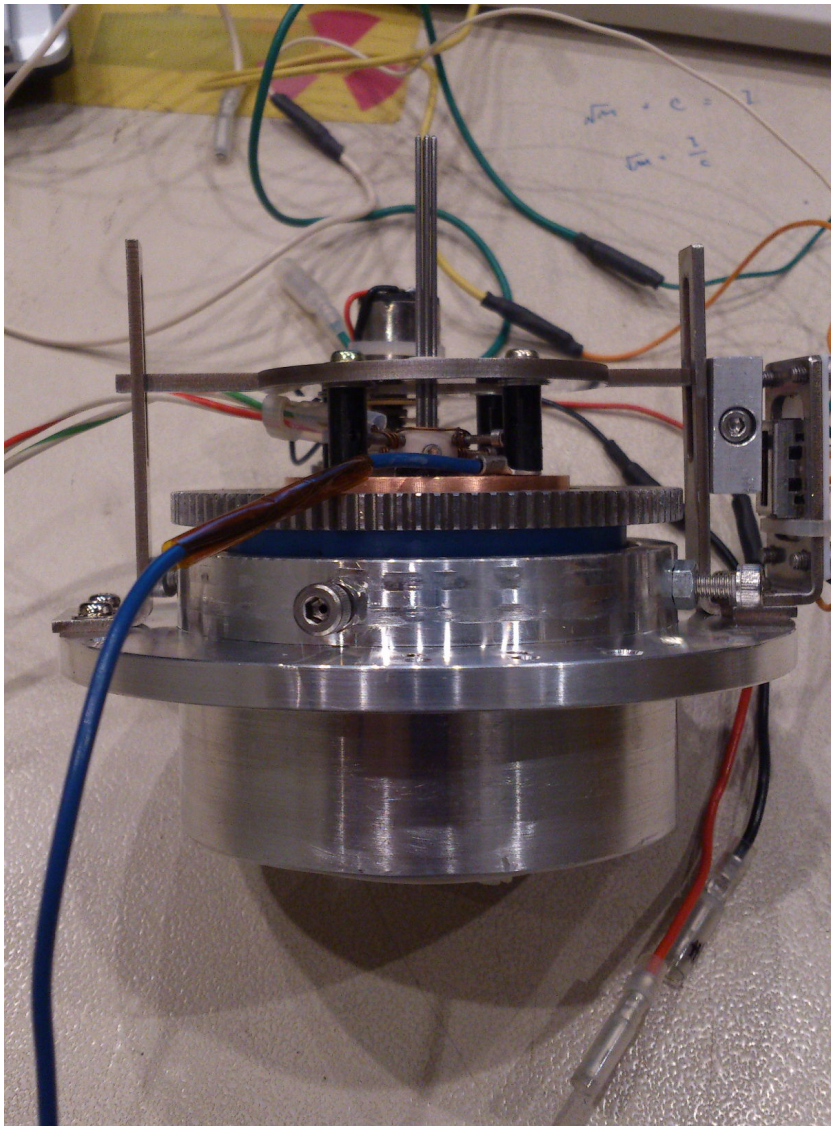

Fig. 3.31 Photo of the SPIG assembly. The SPIG is fixed on a linear moving devices of which a maximum range is 7 mm.

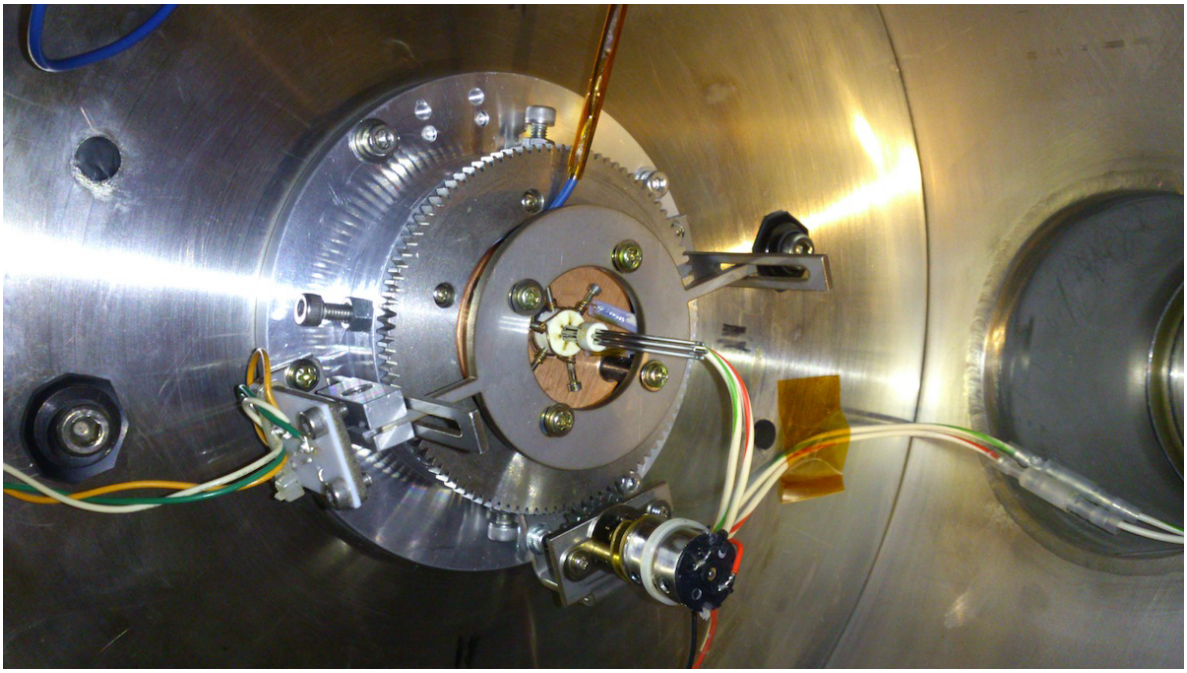

Fig. 3.32 Photo of the SPIG assembly mounted on wall between skimmer region and extractor region in Tohoku RF-IGISOL.

3.4.4 Performance check

■Mass resolving power Performance of the SPIG-system RF-IGISOL was tested by measurement of mass-separated atomic and molecular ions in off- and on-line experiments. Natural xenon gas mixed in the He buffer gas and the xenon atoms were ionized by the proton beam at energy of the 50 MeV accelerated by the 930 cyclotron. A current of extracted Xe isotopes ions after mass separation has been measured using an electron multiplier tube (EMT), R5150-10 of Hamamatsu Photonics, placed at end of the beam line. Comparison of mass spectra between SPIG-system and skimmer-system is shown in Fig. 3.33. This spectrum shows that the mass resolving power at fwhm (MRP) improved to greater than 260. In addition, the spot size of the beam at the end of the beam line measured 1 cm in diameter. Thus, the almost beams should enter the measuring device and then the yield at the detector improves 4 times larger than that with the skimmer-system RF-IGISOL.

Therefore, the main purpose of the introduction of the SPIG is archived, but the MRP of at the least 260 is not so large using the SPIG and would be brought by not optimized optics. The optics of the present Tohoku RF-IGISOL were extremely changed from that of the original mass separator satisfying the double achromatic condition, because the positions of the exit hole of the gas cell, the skimmer electrode and the extractor electrode moved downstream by 300 mm when the volume of the gas cell enlarged. Improvement of the optics of Tohoku RF-IGISOL will be necessary.

Figure 3.33 shows the yield of $^{128-132,134,136}$Xe as much as that of background impurities. The ionization potentials of the impurities are not as high as that of helium, so that the Xe isotope ions are neutralized under collisions with them.

■Impurities in gas cell In order to identify the impurities in gas cell, mass spectrum was measured up to $A = 300$ with a spark-discharge ion source. As shown in Fig. 3.34, a result suggests that the impurities exist overall mass number. Background impurities would be out gases from plastics of the RF carpet and the cylindrical electrode, and oils from the pumps.

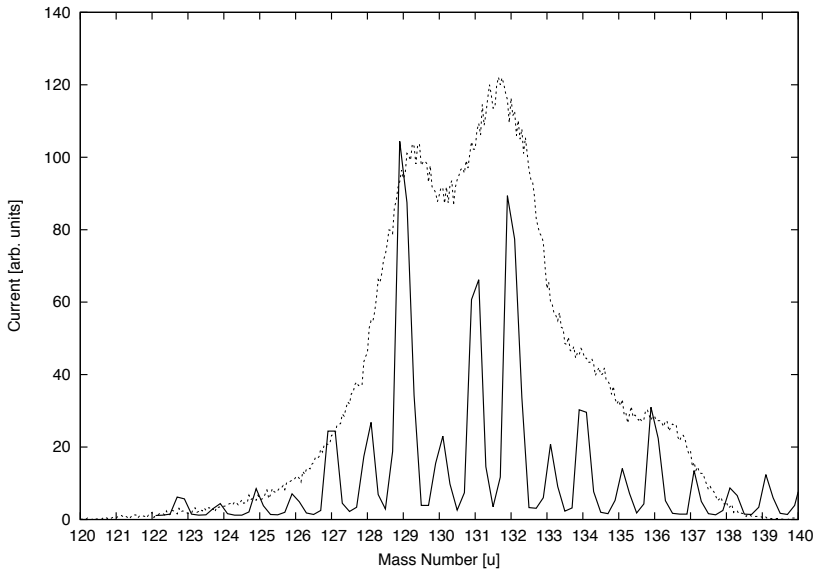

Fig. 3.33 Comparison of mass spectra between SPIG-system and skimmer-system. Current of the ions is plotted as function of mass number. A solid line and a dashed line are for the skimmer-system and the SPIG-system, respectively.

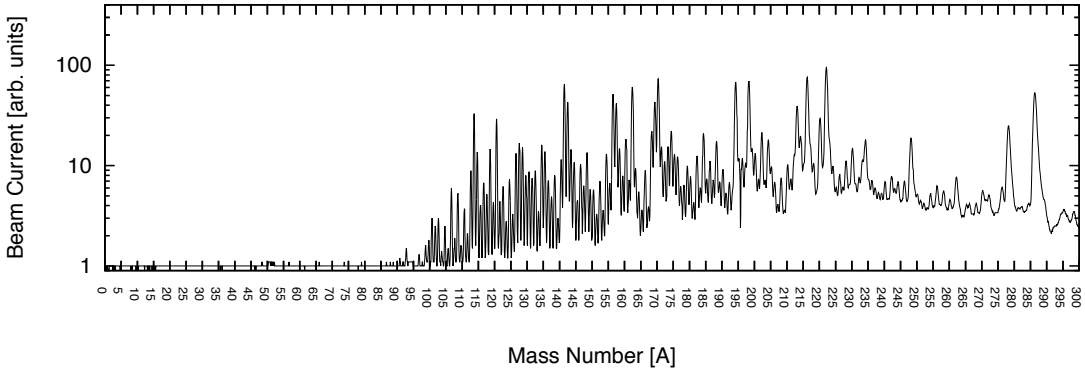

Fig. 3.34 Mass Spectrum without Xe gas, only He gas. Background. Discharge ion source.

3.5 Conclusion

3.5.1 Summary

■Tohoku RF-IGISOL The Ion-Guide Isotope Separator On-Line (IGISOL) is a kind of the ISOL specialized for unstable nuclei having shorter half-lives ($\leq$ 0.5 s) and higher melting temperatures ($\geq$ 1000 K) [20, 21]. The principle of IGISOL is as the following: radioactive ions recoil out of the thin target after the nuclear reaction and are thermalized in a helium buffer gas after many collisions. The important point is in the fact that some fraction of these thermalized atoms are still in 1+ charge state, since the ionization potential of He atom has a larger value than heavier atoms. This is an astonishing fact from point of view of atomic and molecular physics in a gas phase. Therefore, an IGISOL-system does not need to re-ionize the thermalized atoms. The ions are transported by a helium flow out of the target chamber and are guided into the mass separator by an electric field.

Since the last decade, we have developed an ISOL of radio-frequency ion-guide type in CYRIC of Tohoku University, named "Tohoku RF-IGISOL". It has following unique properties of the target gas cell: the volume of the target cell is larger and the pressure of helium gas filling the target chamber is higher than conventional IGISOL to enlarge the acceptable range for recoiled fragments, and then a combination of DC and inhomogeneous RF electric fields are applied to collect recoiling fragments to an exit hole [22–25].

■Measurement of half-life Using Tohoku RF-IGISOL, half-life of the 163.82-keV excited state in unstable nucleus ^{105}Ru was measured. The half-life was determined to be 18.0(4) ns, of which error was reduced to one sixth of the previous one measured by Holland *et al.* [73]. Following the discussion in Ref. 73 the result was compared with a semiempirical prediction based on shell model with the pairing-plus-quadrupole residual interaction. The present result supported the Holland's arguments.

■Installation of SPIG The result of this measurement also realized that the yield of the ^{105}Tc of 2×10^3 particle per second was not enough for measurement of the g-factor of the excited state in ^{105}Ru by γ-PAC. One of solutions to increase the yield was the improvement of the mass resolving power (MRP), because this experiment

employed at most 25 % of the mass-separated ^{105}Ru beam for spatial distribution of the beam was larger than acceptable width of a measuring device. In the case of IGISOL a deterioration in MRP are caused by collisions with residual gas molecules during the acceleration from the exit hole of the high-pressure gas cell to a high-vacuum region through a poor-vacuum skimmer region by an electric field. In order to increase the yield one have to apply a strong electric field to the skimmer region at the expense of MRP, because of both threshold of the electric field to well focus the extracted ions and deterioration of the MRP proportional to the ratio of the skimmer voltage to the acceleration voltage. In order to defeat such difficulties the electric field between the exit hole and the skimmer electrode must be kept low, and the evacuation conductance must be increased to extend the distance. Therefore, a SextuPole Ion-Guide (SPIG) has been introduced, which could focus scattering and diffusing ions and guide them to the high-vacuum acceleration region.

■Performance test of SPIG The SPIG was tested using a proton beam at energy of 50 MeV accelerated by the 930 cyclotron. A xenon gas was mixed into the buffer helium gas. The MRP at fwhm was measured using the ions of xenon isotopes ionized by the proton beam, and then improved at least 260 in the $A \sim 130$ region. Thus, most of the beam particles would enter the measuring device and then the yield at the detector improves by a factor of four from that with the skimmer-system RF-IGISOL.

3.5.2 Outlook

■Next step The next step for the SPIG-system RF-IGISOL is the extraction the RI and the measurement of g-factors listed in Table 3.3.

■Increase of pressure of gas cell Furthermore, the pressure of helium gas filling the gas cell will be able to increase in order to extend an acceptable range of stopping of recoiling unstable nuclei. That is one of the unaccomplished purposes of Tohoku RF-IGISOL. In the skimmer-system RF-IGISOL the pressure was limited to only several kilo pascal by vacuum of the acceleration region of 10^{-3} Pa. The pressure of the acceleration region was improved to 10^{-5} Pa by the SPIG-system, and the pressure of the gas cell, consequently, can be increase until it reaches the pumping limit for a root pump. It is expected at least 10 times as high as that of the SPIG-system. Besides, the back plate of the RF carpet has to be strengthened because of an apprehension that it is too weak to keep such a 10-kPa pressure as shown in Fig. 3.8.

■Optimization of parameters The optimization of parameters for Tohoku RF-IGISOL listed in Table 3.1 is required. The MRP of at least 260 at fwmh is not so large using SPIG and would be brought even by unoptimized optics. The optics of the present Tohoku RF-IGISOL were dramatically changed from that of the original mass separator satisfying the double achromatic condition, because the positions of the exit hole of gas cell, the skimmer electrode and the extractor electrode moved downstream by 300 mm when the volume of the gas cell was enlarged. The output beam of the SPIG has narrow distributions in position, momentum and emission angle, so that the parameters of the current optics could be tested well. Thus, the obtained parameters involving the addition of new lens will achieve very high MRP's and give very small spot sizes of the beam at the measuring device.

■Change of cylindrical electrode to RF carpet Although the present side-wall cylindrical electrode of the RF-IGISOL is just a DC electrode, it will be replaced to the RF carpet in order to suppress the neutralization by collisions of recoiling unstable ions with the side wall.

■α-decay recoil source An α-decay recoil source, ^{227}Ac/^{223}Ra, described in Ref. 80, will have to be introduced for the off-line development. For the ionization in the off-line development, currently, an arc-discharge or a radiation of an activated uranium target in the gas cell were employed. These methods do not have stability nor reproducibility. Hence, the yield of ions can not be estimated exactly.

■Prospect Detailed discussion of the nuclear structure requires the systematic data, such as that of the electric quadrupole moments of neutron-rich aluminum isotopes discussed in Sec. 2.4. However, Figs 1.1 and 3.24 show that known magnetic moments in this region are rare, except for those of alkali elements, alkaline-earth elements and stable nuclei. The beams of unstable nuclei produced using ISOL are low in energy and well-focused. Consequently, they are very suitable to systematic and precise measurements of not only magnetic moments but also half-lives, transition probabilities and masses, because obtained nuclei are easily stored and trapped. Furthermore, IGISOL could produce short-lived neutron-rich nuclei without depending on chemical properties of the nuclei in contrast to the thick-target ISOL. We will promote the improvement of IGISOL as well as development of new magnetic-moment measuring method such as cross-polarization β-NMR [81] and atomic beam method explained in Chap. 4.

Chapter 4

Development of Atomic Beam Resonance Method for Radioactive Isotopes (RIABR)

4.1 Introduction

A number of nuclear moments have been measured by using spin-polarized radioactive isotope (RI) beams from the projectile fragmentation reaction combined with the nuclear magnetic resonance *via* change in the angular distribution of β-rays (β-NMR method). Known magnetic moments particularly in the light-mass region are shown in Fig. 4.1. This approach, however, requires several conditions to be fulfilled. One is to find a suitable host material in which the spin polarization of the implanted RI can keep long enough, since the spin relaxation time is very sensitive to chemical properties of the implanted atom and the host material. Another important factor is the degree of β-ray asymmetry parameter which largely determines the performance of measurement.

To avoid the difficulties forecasted in such requirements when measurements of nuclear moments are extended to heavier mass region, we attempt to develop a new method which involves a thermal-energy spin-polarized RI beam, which is called the Atomic Beam Resonance method for RI (RIABR). This method is an extended application of the Rabi resonance method [28–30] to RI. This has an advantage that neither special host materials nor large β-ray asymmetries are required, since the magnetic resonance is performed in flight and the resonance is detected simply *via* change of a

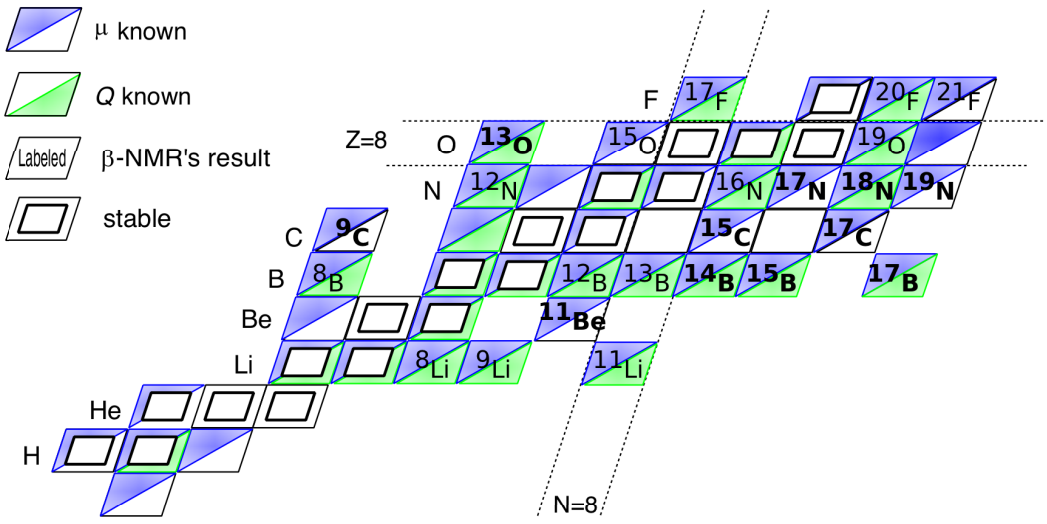

Fig. 4.1 μ and Q moments of ground state measured by β-NMR in light-mass region [5, 55, 82–85]. The bold labels are particular results with spin-polarized beams from fragment separators.

position of the RI reaching the end of the apparatus.

The ABR also works as the spin-direction filter for the non-spin-polarized atomic beam. Consequently, this gives spin-selected and also thermal energetic beams. Such a beam allows us application to surface science and a test of fundamental symmetries such as the time-reversal invariance.

4.2 Design and construction of RIABR device

4.2.1 Basic design concept of RIABR

The RIABR method needs the thermalized and neutralized RI for the Stern-Gerlach principle of ABR. In the following, a method to produce thermal-energy spin-polarized RI atomic beams after the projectile-fragment process is proposed. A schematic view of the setup is shown in Fig. 4.2. First, the RI beam produced using the projectile-fragment separator are stopped in a cell filled with a noble gas, and consequently thermalized and neutralized by the gas. Then, the RI atoms are ejected together with the gas into vacuum from the cell passing through a Laval-type nozzle mounted on the exit of the cell so that the gas flow is spouted out to forward angles. The spread of the angle of gas flow can be set within 3 to 4° as reported in Ref. 86. The temperature of the gas is kept as low as 80 K in order to increase the stopping power of the gas cell and to reduce the velocity of ejected atoms.

Then, a series of sextupole (hexapole) magnets is installed to converge a certain spin components of the atomic beam from the nozzle of the cell. The force on the atoms in a strong magnetic multipole field is given as

$$F(r) = \mu \nabla B(r), \tag{4.1}$$

where μ and $B(r)$ are the atomic magnetic moment and the strength of the magnetic field, respectively. The field distribution $B(r)$ within the magnet bore can be calculated using formulae derived by Halbach [87]. For the sextupole magnet consisting of M wedge-shaped segments, one finds:

$$B(r) = \left(\frac{r}{r_i}\right)^2 B_0 \frac{3}{2}\left[1 - \left(\frac{r_i}{r_o}\right)^2\right] \cos^3(\pi/M)\, \frac{\sin(3\pi/M)}{3\pi/M}, \tag{4.2}$$

where r_i and r_o denote the inner and outer radii of the sextupole magnet, and B_0 the residual field. In our calculation, the sextupole magnet is assumed to consist of 24 segments of permanent magnets, of which schematic cross section is shown in Fig. 4.3 with the easy axis direction indicated by an arrow in each piece. The magnetic field at the pole tip is about 1.5 T. The radius r_i is varied over a region 0.5 to 3 cm while r_o is fixed at 7.5 cm. The calculated field of the sextupole magnet using Eq. (4.2) is compared with $B(r)$ using the electromagnetic finite-element simulation code, OPERA [88]. Figure 4.4 shows a good agreement. Therefore, the $B(r)$ value

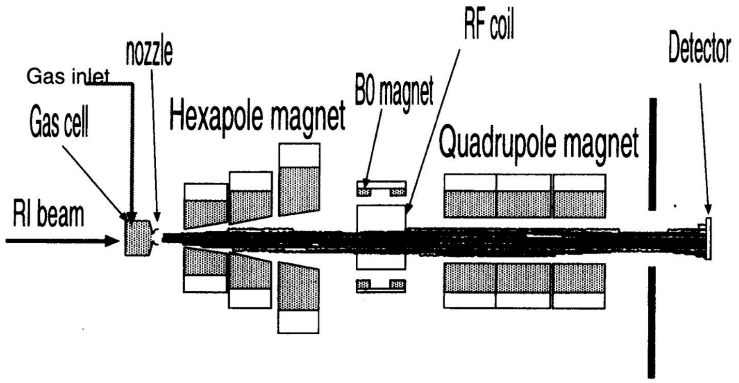

Fig. 4.2 Schematic view of the RIABR device. The trajectories indicate the results of simulation for RI atoms with spins parallel to the field (low-field seeker) when the RF field is applied.

from Eq. (4.2) is employed to simulate trajectories for atoms. At the final stage, a quadrupole magnet is installed to obtain a polarized atomic beam. By selecting a direction of a spin of the beam, a high degree of polarization is expected. In the low-field region located between the sextupole magnet and the quadrupole magnet, an RF field is applied in order to induce transitions between different spin states. The β or γ radiation detector is located behind the quadrupole magnet. When the RF frequency is resonant with a transition between different spin states, the spin transition occurs, the deflection of the flight path changes and then the detector counts the transmitted atoms. Table 4.1 shows the simulated result of the transmissions of RI atoms. Here, the "transmission" is defined as a ratio of the number of atoms reaching the detector to that of atoms released from the nozzle.

Since the ABR method can separate the spin states spatially, it has highly sensitive detection method to magnetic moment, and furthermore is a very universal method for unstable nuclei. In the case of RIABR, we can use the sensitive radiation-detection method for the spin-selected RI atoms. Although it needs complicated devices to obtain a thermalized and neutralized RI atomic beam, it might be very sensitive method to measure nuclear moments for RIs in the regions far from stability.

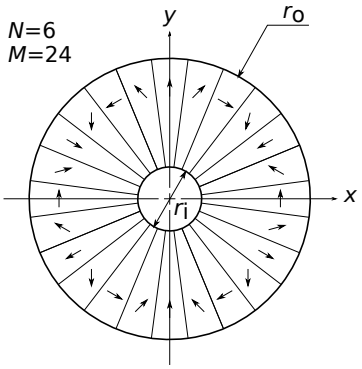

Fig. 4.3 Schematic cross section of a 24-piece sextupole magnet with the easy axis direction indicated by an arrow in each piece.

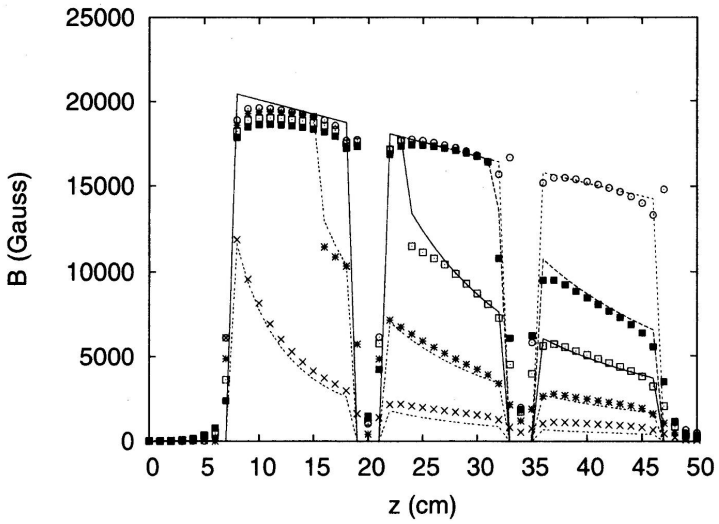

Fig. 4.4 Comparison of $B(r)$ field obtained from Eq. (4.2) in the text (dotted lines), with the simulated value from the code OPERA (dots). The three sextupole magnets are assumed to be 12 cm long each with 2 cm interval spacing.

4.2.2 Construction of RIABR device

Overview of RIABR apparatus

The RIABR device consists of an atomic beam source, "A" magnet, "B" magnet, "C" magnet, a RF cavity, and an RI detection device as shown in Fig. 4.5. The development of an atomic beam source including a stopping cell and a neutralizer is described in Sec. 4.3 in detail. A sextupole magnet is selected as the "A" magnet and its construction is described latter in this section. The quadrupole electromagnet was installed as

Table 4.1 Simulation results for the transmission for the various mass numbers of RI atoms.

A	Transmission [%]	
	RF-On	RF-Off
20	17.75	0.15
30	27.27	0.50
40	33.12	0.62
50	33.02	1.00
60	29.34	1.15
70	26.42	1.39
80	21.73	1.59

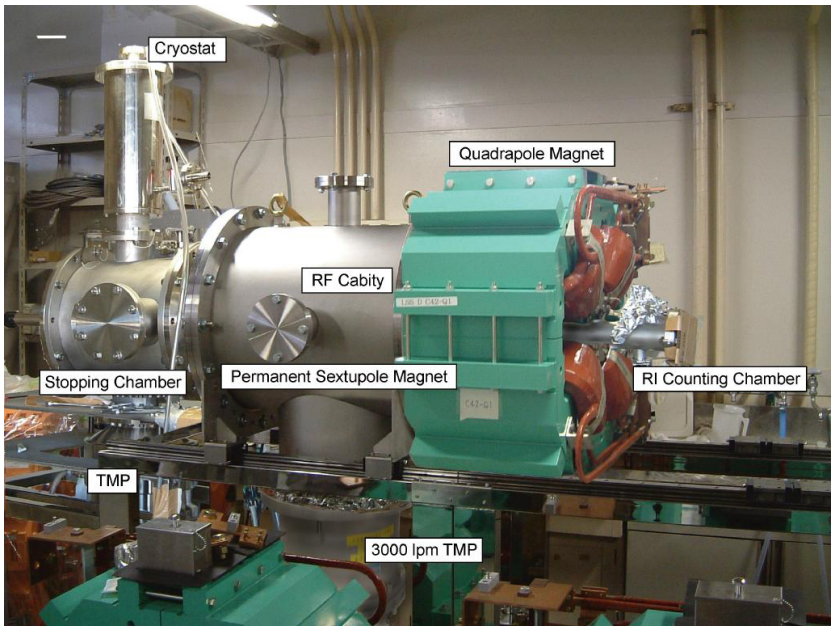

Fig. 4.5 Overview of the RIABR apparatus of the present.

the “B” magnet. The nuclear magnetic resonance section consisting of the “C” magnet and the RF cavity will be developed using laser-polarized alkali elements. The detection devices are the quadrupole mass spectrometer, QMS422, for stable nuclei, and a plastic scintillation detector and a high-purity Ge detector for unstable nuclei.

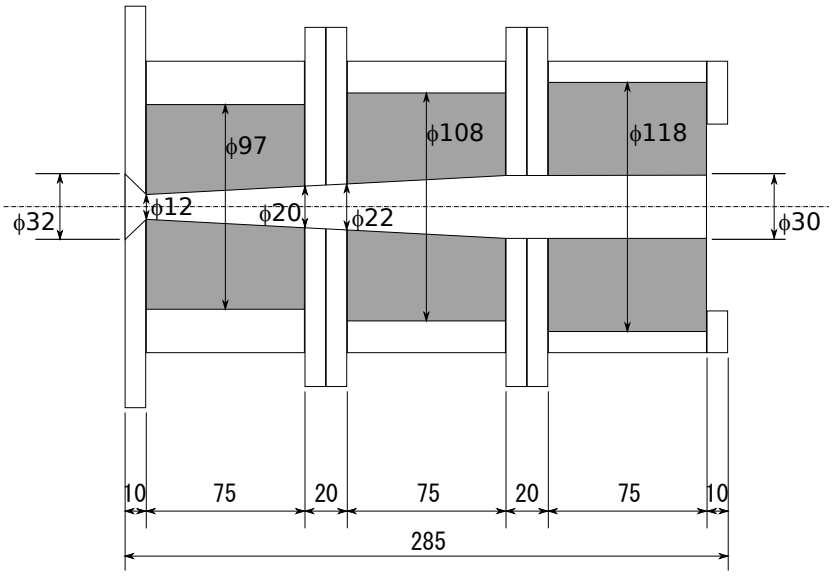

Fig. 4.6 Schematic view of the sextupole-magnet complex. The shadow parts are the ferromagnetic material, NEOMAX-44H, and the other parts are SUS316. The RI ions are transported from the left side to the right side.

Construction of "A" magnet

The sextupole magnet to converge the atomic beam is designed using the electromagnetic finite-element simulation code, OPERA [88]. The sextupole magnet constructed is shown in Figs. 4.6 and 4.7. To converge efficiently the atoms of which spins are parallel to the field a series of the three sextupole magnets is installed. Each of the sextupole magnets consists of 24 segments made of ferromagnetic material, NEOMAX-44H, that form the Halbach-type magnetic circuit to produce the strong magnetic field. The inner diameters of the first and second magnets are increased over regions from 12 to 20 mm and from 22 to 30 mm, respectively. The diameter of the final magnet is 30 mm. The magnetic fields at the pole tip are about 1.3 T. Each of the magnets is 7.5-cm long and they are arranged at intervals of 2 cm to exhaust the carrier gas.

Figure 4.8 shows the field strength of the sextupole magnets measured using a Hall probe. The measured magnetic field are in agreement with the model calculation using Eq. (4.2).

The focusing power of the sextupole magnet is simulated assuming that the mass and the drift velocity of RI are 20 mass unit and about 600 m/s, respectively. The result is shown in Fig. 4.9. When the entrance size of the RF cavity is set at 2 cm, the

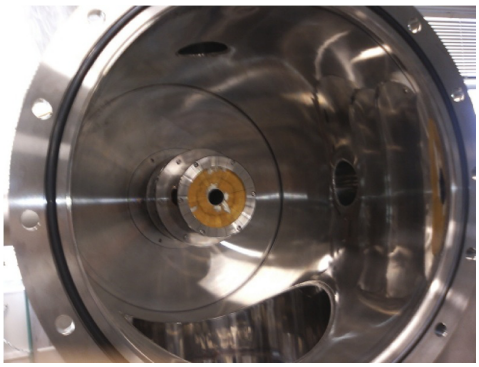

Fig. 4.7 Photo shows view of the sextupole magnets from the downstream side.

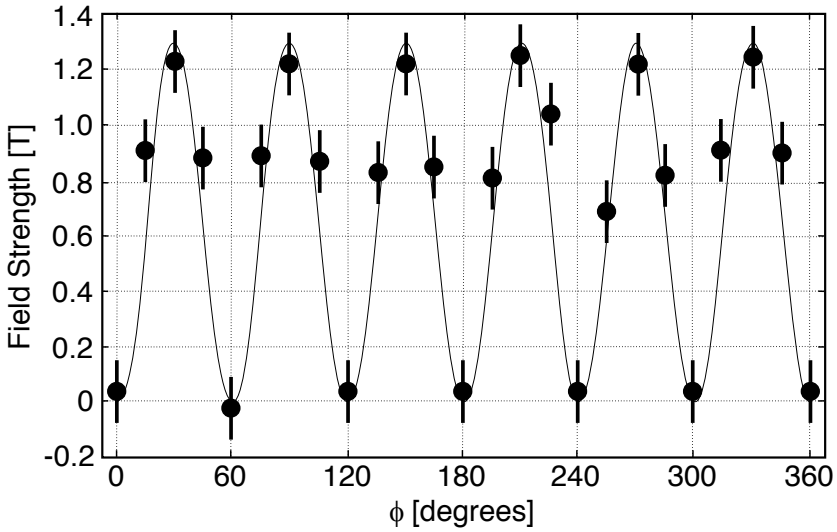

Fig. 4.8 Comparison of $B(\boldsymbol{r})$ field of the sextupole magnets between the measurement (dots) and the calculation using Eq. (4.2) (solid line). ϕ denote the azimuthal angle.

efficiency for RI to enter the RF cavity is improved by a factor of 1.8 with the magnet. This efficiency is good enough for our plan. If a lighter mass or a slower velocity is assumed, the focusing power becomes more efficient.

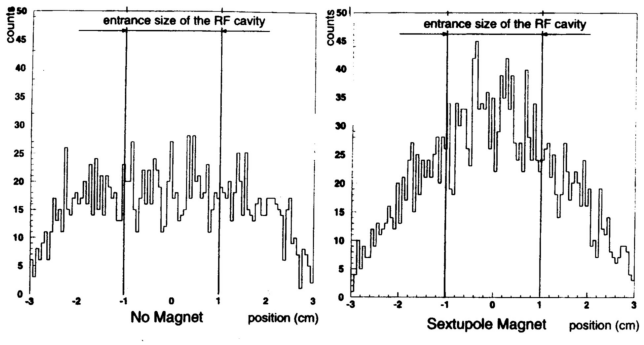

Fig. 4.9 Simulation result for distribution of transmitted RI at 10 cm behind the sextupole magnets. The left and right data are without and with the magnet, respectively.

4.3 Development of sources of RI atomic beams

The present section discusses principles and methods for some types of source of the neutral RI atomic beam, which is the most important part of the RIABR device. Once a sufficient source of neutral atomic beams of unstable nuclei becomes available, the succeeding Stern-Gerlach experiment using sextupole magnet would be performed. A neutral atomic beam is obtained by the processes in a series of steps of

1) stopping and thermalization of the energetic radioactive ions in a gas cell,
2) transport of the thermalized ions,
3) extraction of the ions from the cell through a nozzle, and
4) the neutralization of the ions.

In the followings, several developments conducted to obtain neutral atomic beam are presented.

4.3.1 Source of RI atomic beam with gas-flow extraction

RIs produced via the projectile-fragmentation reaction were stopped and thermalized in a small glass cell filled by an argon gas at 133 Pa. The temperature of the gas was kept as low as 150 K using a cryostat, in order to increase the stopping power of the gas volume and to reduce a velocity of the atomic beam. From our simulation, a velocity range of atomic beam below 400 m/s are favorable for the RIABR technique, and the condition is mainly determined by the vacuum-system performance and available magnetic field strengths in the sextupole magnet. The RI atoms are ejected from the cell together with the argon carrier gas into vacuum. The *Laval-type nozzle* [86] was mounted on the exit of the cell so that the gas molecules are spouted out to forward angles. A drawing of the setup is shown in Fig. 4.10.

The experiment was carried out using the RIKEN Projectile-fragment separator (RIPS) at the E6 beam line of the RIKEN Accelerator Research Facility. A ^{17}N beam was produced from fragmentation of ^{18}O projectiles at energy of $E/A = 100\,A$MeV on a 1.48-g/cm^2-thick ^{9}B target. In this experiment, we measured the counting rate of β-rays emitted from ^{17}N with a plastic-scintillation-detector telescope. The experiment was performed under two different conditions: β-rays were counted with or without an argon carrier gas flow. From the difference in the β-counting rates between the

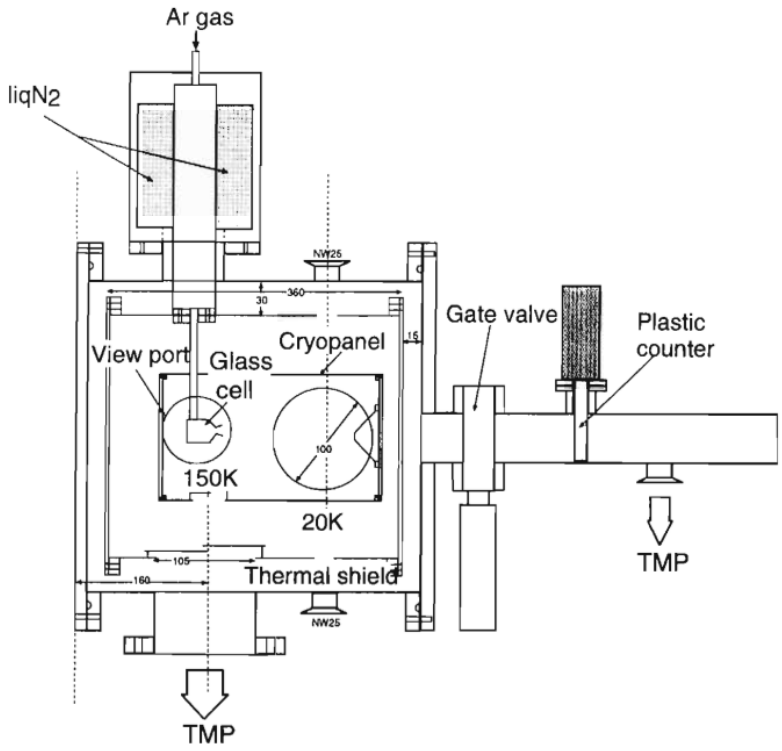

Fig. 4.10 Drawing of setup. The ^{17}N beam is incident at the cell from the direction perpendicular to the figure, and a fraction of atoms in the beam are stopped in a gas in the cell.

Table 4.2 Result of the experiment.

status	BaF_2 (counts)	Plastic (counts)	$R\left(=\frac{\text{Plastic}}{BaF_2}\right)$
Ar flow	15923159	19385	1.217×10^{-3}
no flow	13163251	15347	1.166×10^{-3}

two conditions, we ascertained ^{17}N atoms to be extracted from the cell by the carrier gas. The experimental result is shown in Table 4.2.

For normalization of the intensity of ^{17}N beam, a BaF_2 counter was placed far from the RIABR setup, which counted radiations such as γ-rays and neutrons originating from the beam. Table 4.2 shows a clear difference between the beam-normalized β-counting rates R with the gas flowing and non-flowing.

4.3.2 First prototype source of ion-guide scheme

We decide to introduce the ion-guide technique to the RI atomic beam source in order to increase the stopping power and to enlarge the gas volume. To produce slow RI atomic beam, the RI ions produced by the projectile-fragmentation reaction are stopped and thermalized in a volume filled with a high-pressure noble gas. In this volume, a strong static electric field are applied, so that the stopped RI ions are swiftly separated from the plasma region around the track of RI ions and are allowed to drift downstream. Close to the end of this volume, the field lines are compressed into an exit hole by increasing the field strength. The RI ions drift following the field lines and are thus compressed into the exit hole. In the region close to the exit hole, the noble gas flowing and converging by a cone placed upstream of the exit hole, so that the flow velocity rapidly increases and helps the RI ions to be extracted through the hole. As soon as the RI ions and the carrier noble gas enter the downstream volume, the RI ions are forced to proceed further downstream by a strong electric field, while the carrier gas is evacuated by a high-power vacuum pumping system. Finally, the RI ions are introduced to a neutralization section.

The first prototype source is shown in Fig. 4.11. It consists of a glass cell and ring electrodes outside it. The profile of the electric field applied to the ring electrodes is optimized to achieve maximum transportation efficiency. In order to obtain a strong focusing force at the exit hole, a one order of magnitude stronger field is applied there. The gas cell is filled with a helium gas of 27 kPa.

An experiment was performed using ^{17}N beam, produced by projectile-fragmentation reaction of ^{18}O beam at energy of $E/A = 100\,A$MeV on a 1.48-mg/cm^2-thick ^{9}Be target, and separated by the RIPS. To optimize the thickness of an aluminum degrader for ^{17}N, two thin plastic scintillators were introduced; one was installed upstream from the gas cell and the other was installed downstream. The thickness of the degrader was set so as the ratio of the upstream counting to the downstream one to be minimized. The energy of the beam incident at the apparatus was about 0.5 AMeV.

The transported RI ions were counted by two plastic scintillation counters, which detected β-rays. The transportation was checked by observing dependence of the field strength applied to the electrodes on the β counting rate. Unfortunately, no clear evidence of the transportation was obtained in this experiment. Speculative reasons

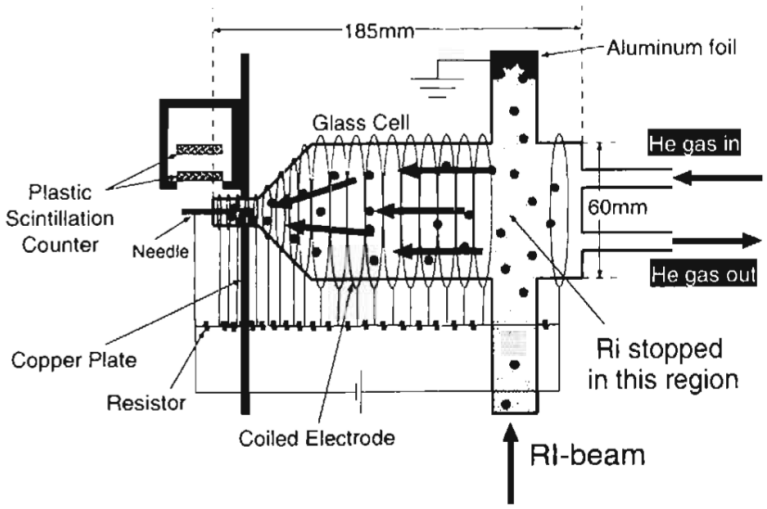

Fig. 4.11 Drawing of setup of first prototype.

are the neutralization of the ions due to gas impurity and the ion loss at the wall of the cell due to a low beam-stopping rate, a non-optimum electric field and charge-up of the glass cell.

4.3.3 Second prototype source of ion-guide scheme

In the case of the first cell, 1) there was no electrode on an inside wall of the glass cell, so that space charges originated from the deceleration of the RI ions remained on the inside wall and canceled the applied electric field. 2) an out-gases emitted from the cell caused the neutralization of the stopped RI ions, and 3) the gas flow, the volume size and the layout of the ring electrodes and the Laval-type nozzle had little flexibility because of dependence on a shape of the glass cell. In order to improve the second cell, the glass wall was rejected and electrodes were directly placed in the gas volume as shown in Fig. 4.12.

In a high-pressure gas volume filled by He at 40 kPa, first four electrodes were 1-mm-thick discs of 90 mm in diameter with respective inner openings of 70 mm in diameter, and an electric field between these electrodes was 10 V/cm. The remaining three electrodes had inner openings of 50, 20 and 10 mm in diameter, respectively. The last electrode had a hole at 0.2 mm in diameter, and the electric field was 2.5 kV/cm They were arranged with intervals of 9 mm. In a low-pressure gas volume there were eight disc electrodes at 36 mm in diameter with respective inner openings of 20 mm in diameter, and the electric field was 25 V/cm.

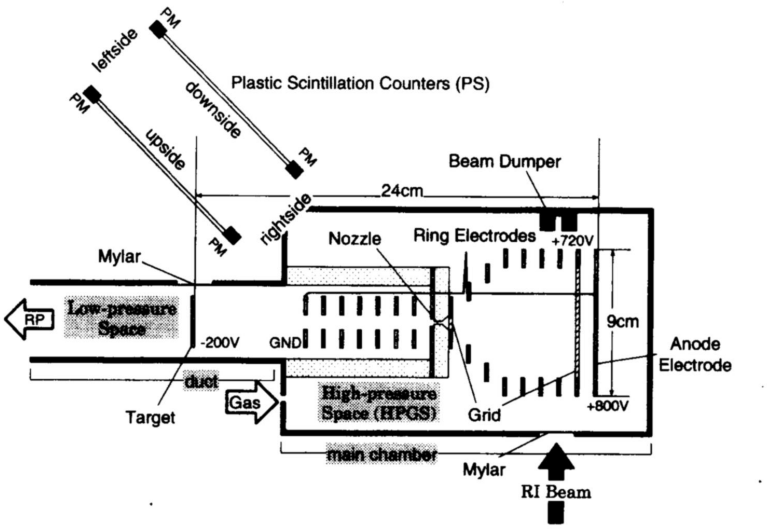

Fig. 4.12 Drawing of setup of second prototype.

An experiment was performed at the E6 beam line of the RIKEN Accelerator Research Facility. ^{12}B was produced by the projectile-fragment reaction of a 110-*A*MeV ^{22}Ne on a 740-mg/cm^2 ^{9}Be target, and separated by RIPS. The RI ions were stopped inside the high-pressure gas volume and extracted to the low-pressure volume through the nozzle of the exit hole by an electric field and a helium gas flow. The extracted RIs were collected at the catcher electrode. β-rays emitted from the catcher electrode were counted by the plastic scintillators. By observing the field-strength dependence on the β counts the extraction rate was estimated.

Unfortunately, no clear evidence of the extraction was obtained by the second prototype, too. It is assumed that the same reasons of the first prototype blocked even at the present second prototype.

4.3.4 Design of third prototype source of ion-guide scheme

The stopping volume of the third prototype RI atomic beam source of the ion-guide scheme was extended to 350 mm long in order to enhance the stopping power by five times from that of the second cell. The structure of the third cell is shown in Fig. 4.14. The first chamber for the RI-stopping and RI-drifting volume involved electrodes consisting of 36 stainless-steel discs and intervening ceramic spacers. The upstream 33 electrodes were 1-mm-thick discs of 58 mm in diameter with respective inner openings of 20 mm in diameter. The remaining three (34th, 35th and 36th) electrodes had

Fig. 4.13 Photo of electrode assembly of second prototype

inner openings of 15, 10 and 5 mm in diameter, respectively. A total length of the series of electrodes was 350 mm. The ceramic spacers located close to the nozzle had a tapered hole and formed the converging cone. This cone suppressed the discharge between electrodes, so that 2.1 kV could be applied to the last electrode. The orifice of the nozzle was as small as 0.5 mm in diameter in order to increase the pressure of the first chamber. The neon gas could be filled at 80 kPa. Approximately 70 % of the RI ions stopped in the volume, though they were energetically spread. The second chamber was a jet-separator (JS) chamber, which consisted of nine ring electrodes. The total voltage of −700 V was applied to these electrodes. The pressure could stay at 16 Pa which was 2×10^{-4} times as low as that in the first chamber.

Figure 4.15 shows a static electric field calculated with POISSON code [89] and the tracks of transport of incident ions simulated in a computer. In this simulation, the total voltages applied to the electrodes in the first chamber and in the second chamber were 2.4 kV and −700 V, respectively, and the charge of ions attached to the ceramic spacer was ignored. The electric field in the first chamber started with as low as 8 V/cm, and in the final electrode it rapidly increased to 2.3 kV/cm. As a result, the ions drifted and converged into the nozzle along the electrical flux line. For example, ions stopping at a radial distance of 10 mm from the axis of the cylindrical stopping gas volume converged at a radial distance of 0.6 mm just before the orifice. Around the orifice, since the velocity of the outgoing carrier flow was much larger than the ion drift velocity due to the electric field, the flow would bring the converging ions

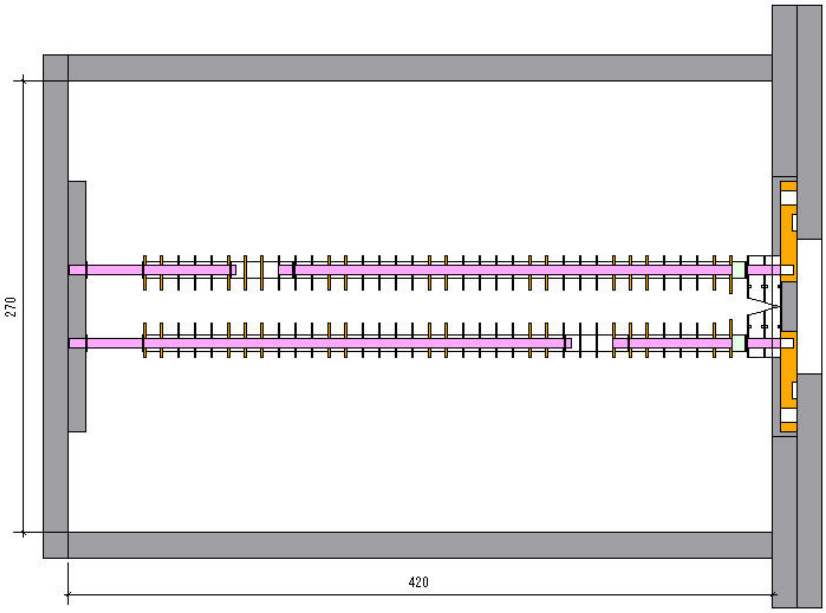

Fig. 4.14 Drawing of setup of third prototype.

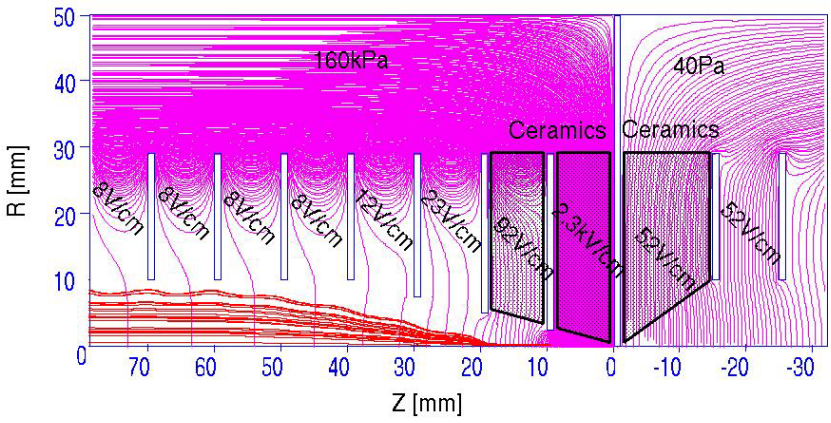

Fig. 4.15 Electric field and track of ions drifting near nozzle.

to the second chamber through the nozzle.

4.3.5 First online experiment with third prototype source

The first online test of the third prototype RI atomic beam source was performed using an ^{30}Al beam from RIPS. The experimental setup is shown in Fig. 4.16. The intensity of ^{30}Al introduced to the upstream RI stopping chamber was 3.7×10^4 pps, as counted at the beam monitor which was a 0.5-mm-thick plastic scintillator. The high voltage applied for the electrodes was 816 V and the orifice was 0.5 mm in diameter. Therefore, the electric field of the drift volume was 3.1 V/cm. The RI-stopping cham-

ber placed upstream was filled with an 80-kPa neon gas.

Measurement of drift efficiency

The plastic scintillator telescope was introduced to study the spatial distribution of the probability of ion loss during the drift in the gas chamber.

A chamber of the third source has a window of an aluminum plate of 1 mm in thickness. The telescope consisted of four layers of plastic scintillator. The first comprised 12 plastic scintillators of a $45 \times 200 \times 0.5\,\mathrm{mm}^3$ size each. The second layer comprised a plastic scintillator $800 \times 200 \times 5\,\mathrm{mm}^3$ in size. The third layer comprised 30 plastic scintillators of a $25 \times 200 \times 25\,\mathrm{mm}^3$ size each. The fourth layer was used as a veto counter and was a plastic scintillator of a $650 \times 380 \times 10\,\mathrm{mm}^3$ size. These layers placed at distances of 150, 410, 430 and 460 mm from the center line of the stopping volume. Assuming the β-rays emitted from the RI on the center line of the stopping volume, the telescope measured a distribution of the stopping position of the RI ion beam. A position resolution σ was 6 cm as measured using the β-ray, emitted from the ^{90}Sr/Y source placed in the center of the first chamber. A detection efficiency $\Omega\varepsilon$ was 0.01 from a simulation performed with GEANT code [48].

We first measured the ratio of counts at the telescope and the beam monitor while changing the thickness of aluminum degrader. The result is shown in Fig. 4.17. As inferred in this relationship, the thickness of the aluminum degrader was chosen to be 675 µm.

A drift efficiency was measured by a comparison between the distributions of ^{30}Al with and without the electric field. A result is shown in Fig. 4.18. The result and the intensity of ^{30}Al gave a drift efficiency of 0.0115(5).

Measurement of extraction efficiency

In the next step the measurement was made of the efficiency of ^{30}Al to reach the JS chamber through the nozzle.

The JS chamber was evacuated to 16 Pa. After passing through the orifice between these two chambers, ^{30}Al ions and the carrier gas formed jet and entered into volume of the second chamber. Nine electrodes were installed to guide ^{30}Al ions using a parallel electric field from the orifice to further downstream. The number of extracted ^{30}Al ions was evaluated by counting the β-rays using a cube-type plastic scintillator. It was a $100 \times 100 \times 110\,\mathrm{mm}^3$ cube with a hole of 70 mm in diameter and 80-mm-

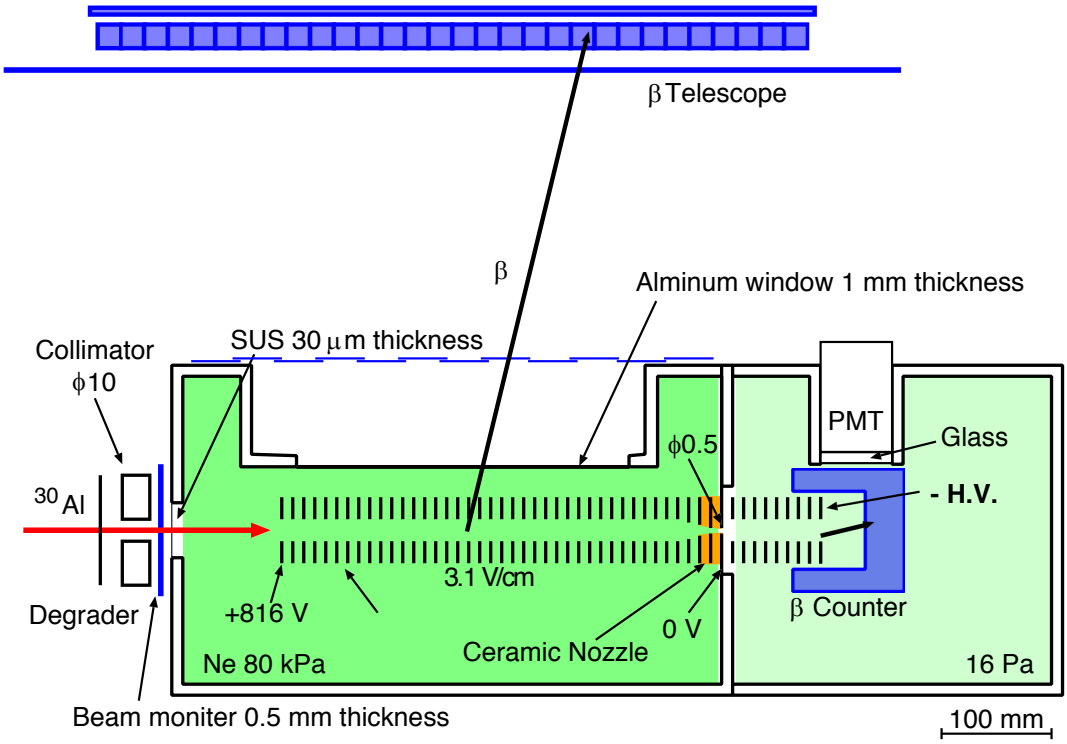

Fig. 4.16 Experimental setup for extraction efficiency measurement.

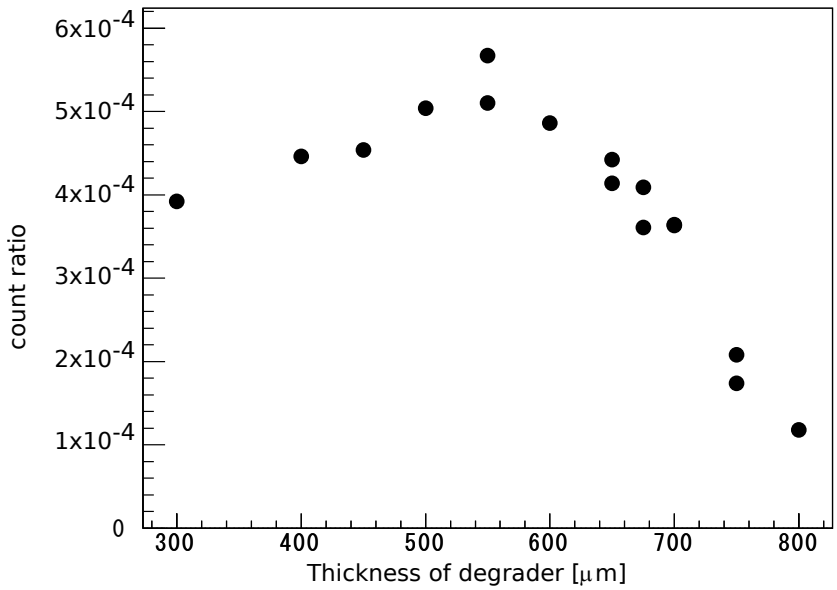

Fig. 4.17 Thickness of aluminum degrader vs. ratio of counts at telescope and that at beam monitor. Guided by this relation, the thickness of the aluminum degrader was chosen to be 675 um.

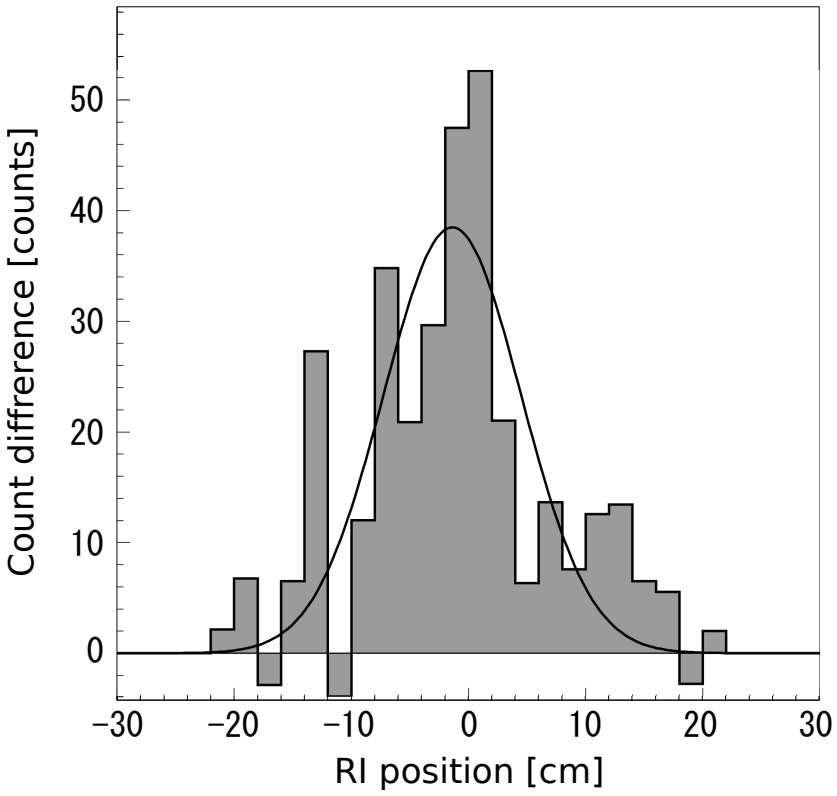

Fig. 4.18 Difference between yields of β-rays measured with and without electric field. The center of the first chamber is set to be zero. The drift efficiency obtained was 0.0115(5).

long cylinder, and placed in the JS chamber while a photomultiplier tube was placed outside the chamber over a glass flange. Although noise events such as from ions attached to the electrodes or nozzle were also counted, the amount of the noise events was small.

The extraction efficiency was the ratio of count at the cube scintillator to that at the beam monitor. Figure 4.19 shows the obtained extraction efficiency depending on the electric field strength. The maximum extraction efficiency was determined to be $4.3(1) \times 10^{-4}$.

4.3.6 Second online experiment with third prototype

In order to test the radioisotope ion collection, experiments were performed at CYclotron and RadioIsotope Center (CYRIC) of Tohoku University [90, 91]. The experimental setup consists of a reaction target (the deuterium enriched polyethylene), an argon-gas degrader, the ion-guide system and the β telescopes. A secondary

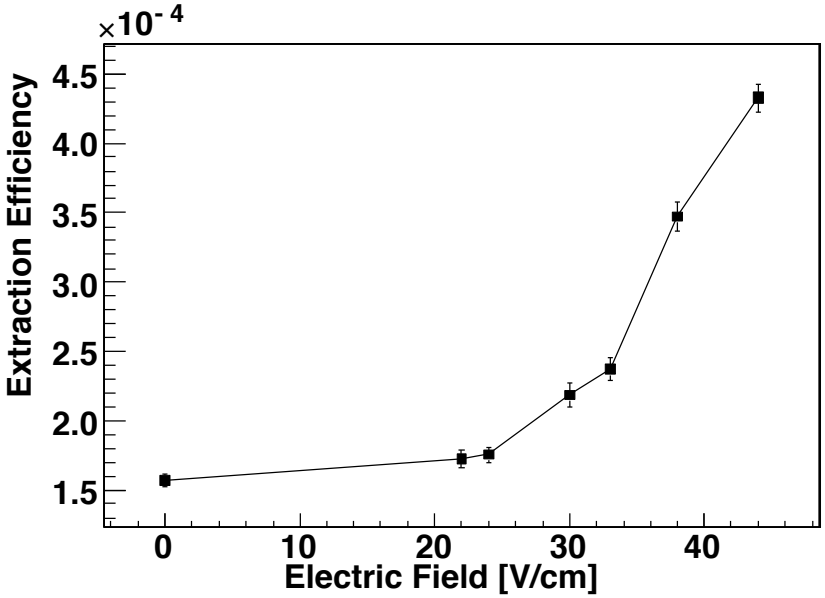

Fig. 4.19 Measured extraction efficiency. The electric field was limited to 44 V/cm because of discharge.

beam of unstable nucleus ^{16}N was produced by the d(^{15}N,^{16}N)p reaction at 150 MeV. Figure 4.20 shows a schematic view of the ^{16}N beam production and deceleration section. Two collimators with thin aluminum foil were installed downstream of the target to select the emission angle of ^{16}N. In order to prohibit the primary ^{15}N beam from entering the ion-guide system, the emission angles were selected in a range from 1.2 to 2.6°. Typical intensity of ^{16}N entering the ion-guide system was 10^4 particle per second (pps). A Faraday cup was installed between the collimators to stop the direct beam of ^{15}N for monitor the beam current. The Al_2O_3 plate was installed downstream from the Faraday cup for adjust the beam position. The energy of ^{16}N was degraded by the argon-gas degrader, and ^{16}N entered the ion-guide system. Effective length of the gas degrader was 512 mm and pressure of the gas degrader was adjusted so as to stop ^{16}N ions at the upstream half region of electrodes. Typical pressure of the gas degrader was about 17 kPa.

Figure 4.21 shows a prototype ion-guide system. The ion-guide system consists of two cells. The first cell is filled with neon gas at 27 kPa to stop ^{16}N ions, and the second cell is kept in vacuum using a turbo-molecular pump. Due to interactions with neon gas, a ^{16}N ion is neutralized and becomes inert thereafter against the action of the electric field. The neutralization/ionization efficiencies depend on the ionization energy, and stopping power of gases are proportional to square of the atomic num-

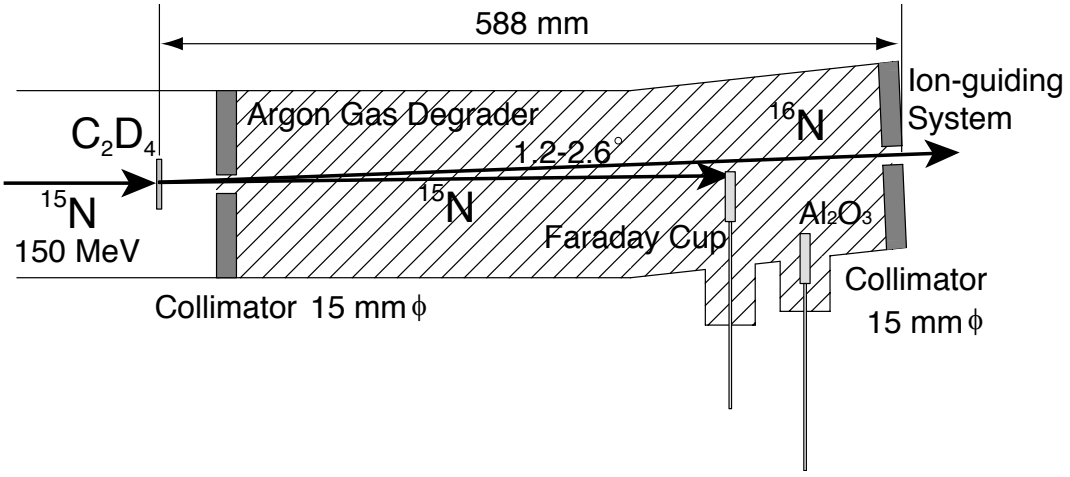

Fig. 4.20 Drawing of production and deceleration section which consists of reaction target (the deuterium enriched polyethylene), two collimators, argon gas degrader, Faraday cup, and Al_2O_3plate. ^{16}N was produced using d(^{15}N,^{16}N)p reaction at 150 MeV, and degraded by the argon gas and entered the ion-guide system.

ber (Z^2). Thus helium is the most suitable gas from the ionization, but is inadequate from point of view of the stopping power. In this study, we chose the second-period rare gas, neon, because the larger ionization loss facilitates the ions to stop in a small region. The neon buffer gas is worth studying, because there are few studies so far. Two cells were parted by an aluminum flange with 1-mm-diameter hole to extract ions with gas jet from the first cell to the second cell. An assembly of direct-current (DC) electrode was installed in the first cell. The electrode assembly consisted of 33 thin aluminum discs with 5 cm bore. The gap between the discs was 1 cm and the discs were connected by 300 kΩ resisters. The end electrode was connected to the flange by a 10 MΩ resister. By applying a high voltage (500 V) between the entrance of the electrode element and the flange, a DC electric field was generated to transport the ions downstream. Typical electric field was about 8 V/cm at the 300 kΩ region. A mobility of the ^{16}N ion was calculated as 120 cm/s [92], and typical transport time from the entrance element to the flange was 0.3 s. Since the half life of ^{16}N is 7.13 s, there was enough time to move the ^{16}N ions in these life time, whereas the neutralized ^{16}N atoms were intercepted on these way. By utilizing β-rays emitted from ^{16}N, distribution of the ^{16}N stopped in the first cell was measured using β telescope located besides the first cell. Typical position resolution of the β telescope was about 6 cm (1σ).

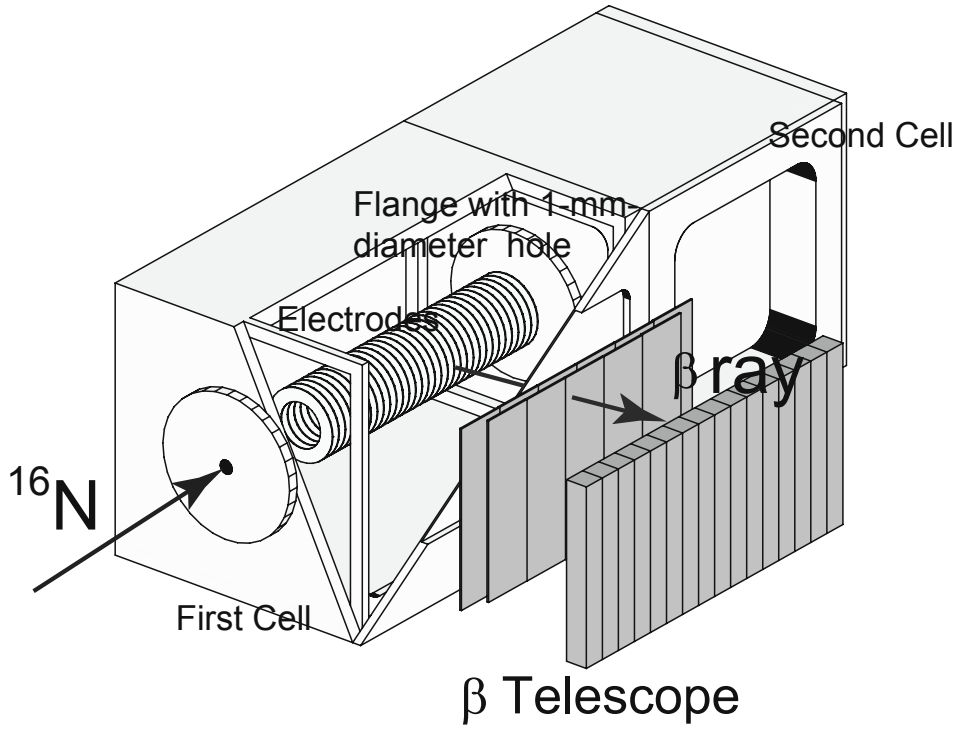

Fig. 4.21 Drawing of the proto type of ion-guide system. The ion-guide system consists of two cells: the first cell is aimed to stop and to transport ions using DC electric field. The ions were extracted through a 1-mm-diameter hole into the second vacuum cell. Position distribution of ^{16}N was measured by the β telescope located besides of the first cell.

By adapting the pressure of the gas degrader, the ^{16}N distribution adjusted to the upstream region of the first cell without the electric field. Then, by applying the electric field, the distribution shifted to the downstream region. By comparing the measurements with and without the electric field, transfer efficiency of the ^{16}N ions in the first cell was obtained. Figure 4.22 shows the position distribution differences of ^{16}N with and without the electric field, and a clear effect of the distribution shifted from upstream to downstream region by the electric field. The efficiency from the upstream region (1, 2, and 3) to the downstream region (4 and 5) was extracted as $3.20(28) \times 10^{-2}$.

Figure 4.23 shows another β telescope with gas-jet stopper installed in the second cell. The gas-jet stopper was made of aluminum plate to capture the ^{16}N ions. By measuring the β-rays from the ^{16}N ions, the transmission efficiency from the first cell to the second cell through the narrow hole can be estimated. From β-ray time spectrum shown in Fig. 4.24, β-rays emitted from ^{16}N was clearly observed. Taking into

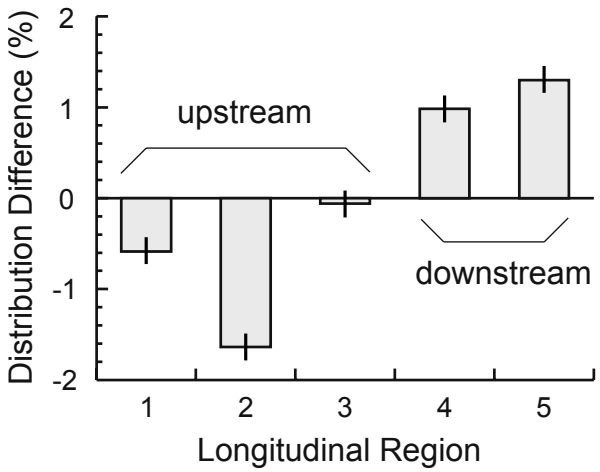

Fig. 4.22 Position distribution difference of ^{16}N with and without the electric field. An x-axis represents the longitudinal position dividing into five region. Each region covered about 6 cm length corresponding to the position resolution.

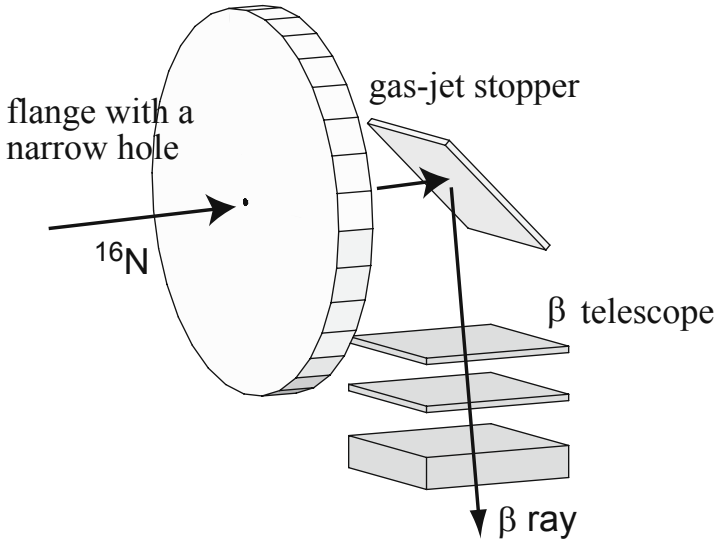

Fig. 4.23 Drawing of the gas-jet stopper and the β telescope installed in the second cell. The ^{16}N ions were captured by the stopper.

account geometrical acceptance of the telescope (~ 0.01), total transmission efficiency of the ion-guide system was extracted to be about 0.001.

In the present study, achieved transmission rate of ^{16}N was about 1 pps. This rate is not enough to apply the ABR method. We plan further developments such as improvement of the secondary ^{16}N rate, the application of high voltage of the DC electric field to reduce the neutralization rate. We also plan to install RF ion-guide system [1] to improve the transmission efficiency. With these developments we expect factor 100

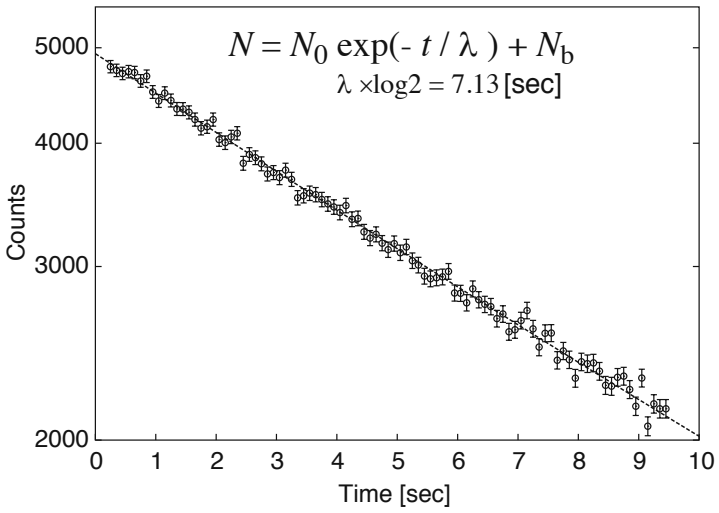

Fig. 4.24 β-ray time spectrum measured by the telescope. The spectrum is well reproduced by a decay function shown in the figure.

of improvement, then the ABR measurement will be performed.

4.3.7 Neutralization systems

Measurements of neutralization of ions were performed by using an ion source which was designed and installed for this experiment [93]. An off-line setup consisted of the ion source, ring electrodes, Faraday cups, a Laval-type glass nozzle, a neutralization system and the quadrupole mass spectrometer QMS422. A schematic view of the off-line setup is shown in Fig. 4.25. A static field formed by a series of ring electrodes was applied in the drift chamber in order to guide the ions towards the nozzle, and they were extracted into the active neutralization system through the nozzle.

Ions were produced by the arc discharge in the nitrogen gas flow and the nitrogen ions were extracted from the ion source into the ion drift chamber by an electric field together with gas flow. In the ion drift chamber, the ions were guided by an electric DC field and the gas flowed towards the nozzle. The total voltage applied to the series of the ring electrodes was 400 V. The pressure of nitrogen gas in the drift chamber was maintained at approximately 20 kPa, and the carrier-gas inlet was close. The current of ions was measured by the Faraday cup located just downstream from the ion source, and it was approximately 86.2 nA. At the end of the drift chamber, the current of ions was 10.0 nA. Thus the transmission efficiency obtained was 0.12 and lower than the previously reported on-line result, for the neutralization cross

section between the nitrogen atoms might be larger than that between the aluminum ion and neon atom. Other mechanisms such as the space charge effect are still to be investigated.

We checked an extraction efficiency from the drift chamber to the neutralization system through the nozzle with a diameter of 1 mm. In order to measure the current, another Faraday cup was installed at the distance of 10 mm from the nozzle exit instead of the neutralization system in Fig. 4.25. The current of extracted ions was 0.33 nA. From the results, the extraction efficiency was found to be 3.3×10^{-2}.

The neutralization system consisted of a yttrium tube, a stainless steel (SUS) tube and a SUS wire, as shown in Fig. 4.25. A DC bias of −200 V was applied to the yttrium and the SUS tube, so that ions were drifted to the yttrium tube by the electric field and converted into neutral atoms by neutralization in the charge-transfer collision with the yttrium tube. The neutral atoms after passing through the yttrium tube and the entrance hole with a diameter of 0.5 mm were detected by the QMS placed at the downstream chamber. If ions were not neutralized they could not reach the QMS, because the potential of the entrance flange was grounded.

In order to experimentally estimate the neutralization efficiency of this system, we measured the neutral atoms on the QMS under four kinds of conditions, in which the ion source was switched ON and OFF, and the yttrium tube was installed or removed (SUS tube only). The deduced neutralization efficiency is as following. A ratio (R) of the detected numbers of atoms with ion source on (N_{ON}) and off (N_{OFF}) is described as

$$\begin{aligned} R &= \frac{N_{\mathrm{ON}}}{N_{\mathrm{OFF}}} \\ &= \frac{[a_1 - a_2\alpha(1-\beta)(1-\gamma)(1-\varepsilon)]N_0}{a_1 N_0} \\ &= 1 - \frac{a_2}{a_1}\alpha(1-\beta)(1-\gamma)(1-\varepsilon), \end{aligned} \tag{4.3}$$

where N_0 is the number of atoms introduced into the ion source, α is an ionization efficiency in the ion source, β is a neutralization probability in the drift chamber, γ is an active neutralization efficiency in the neutralization system, ε is a neutralization probability in the downstream of the neutralization system, and a_1 and a_2 are total transmission efficiencies of the neutral particles and the ions, respectively.

In this experiment, a nitrogen gas was used as the ion source. An argon gas was employed as a carrier gas and the gas pressure in the chamber was approximately 10 kPa in Fig. 4.25. The neutral N_2 were measured with the ion source off for 120 s,

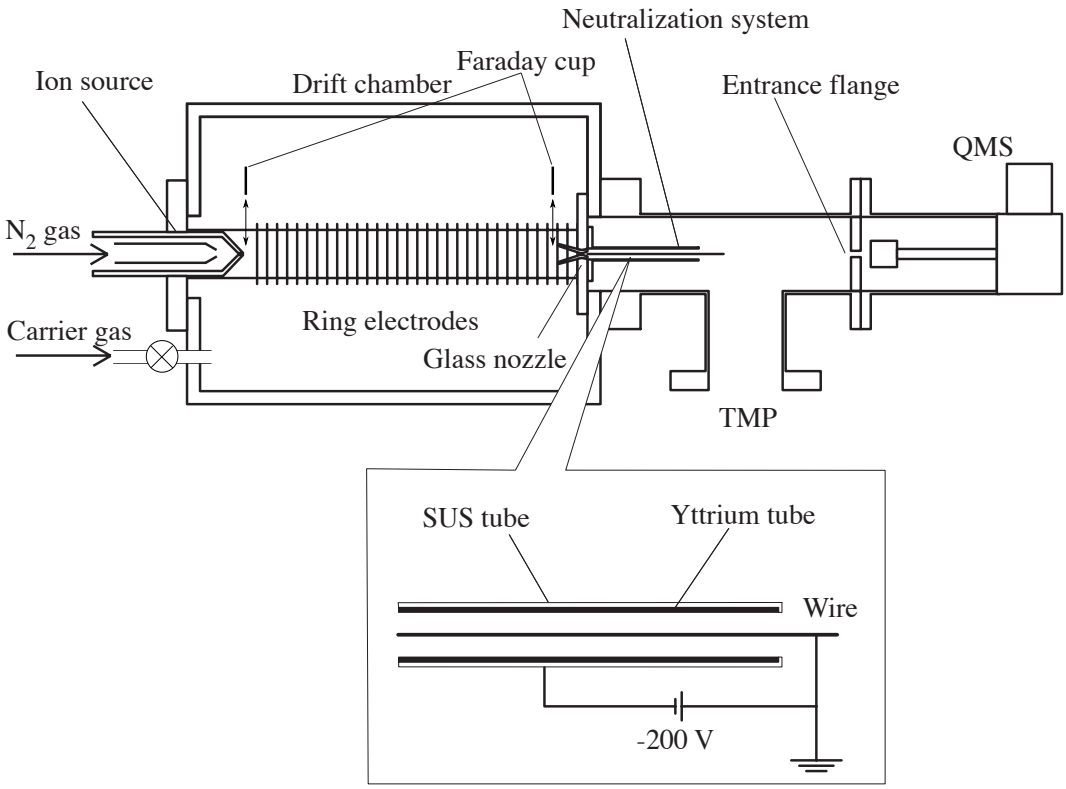

Fig. 4.25 Drawing of the off-line setup and the neutralization system. The length of the yttrium tube is 110 mm and the inner diameter is 8 mm.

and just after switching on the ion source, the same measurement was performed for 120 s, The set of these two measurements was repeated and the averaged counting rates with the ion source ON/OFF were compared in order to reduce the influence of the instability of the system's parameter α, gas-flow rate, etc. The above procedure was employed for yttrium tube and for SUS tube. A notable difference between ratios R with the yttrium tube and the SUS tube was observed as shown in Fig. 4.26. It would be considered due to a difference of γ, between the conditions with the yttrium and the SUS tube. In order to estimate γ of the yttrium, we are now evaluating $a_2 = a_1$ in each condition.

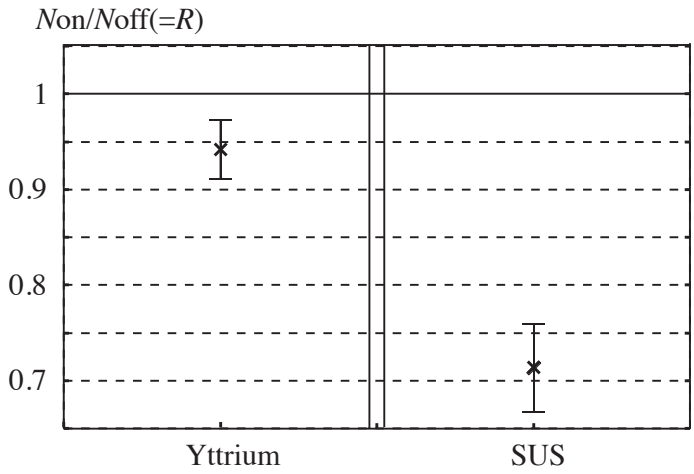

Fig. 4.26 Ratio "R" of count measured with ion source ON to that measured with ion source OFF. The "R" was determined both with and without a yttrium tube.

4.4 Conclusion

The RIABR is an extension of the Rabi resonance method and has an advantage over the β-NMR method because it does not require a spin-polarized RI. It provides a new and powerful method to measure nuclear moments of unstable nuclei, and also to produce thermal-energy spin-polarized beams which should be useful in surface physics and fundamental physics.

The RIABR device consists of an atomic beam source including a stopping cell and a neutralizer, a sextupole "A" magnet, an NMR section including an RF cavity and a "C" magnet, a quadrupole "B" magnet, and an RI detection device. The names "A", "B" and "C" come from the conventional atomic beam method. The neutral atomic beam is obtained by the processes of the stop of the energetic radioactive ions in the gas cell, the transport of the thermalized ions, the extraction of the ions from the gas cell through the nozzle and then the neutralization of the ions. Thus, the source of the thermalized and neutral atomic beam of unstable nuclei is the most important part of the RIABR device.

First, the small gas cell was designed and installed to test the stopping performance of the energetic unstable nuclei and the extraction efficiency through the small exit hole with the gas flow. It was filled by the argon gas at 133 Pa and kept as low as 150K. The unstable nucleus, ^{18}O selected using the RIPS were introduced into the gas cell, and extracted from the gas cell. Yields of β-rays emitted from the ^{18}O were measured. The result showed the clear difference between the yields for the gas flowing condition and the non-flowing one.

On the next step the volume of the cell was enlarged to increase the stopping performance of the gas cell, and ion-guide technique was introduced. The first and second prototype of RI atomic beam source with ion-guide technique were tested using RI beams selected by RIPS. However, we could not find out the extracted RI from the gas cell in these experiments. Speculative reasons would be the neutralization of the ions due to impurities of the gas and the ion loss at the wall of the cell due to low beam-stopping performance, a non-optimum electric field and charge-up of the glass cell.

Considering these reasons, the third prototype of RI atomic beam source with ion-guide technique was designed. The stopping volume of the third prototype was extended to 350 mm long that caused the stopping power become 5 times larger than

that of the second cell.

In order to measure the position of the stopped unstable nuclei in the third cell, the plastic scintillator detector telescope was installed. Since the present telescope could identify the direction of the β-ray emitted from the stopped unstable nuclei, it determined the position of the unstable nuclei stopped in the cell. Its position resolution σ and detection efficiency $\Omega\varepsilon$ were found to be 6 cm and 0.01, respectively.

The first online experiment was performed with the unstable nucleus ^{31}Al selected from the RIPS. This telescope system well worked to decide the position of the radioactive nuclei with the appropriate thickness of the Al degrader, and to measure the drift efficiency. The drift efficiency was measured by a comparison between the distributions of RIs with and without the electric field. The obtained drift efficiency was 0.0115(5). From the yield of the β-ray emitted from the RI extracted to the low-pressure volume, the maximum extraction efficiency was obtained as $4.3(1) \times 10^{-4}$.

The second online experiment was performed using the unstable nucleus ^{16}N produced by the d(^{15}N,^{16}N)p reaction at CYRIC. In this experiment the gas degrader was introduced at the upstream of the ion-guide system to reduce the energy of the recoiled nuclei. It show the better performances than that of the rotary metallic degrader because of easy gas-pressure control. The drift efficiency was measured in the same fashion of the first experiment and extracted as $3.20(28) \times 10^{-2}$. The total transmission efficiency of the ion-guide system was about 0.001.

Next step toward the RIABR was the development of the neutralization system. In this neutralization system the ions were converted into the neutral atoms by the charge-transfer collision with the yttrium. The neutralization efficiency of the system was measured using the nitrogen ion from the discharge-type ion source, which was installed at the ion-guide chamber filled by the argon gas. The nitrogen ions from the ion source were transported and extracted to the yttrium tube of the neutralization system. The yield of the neutralized nitrogen was measured using the quadrupole mass spectrometer. A notable difference between ratios with the yttrium tube and the SUS tube was observed. It would be considered due to the difference of neutralization efficiency between the conditions with the yttrium and the SUS tube.

The present results motivate further developments to realize the RIABR which nobody has ever done.

Chapter 5

Production of Spin-polarized ^{17}N Beam using Inverse-kinematics in Low-energy Transfer Reaction

5.1 Introduction

5.1.1 Physics with spin-polarized RI beam and β-NMR

Beams of spin-polarized Radioactive Isotope (RI) are applied for various studies, *e.g.* from in nuclear physics with β decays and nuclear moments [39], to in condensed matter physics including magnetism in metals and insulators, impurity and electronic dynamics in semiconductors, and superconductivity. In addition, the spin-polarized RI beam may even be an exclusive tool to investigate surfaces, layers and nano-sized structures, if distribution of energy and spatial of the beam at a measuring device can be controlled with sufficient precision. Production of the RI beam *via* inverse-kinematics reactions would be one of the most appropriate methods to obtain spin-polarized RI beams.

In the low-energy nucleon-transfer reaction, selection in both the recoil angle and the kinetic energy of the product nuclei brings the spin polarization to the RI beam, as shown in Fig. 5.1. In the inverse-kinematics arrangement, the distribution in the recoil angle in the normal kinematics shows up as a sharply focused angular dispersion of the RI beam. Yet, the narrow but finite widths of the angular and energy distribution of the RI beam preserve the memory of the recoil angle and energy. By selecting, consequently, a certain region of emission angles and energies of RI beam, the RI beam will be spin-polarized. Forward focusing beam facilitates more efficient transportation and focus at measuring point than the beam recoiled in normal kinematics, and also separation based on momentum analysis with an in-flight mass separator.

5.1.2 Application of spin-polarized RI to condensed matter physics: nitrogen-vacancy center

The exclusively long relaxation times achieved for nuclear spins in solid suggest a promising nuclear spin system for quantum bits (qubits). However, realization of the nuclear spin qubits requires inevitably the observation and operation of a single nuclear spin. Such an opportunity would be provided by a ^{15}N nuclear spin in a diamond nitrogen-vacancy center (N-V center). The N-V center consists of a nitrogen atom substituting for a carbon atom and a nearest-neighbor vacancy as illustrated in Fig. 5.2(a), and is produced in Type Ib diamond by high-energy electron irradiation and subsequent annealing. The N-V center has a ^3A ground state and a ^3E excited

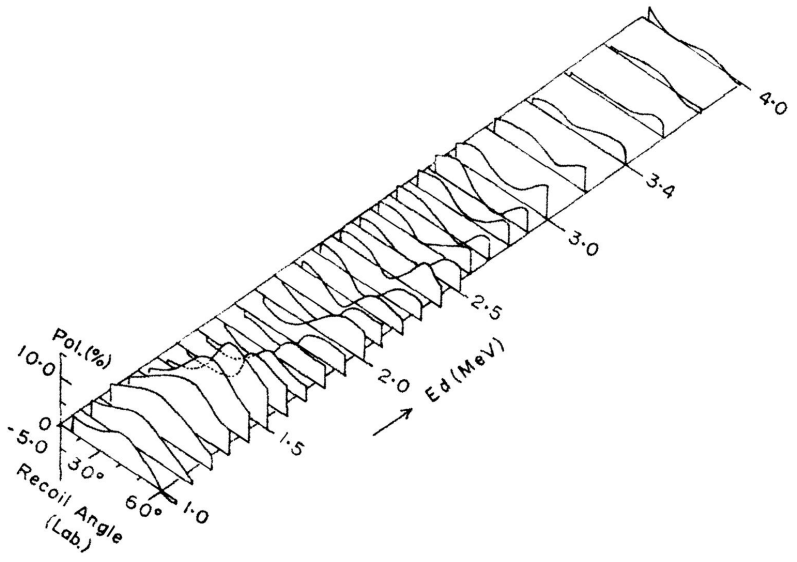

Fig. 5.1 Stereographical view of observed polarization of ^{12}B in ^{11}B(d,p)^{12}B reaction. (Tanaka *et. al.* [94])

state with a very short lifetime as shown in Fig. 5.2(b). The notably luminous optical transition between these states would provide a means of detecting a single nuclear spin in the N-V center: after repetition of the optical excitation and de-excitation, the electronic spin state is oriented preferentially to the population of the $m_s = 0$ state. Once the orientation of electronic spins is achieved, the application of a microwave for the Electron Spin Resonance (ESR) transition between the hyperfine-split levels leads to an intensity change in the optical transition. Thus it enables a high-sensitivity detection of ESR, namely optically detected ESR. Furthermore, incorporation of a Nuclear Magnetic Resonance (NMR) transition with the ESR induces the polarization of nitrogen nuclear spins. We will investigate the method of examining this nuclear polarization process by detecting β-rays from the unstable nuclei ^{17}N.

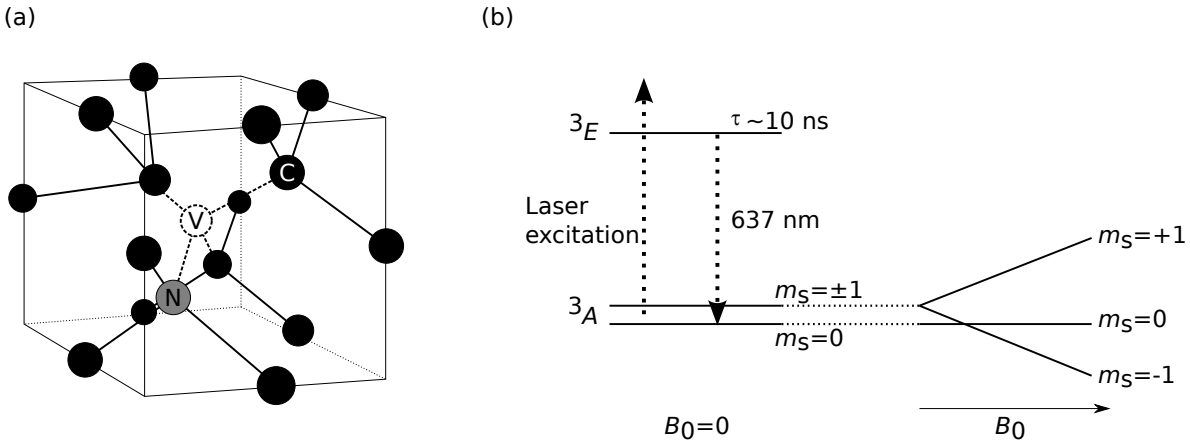

Fig. 5.2 Crystalline structure (a) and energy levels and excitation scheme (b) of N-V center.

5.2 Experimental Procedure

5.2.1 Production of spin-polarized ^{17}N beam

Spin polarization in inverse-kinematics reaction

As a starting point, it is appropriate to consider spin polarization in the normal-kinematics reaction. In the normal-kinematics experiment such as that with the ^{11}B(d,p)^{12}B reaction [94], Figure 5.1 suggests that the polarization obtained shows an abrupt change including its sign depending on the recoil angle and the energy of the deuteron. Additionally, it indicates that by selecting suitable recoil angles and incident deuteron energies the ^{12}B polarization should be obtained up to 15 %.

Meanwhile, Yamamoto and Kubo [95] discusses a possibility of large spin polarization for nuclei produced *via* an inverse-kinematics nucleon-transfer reaction using Brink's matching conditions [96, 97]. According to Brink, the kinematical matching condition for the large nucleon-transfer probability comprises two requirements: one is the linear momentum matching of the transferred nucleon and the other is the angular momentum matching which claims that the orbital angular momentum of the reaction system have to be approximately conserved. The first is given by

$$\Delta k = k_0 - \frac{m_1}{R_1} - \frac{m_2}{R_2} \approx 0, \tag{5.1}$$

where k_0 is a wave number of the projectile per nucleon in the laboratory system, R_1 and R_2 are the radii of the projectile and the residual nucleus, respectively, and m_1 and m_2 are the z-components of the orbital angular momenta l_1 and l_2 of the projectile and the residual nucleus, respectively. Here the z axis is chosen parallel to a vector $\boldsymbol{k}_f \times \boldsymbol{k}_i$ where $\boldsymbol{k}_i$ and $\boldsymbol{k}_f$ are the incoming and outgoing wave vectors, respectively, as illustrated in Fig. 5.3. The second requirement is written as

$$\Delta L = (m_2 - m_1) + \frac{1}{2}k_0(R_1 - R_2) + \frac{Q_{\text{eff}}R}{\hbar v} \approx 0, \tag{5.2}$$

where $R = R_1 + R_2$ and v is the relative velocity of the projectile and the residual nuclei. Q_{eff} denotes the effective reaction Q value defined as $Q_{\text{eff}} = Q - \Delta V_{\text{C}}$ with ΔV_{C} being the difference in the Coulomb barrier between the initial and final channels. In addition, Brink defines the following third condition due to the parity restriction,

$$l_1 + m_1 : \text{even} \quad \text{and} \quad l_2 + m_2 : \text{even}. \tag{5.3}$$

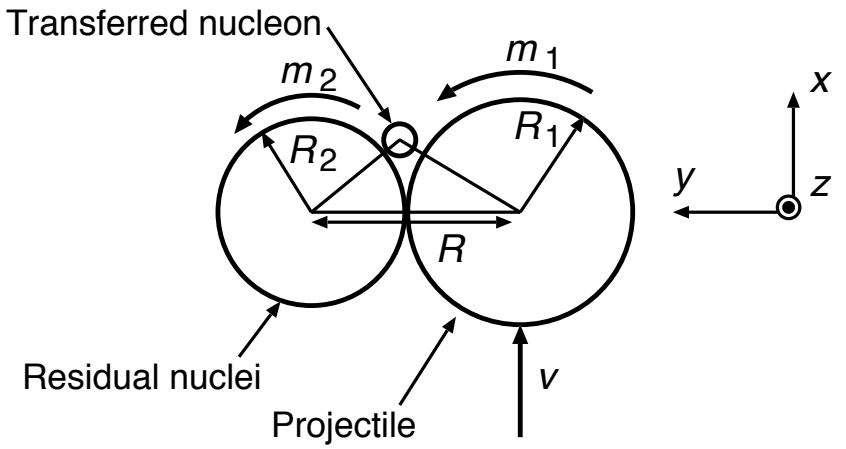

Fig. 5.3 Diagram of transfer process. Symbols are defined in the text.

They show that the cross section acquires a strong dependence on the z-component of nucleon orbital angular momenta before and after the transfer.

The sign of polarization should depend on whether the reaction is near-side or far-side dominant [95]. The deflection angle of the ejectile is essentially governed by a balance between the attractive nuclear force and the repulsive Coulomb force. The nuclear force should become dominant as the proton number of the target decreases, so that the dominating trajectory is considered to switch from the near-side to far-side trajectories [98]. The kinematical matching conditions become different between the near-side and far-side trajectories, and consequently, their cross sections can be very different. Therefore the large spin polarization will realized by choosing the kinematics conditions experimentally, where the Brink's matching condition is satisfied and either of the near-side or far-side trajectory is dominant.

Isotope separation

The present experiments were performed using a low-energy in-flight separator CRIB [99]. CRIB essentially consists of two dipole magnets and seven quadrupole magnets, as shown in Fig. 5.4.

The isotope separation was provided through the analysis of the magnetic rigidity in the dipole. The magnetic rigidity is defined as

$$B\rho = \frac{m_{\mathrm{N}} v_0}{e} \frac{A}{Q}, \tag{5.4}$$

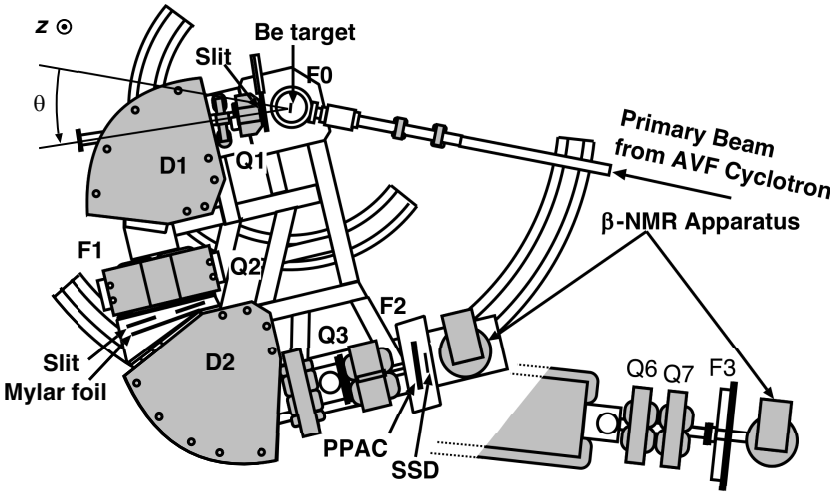

Fig. 5.4 Schematic view of the low-energy in-flight isotope separator CRIB and the β-NMR apparatus.

where B is the magnetic field, ρ is the gyroradius of the particle due to this field*1, m_{N} is the nucleon mass, and e is the elementary electric charge. A and Q denote the mass and charge of the particle, respectively. The velocity v_0 is almost the same as the projectile one. Therefore, by placing a slit at the momentum-dispersive focal plane F1 the fragments are selected according to their A/Q values through the first dipole D1.

Production of ^{17}N beam

A beam of ^{17}N was produced via the Be(^{18}O,^{17}N) reaction. A primary beam of $^{18}O^{7+}$ at energy of 7.0 AMeV with intensity of 300 pnA bombarded a thin Be target of 2.8 mg/cm^2, which was installed in a target chamber at F0. The ^{17}N products were separated from other species by the magnetic rigidity analysis. In order to reduce intensity of $^{17}O^{7+}$ from that of the secondary beam, the charge stripper foil of 1.5-μm Mayler was inserted in the path of the secondary beam at the momentum-dispersive focal plane F1. The yield of the ^{17}N beam was typically 10^5 cps at the achromatic focus F2 by selecting the emission angle in the laboratory system from −0.6 to −2.8° and the momentum from 1.84 to 1.88 GeV/c.

*1 The radii ρ in the D1 and the second dipole D2 in the CRIB are both 0.9 m.

5.2.2 Detection of nuclear magnetic resonance

β-detected nuclear magnetic resonance by means of adiabatic fast passage method

The Adiabatic Fast Passage (AFP) technique of NMR [100] was employed to measure the spin polarization P of ^{17}N ($I^{\pi} = 1/2^{-}$, $\mu = 0.352(2)\ \mu_{\rm N}$, $T_{1/2} = 4.173\,$s). Angular distribution of β rays originating from the spin-polarized nuclei with P is given by

$$W(\theta) = 1 + \frac{v}{c} A_{\beta} P \cos\theta, \tag{5.5}$$

where θ denotes the angle of β-ray emission relative to the z-axis, v and c are the velocity of the β-particle and light, respectively, and A_{β} is the β-decay asymmetry parameter. A_{β} is determined by spins of levels for pure Gamow-Teller transitions and +0.57 for the β decay of ^{17}N. The ratio between the measured β-ray counts at the up and down telescopes is denoted by R. Effect of β-NMR is evaluated from R measured with the NMR "ON" and "OFF" related to the polarization P of ^{17}N, as

$$\frac{R_{\rm ON}}{R_{\rm OFF}} = \frac{(1 - A_{\beta}P)/(1 + A_{\beta}P)}{(1 + A_{\beta}P)/(1 - A_{\beta}P)} \approx 1 - 4A_{\beta}P. \tag{5.6}$$

β-NMR apparatus

The β-NMR apparatus consisted of a stopper, an NMR magnet, RF coils, and β-ray counters. A schematic view and a photo were shown in Figs. 5.5 and 5.6, respectively.

■Stopper The stopper was a cubic MgO single crystal because of a sufficiently long spin-lattice relaxation time T_1 for ^{17}N at the room temperature [101]. The MgO stopper was placed in a center of the magnet pole and, additionally, in a vacuumed duct, because energy of the ^{17}N beam, ~6.4 AMeV was too low to pass through the air. The size of the MgO crystal was $16 \times 22 \times 1\,$mm^3 and the 16x22 plane was the (110) plane. The MgO stopper was inclined at 45° to the magnetic field.

The duct was made of an 1-mm-thick Fiber Reinforced Plastic (FRP) and its outer size is $20 \times 20\,$mm^2.

■NMR magnet The NMR magnet provided the static magnetic field B_0 to the stopper in order to preserve the spin polarization and to define the NMR frequency. The magnet was located on the F3, or the F2 stage of the CRIB in order to keep with the

rotation of the CRIB. A gap of the magnet pole was 40 mm and a magnetic field was 707.7 mT.

■RF coils The RF coils applying the oscillating magnetic field B_1 to the stopper in the direction perpendicular to B_0, were mounted just by the side of the stopper and outside of the duct. The size of the RF coils was 20 mm in diameter. The RF coils provided the B1 field of 0.2 mT containing 3.8 MHz ± 0.1 %.

■β-ray counters The β-ray counters of the β-NMR was specified for the detection of the emission direction of the β-ray, up or down, its number, and the large detection efficiency. The β-ray counters were two telescopes consisting of three plastic scintillators (BICRON BC408) located above and below the stopper. The thickness of each scintillator was designed to be 1 mm. The radii of the nearest, middle, and farthest scintillators from the stopper were 100, 110 and 120 mm in diameter, respectively. The β-ray telescopes spanned ~50 % of the 4π solid angle in total. This detector solid angle provided an optimized figure of merit, given as $A_{\mathrm{eff}}{}^2\Omega_\beta$ in terms of the angle-averaged β asymmetry A_{eff} and the β detection solid angle Ω_β, for the measurement of β-ray asymmetry. Each scintillator was wrapped the aluminized mylar film and then the light shielding sheet due to isolation of the scintillation. The β-ray detection required coincidence in signals from the three thin plastic scintillators in order to reduce the background noise. Main component of the background noise was γ activities from the daughter nuclei. Cosmic rays were reduced by a iron yoke of the magnet and neutrons from the reaction target were rejected by the time sequence. Efficiency for γ-ray detection by the thin scintillator was smaller than that for β-ray one. In addition, the coincidence in the three signals rejected events of the electrons produced by the Compton scattering, the photoelectric effect, and the pair production. The energy distribution of the β-ray prevent measurement of the energy from identifying its origin, in contrast to that of the γ-ray. Thus, the β-NMR requires composition ratio of the beam implanted in the stopper.

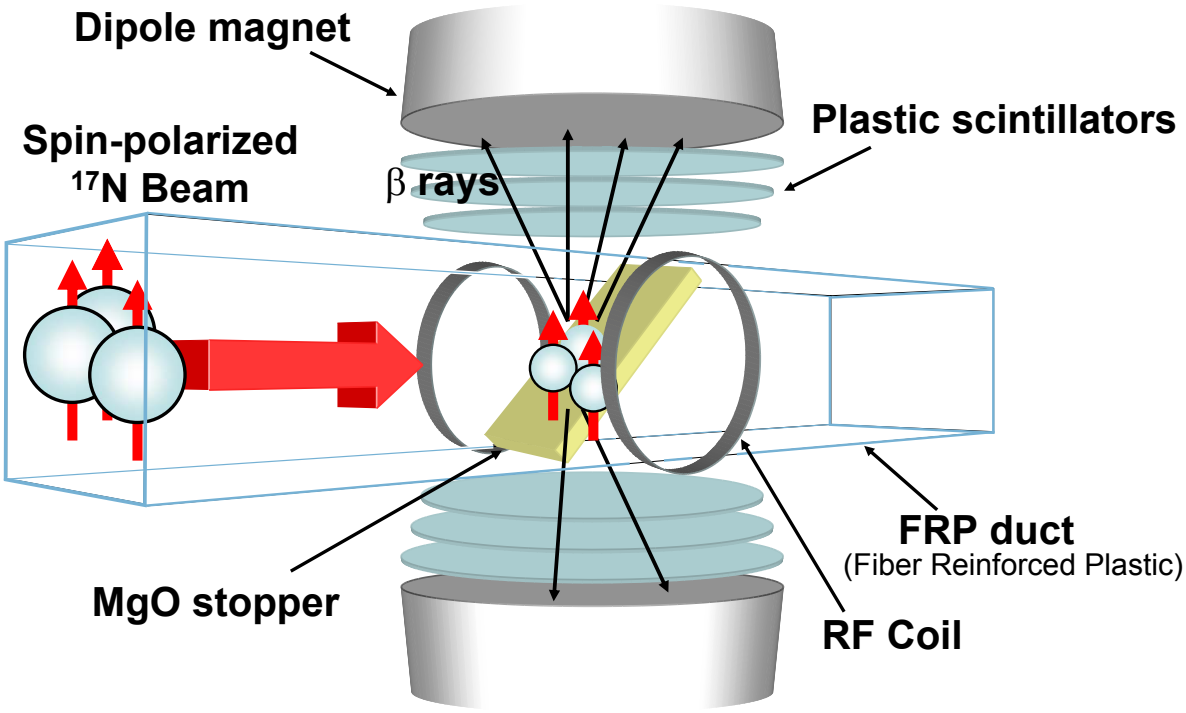

Fig. 5.5 Schematic view of β-NMR apparatus

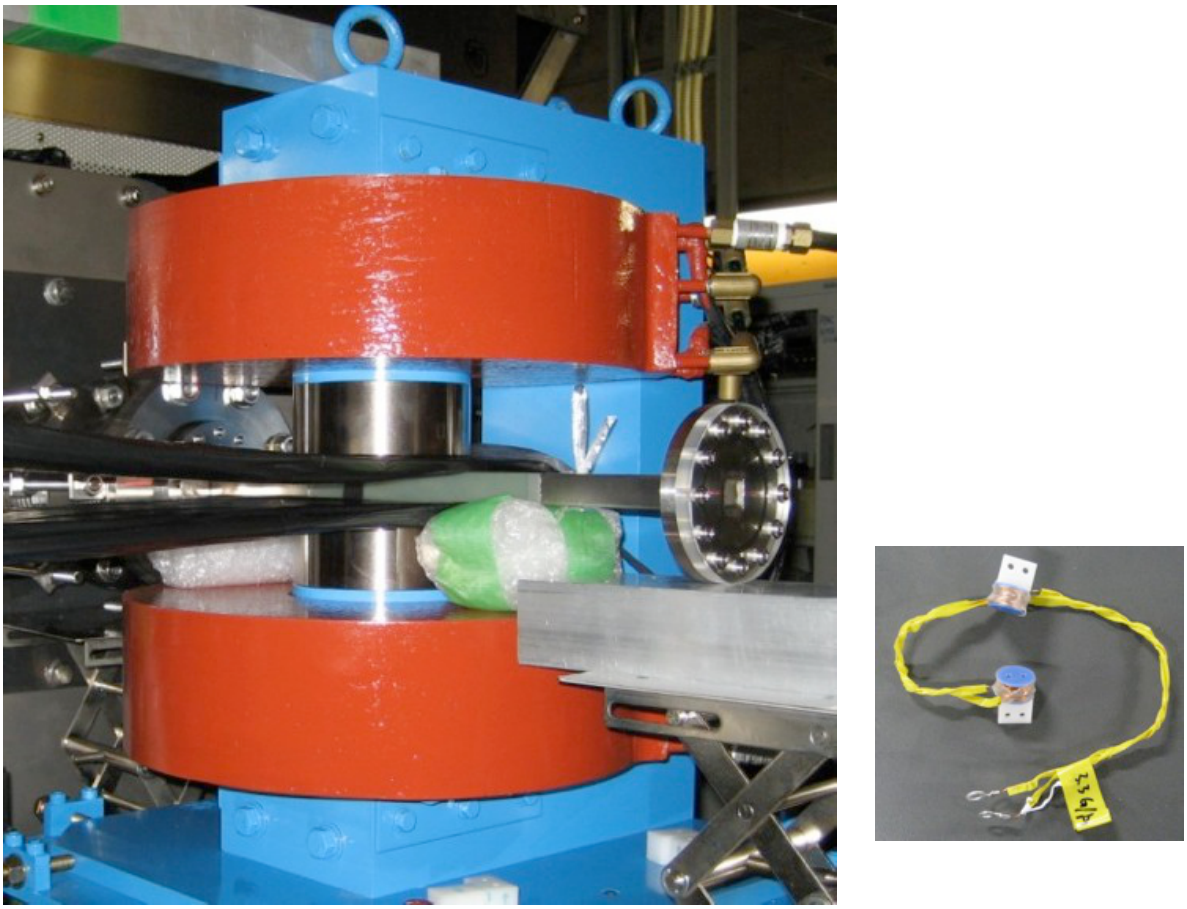

Fig. 5.6 Photo of β-NMRapparatus

5.3 Data analysis

5.3.1 Properties of ^{17}N beam

Yield and purity of secondary beam

ΔE-TOF spectrum at achromatic focal plane F2 is presented in Fig. 5.7. A composition ratio of $^{17}N^{7+}$ was 12 %, And contaminations were $^{18}O^{7+}$ (15 %), $^{15}C^{6+}$ (4 %), $^{14}C^{6+}$ (32 %) and p (26 %). A total yield was 10^6 pps, therefore the yield of ^{17}N was 10^5 particle per second (pps). An energy of ^{17}N was 6.24 to 6.52 AMeV.

Yield and purity of β-rays from RI implanted in MgO stopper

A time spectrum for the β-ray events accumulated is shown in Fig. 5.8. Least squares fitting to the time spectra of a theoretical function is represented two-component experimental decay and a constant background, for short-life β emitters of the beam are ^{17}N ($T_{1/2}$ = 4.173 s) and ^{15}C ($T_{1/2}$ = 2.449 s), It indicates that fractions of the β-rays originating from ^{17}N and ^{15}C were 79 % and 17 %, respectively. Total β-ray yield is

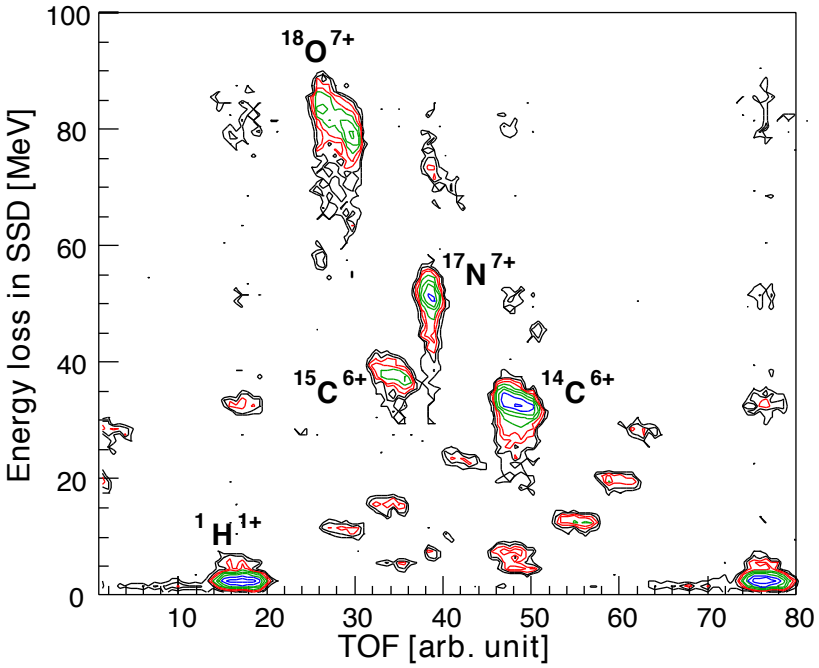

Fig. 5.7 ΔE-TOF at achromatic focal plane F2. The vertical and horizontal axes stands for the energy loss in the silicon state detector, ΔE and the Time Of Flight (TOF), respectively.

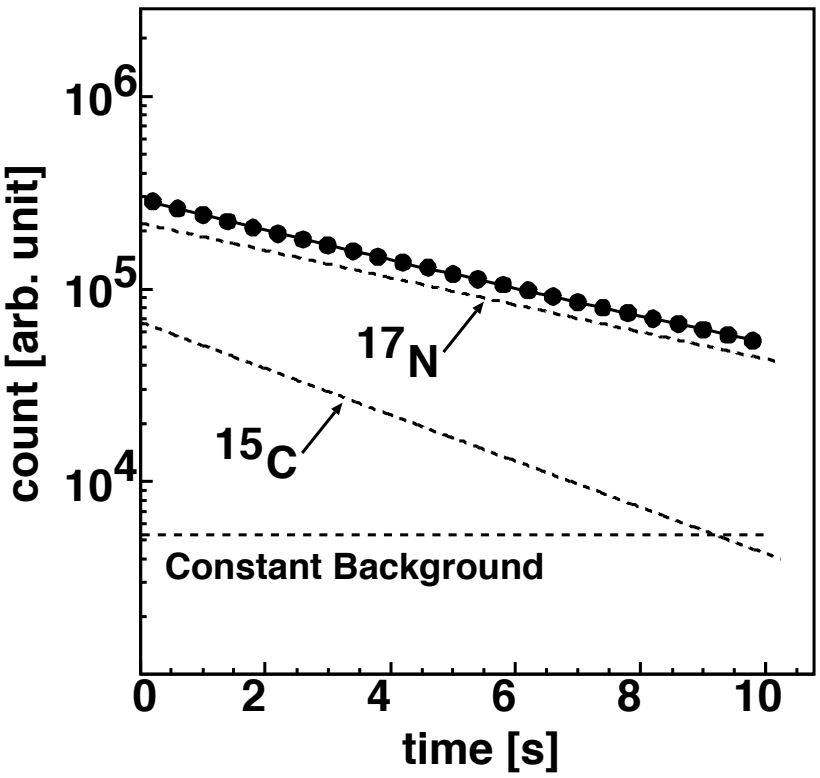

Fig. 5.8 β rays counts as a function of the time (dots). The solid line represents a fit to the data using two exponentials plus a constant background. These individual components are for ^{17}N ($T_{1/2}$ = 4.173 s), ^{15}C ($T_{1/2}$ = 2.449 s) and the constant background, are shown by the dashed lines.

300 count per second (cps).

5.3.2 Polarization of ^{17}N beam

Momentum distribution and polarization of ^{17}N beam

Momentum distribution of an outgoing momentum p of the ^{17}N beam is shown in the upper part of Fig. 5.9, where the emission acceptance is chosen to be −0.6 to −2.8° in the laboratory system corresponding to −2 to −10° in the center-of-mass system. Shape nicely fits to the Gaussian and standard deviation is 0.016 GeV/c. Observed β-ray asymmetry $A_\beta P$ obtained for ^{17}N is shown as a function of p in the lower part of Fig. 5.9. The momentum acceptance had to be set to a right region of a peak of the distribution due to the polarization of the beam.

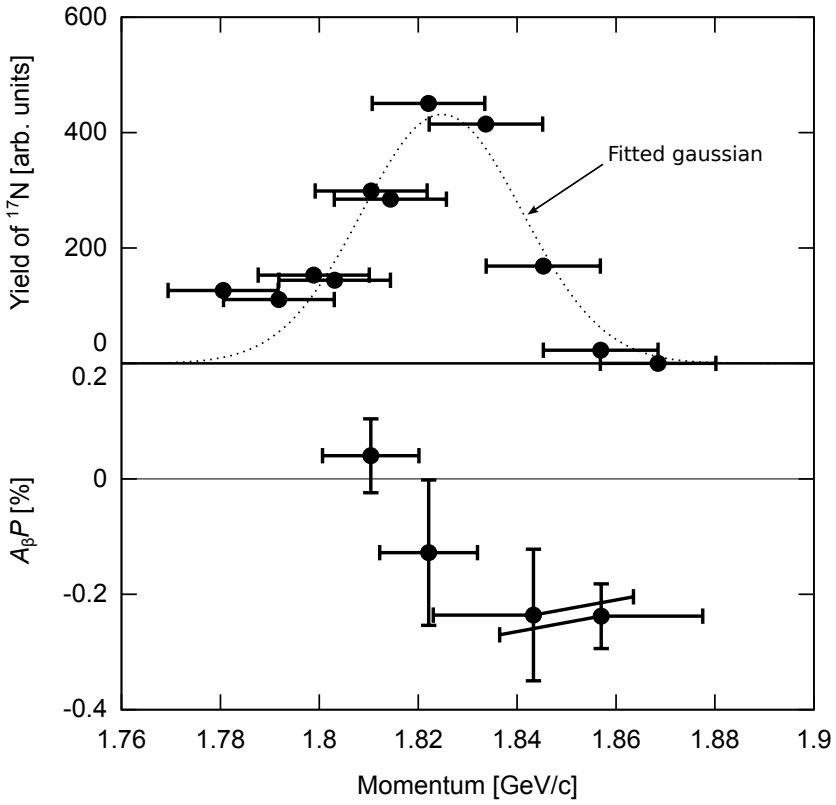

Fig. 5.9 (a) Momentum distribution of ^{17}N and (b) Observed β-ray asymmetry $A_\beta P$ as a function of the momentum of the ^{17}N beam at the emission angles $\theta_{\mathrm{c.m.}}$ = −2 to −10°. Horizontal and vertical extension indicate momentum acceptance and statistical uncertainty in $A_\beta P$ (one standard deviation), respectively.

Emission angle and polarization of ^{17}N beam

Observed β-ray asymmetry $A_\beta P$ as a function of the emission angle in the center-of-mass system $\theta_{\mathrm{c.m.}}$ is shown in Fig. 5.9. In this measurement the momentum was confined to (1.000–1.025)p_0 where p_0 was a peak in the momentum distribution of the beam. Maximum $|A_\beta P|$ is 0.39 %, thus $|P|$ is 0.68 %. However, considering uncertainties, the polarization does not depend on the emission angle, and $|A_\beta P|$ is approximately 0.2 % in spite of the emission angle. $|P| \sim 0.4$ % looks like rather small.

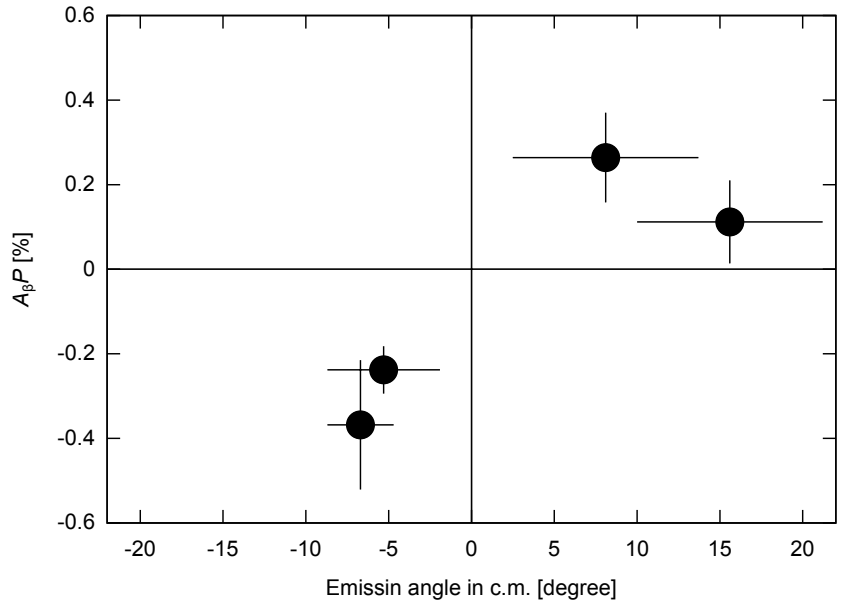

Fig. 5.10 Observed β-ray asymmetry $A_\beta P$ as a function of the emission angle in the center-of-mass system, $\theta_{\text{c.m.}}$. Horizontal extension indicates the acceptance of the emission angle. Vertical extension indicates the uncertainty in $A_\beta P$ (one standard deviation), which was mainly due to the counting statistics.

5.4 Discussion

5.4.1 Matching condition of ^{9}Be(^{18}O,^{17}N)^{10}B reaction

We evaluated values of $|\Delta k|$ and $|\Delta L|$ numerically as a function of the incident energy E_{i} of the ^{18}O beam as stated by Eqs. (5.1) and (5.2), and the result is shown in Fig. 5.10. In the simplest case of the ^{9}Be(^{18}O,^{17}N)^{10}B reaction with a ground state (g.s.) to g.s. transfer of proton, the proton is transferred from a $\mathrm{p}_{1/2}$ state to a $\mathrm{p}_{3/2}$ state, so that both l_1 and l_2 are 1. From Eq. (5.3) we obtain $m_1 = \pm 1$ and $m_2 = \pm 1$, which we used in the evaluation.

As seen in Fig. 5.11, at $E_{\mathrm{i}} = 126\,\mathrm{MeV}$ the condition on Δk (Eq. (5.1)) is mostly satisfied for the transfer from the $m_1 = +1$ to $m_2 = +1$ states (a). On the other hand, the condition on ΔL (Eq. (5.2)) are satisfied for the transfers from -1 to $+1$ (c). The sign of m_1 plays an important role in a sign of the polarization of the ejectile due to the angular-momentum conservation. Thus, the transfers with $m_1 = +1$ contribute to negative polarization of ^{17}N, while $m_1 = -1$ to the positive. The sign of the polarization P observed for $\theta_{\mathrm{c.m.}} > 0$ is negative, since $A_\beta P > 0$ in Fig. 5.10 whereas $A_\beta < 0$ for the β decay of the ^{17}N. This indicates that the transfer from +1 to +1 (a) should be dominant.

The $|\Delta L|$ value for the transfer from +1 to +1 (a) becomes smaller than that for the transfer from -1 to +1 (c) for $E_{\mathrm{i}} \geq 140\,\mathrm{MeV}$. Thus, the magnitude of the polarization of ^{17}N is expected to rise as E_{i} increases beyond 140 MeV (7.8 AMeV).

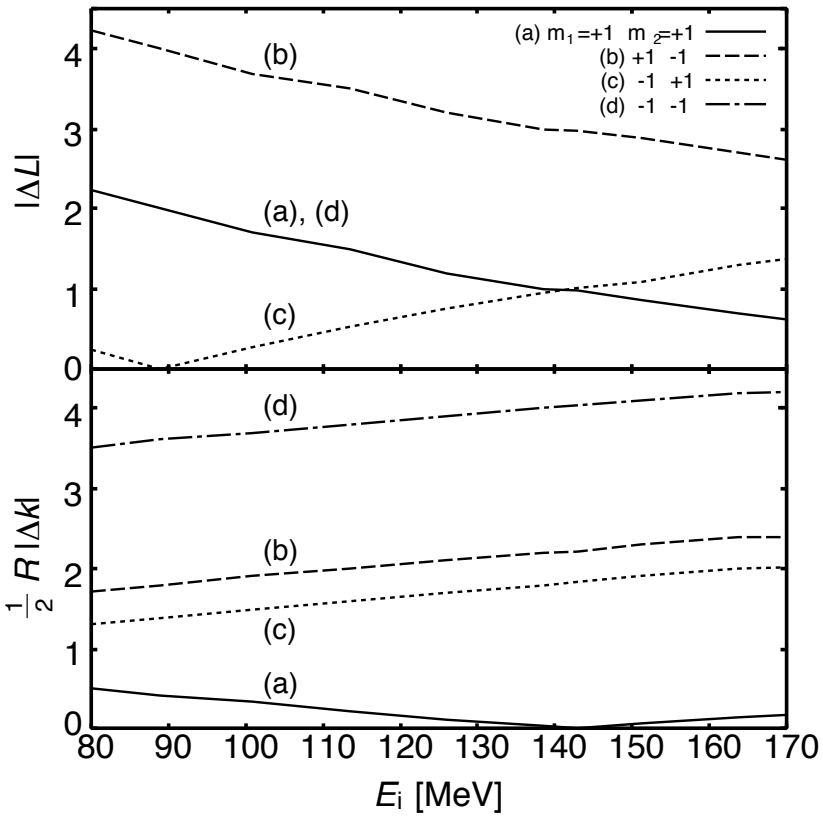

Fig. 5.11 Dependence of $|\Delta k|$ and $|\Delta L|$ on the incident energy $E_{\rm i}$ of ^{18}O, evaluated according to Eqs. (5.1) and (5.2). The nuclear radius was evaluated assuming $1.4A^{1/3}$ fm and the Coulomb energy difference $\Delta V_c = -1.44(Z_1^{\rm f}Z_2^{\rm f} - Z_1^{\rm i}Z_2^{\rm i})/R$ MeV, where $Z_1^{\rm f}$, $Z_2^{\rm f}$ and $Z_1^{\rm i}$, $Z_2^{\rm i}$ are the proton numbers for the nuclei in the final and initial states, and $R = R_1 + R_2$. (a) The transfer from $m_1 = +1$ to $m_2 = +1$, (b) from +1 to -1, (c) from -1 to +1 and (d) from -1 to -1.

5.5 Summary

We produce the spin-polarized ^{17}N beam via the inverse-kinematics low-energy transfer reaction, and investigate the momentum-acceptance and the emission-acceptance dependence of the polarization. The sign of the polarization of the ^{17}N turns out to agree with that evaluated by considering the Brink's matching conditions. Meanwhile, in spite of the emission angle the obtained polarization $|P|$ is 0.4 %, which looks like rather small. The calculation based on the Brink's matching condition shows the possibility to rise $|P|$ as the energy of the primary beam increases.

Chapter 6

Conclusion

Our motivation toward studies presented has been study of structure of unstable nuclei with nuclear moments. The studies mean development, measurement, discussion and application. There is no standard combination between production methods of unstable nuclei and spin polarization and measurement methods of nuclear moments. Therefore, we have needed to select various production and measurement methods in accordance to the goals.

Nuclear moment of Radioactive Isotope (RI) in a relatively light-mass neutron-rich region can be measured using combination of projectile fragmentation and β-ray-detected Nuclear Magnetic Resonance (β-NMR). As presented in Chap. 2, a spin-polarized ^{33}Al beam was produced using the fragment separator LISE, and an electric quadrupole moment of ^{33}Al was measured by β-NMR (β-NQR). Thus, possible evolution of nuclear structure around ^{33}Al was investigated by comparing the electric quadrupole moment obtained with theoretical predictions. We will continue to measure nuclear moments of the other nuclei in or around an *island of inversion*, and to investigate the nuclear structure of the *island of inversion*.

We have developed Tohoku RF-IGISOL which is an isotope separator on-line producing unstable nuclei located in an A = 100–130 neutron-rich region by proton-induced fission reaction. A measurement method of nuclear moment with Tohoku RF-IGISOL is γ-PAC which uses an anisotropic angular correlation between directions of emission of two γ-rays due to unstable nuclei with no orientation of spins. As described in Chap. 3, the half-life of the excited state in ^{105}Ru was measured in the preparation work for the magnetic-moment measurement by γ-PAC, and a SextuPole Ion-Guide (SPIG) has been installed in order to increase yields of unstable nuclei. We will promote the improvement of Tohoku RF-IGISOL as well as development of new magnetic-moment measuring method such as cross-polarization β-NMR and atomic beam resonance method described in Chap. 4. γ-PAC is the most versatile measurement method for nuclear moment of an excited state in this region, but can not be applied for a nuclear moment of a ground state. In contrast with that, those methods can be applied for the ground-state moment.

Tohoku RF-IGISOL has simpler composition than that of other production methods, because it mainly needs a proton beam accelerated by an AVF cyclotron, an uranium target and a mass separator comprised of a dipole magnet, while, for example, BigRIPS needs four accelerators including a huge superconducting ring cyclotron, long beam line and many magnets. It means that its operation cost in a process of producing unstable nuclei is lower. A reaction used in both BigRIPS and Tohoku RF-

IGISOL is the fission of uranium, but its arrangement is different whether in inverse-kinematics or in normal-kinematics. Because of this difference, shorter life unstable nuclei located in farther from stability, namely along the drip line, are able to be produced using BigRIPS. Due to the cost and the production ability, experiment using BigRIPS including measurement and development is apt to be performed for the nuclei located in farther from stability. Meanwhile, in the case of Tohoku RF-IGISOL we can not study such unstable nuclei, but we can often get opportunity of a beam time. In addition, most of nuclear moments to be measured are widely distributed in area between the stable line and the drip line, not only along the drip line, as presented in Fig. 1.1. Systematic study of nuclear moments located from the stable line to the drip line is important, as discussed the evolution of nuclear structure around ^{33}Al in Chap. 2. Thus, we will complement systematic measurements of the nuclear moments using Tohoku RF-IGISOL.

The RIABR is an extension of the Rabi resonance method for unstable nuclei and has an advantage over the β-NMR method for it does not require a spin-polarized RI. It provides a new and powerful method to measure nuclear moments of unstable nuclei produced using not only IGISOL but also a projectile-fragment separator. The RIABR apparatus is conveniently divided into a neutral atomic beam source of unstable nuclei and an Rabi resonance apparatus. Present status of the atomic beam source is still under development as presented in Chap. 4. In this development we again realize that such development requires a basis made of huge amount of knowledge, technique and experience of ISOL, especially IGISOL. Thus, it will be synergistically combined with development of IGISOL. Whereas, there is need of reconstruction of a versatile atomic beam resonance apparatus for heavy nuclei. Because atomic beam resonance apparatuses working today are specialized for each purpose, *e.g.* a spin-polarized proton target in a scattering experiment and a device precisely measuring magnetic moment of unstable alkali nuclei. Therefore, the development has just begun.

New scheme of producing spin-polarized RI ^{17}N via the inverse-kinematics reaction has been developed for application of the spin-polarized RI beam to condensed matter physics including impurity and electronic dynamics in semiconductors, as presented in Chap. 5. The polarization obtained currently looks like rather small, so that we have to find condition in which the polarization increases.

List of Figures

List of Tables

Bibliography

[1] M. Wada *et al.*, Nucl. Instrum. Methods Phys. Res., Sect. **B**, **204**, pp. 570–581 (2003).

[2] T. Sonoda *et al.*, Hyperfine Interact., **216**, pp. 103–107 (2013).

[3] T. Kubo *et al.*, Nucl. Instrum. Methods Phys. Res., Sect. **B**, **70**, pp. 309–319 (1992).

[4] T. Kubo, Nucl. Instrum. Methods Phys. Res., Sect. **B**, **204**, pp. 97–113 (2003).

[5] N. Stone: "Table of Nuclear Magnetic Dipole and Electric Quadrupole Moments", Vol. INDC(NDS)-0594, International Nuclear Data Committee, International Atomic Energy Agency (2011).

[6] E. K. Warburton, J. A. Becker, B. A. Brown, Phys. Rev. **C**, **41**, pp. 1147–1166 (1990).

[7] D. Troltenier *et al.*, Z. Phys. **A**, **338**, pp. 261–270 (1991).

[8] G. Lhersonneau *et al.*, Eur. Phys. J. **A**, **1**, pp. 285–297 (1998).

[9] P. Himpe *et al.*, Phys. Lett. **B**, **643**, pp. 257–262 (2006).

[10] A. Morton *et al.*, Phys. Lett. **B**, **544**, pp. 274–279 (2002).

[11] V. Tripathi *et al.*, Phys. Rev. Lett., **101**, p. 142504 (2008).

[12] C. Thibault *et al.*, Phys. Rev. **C**, **12**, pp. 644–657 (1975).

[13] C. Détraz *et al.*, Nucl. Phys. **A**, **394**, pp. 378–386 (1983).

[14] M. Yamagami, N. Van Giai, Phys. Rev. **C**, **69**, p. 034301 (2004).

[15] N. Hinohara *et al.*, arXiv:1109.2060v1 [nucl-th] (2011).

[16] K. Shimada *et al.*, Phys. Lett. **B**, **714**, pp. 246–250 (2012).

[17] K. Sugimoto *et al.*, J. Phys. Soc. Jpn., **21**, pp. 213–221 (1966).

[18] K. Asahi *et al.*, Phys. Lett. **B**, **251**, pp. 488–492 (1990).

[19] H. Okuno *et al.*, Phys. Lett. **B**, **335**, pp. 29–34 (1994).

[20] J. Ärje *et al.*, Phys. Rev. Lett., **54**, pp. 99–101 (1985).

[21] J. Ärje *et al.*, Nucl. Instrum. Methods Phys. Res., Sect. **A**, **247**, pp. 431–437 (1986).

[22] T. Sonoda: "RF イオンガイド式オンライン質量分離装置による中重核領域中性子

過剰核の研究", PhD thesis, Tohoku University (2002).

[23] T. Sonoda *et al.*, Nucl. Instrum. Methods Phys. Res., Sect. **B**, **254**, pp. 295–299 (2007).

[24] Y. Miyashita: "RF-IGISOL による中性子過剰な中重核領域の核磁気モーメントの測定", PhD thesis, Tohoku University (2008).

[25] Y. Miyashita *et al.*, Nucl. Instrum. Methods Phys. Res., Sect. **B**, **266**, p. 4498 (2008).

[26] M. Tanigaki *et al.*, Phys. Rev. **C**, **80**, p. 034304 (2009).

[27] H. J. Xu *et al.*, Nucl. Instrum. Methods Phys. Res., Sect. **A**, **333**, pp. 274–281 (1993).

[28] I. I. Rabi *et al.*, Phys. Rev., **53**, p. 318 (1938).

[29] I. I. Rabi *et al.*, Phys. Rev., **55**, p. 526 (1939).

[30] N. F. Ramsey: "Molecular beams", Oxford University Press (1956).

[31] C. Détraz *et al.*, Phys. Rev. **C**, **19**, pp. 164–176 (1979).

[32] D. Guillemaud-Mueller *et al.*, Nucl. Phys. **A**, **426**, pp. 37–76 (1984).

[33] T. Motobayashi *et al.*, Phys. Lett. **B**, **346**, pp. 9–14 (1995).

[34] G. Huber *et al.*, Phys. Rev. **C**, **18**, pp. 2342–2354 (1978).

[35] D. T. Yordanov *et al.*, Phys. Rev. Lett., **99**, p. 212501 (2007).

[36] P. J. Woods *et al.*, Phys. Lett. **B**, **182**, pp. 297–300 (1986).

[37] N. Orr *et al.*, Phys. Lett. **B**, **258**, pp. 29–34 (1991).

[38] D. Borremans *et al.*, Phys. Lett. **B**, **537**, pp. 45–50 (2002).

[39] H. Ueno *et al.*, Phys. Lett. **B**, **615**, pp. 186–192 (2005).

[40] P. Himpe *et al.*, Phys. Lett. **B**, **658**, pp. 203–208 (2008).

[41] D. Nagae *et al.*, Phys. Rev. **C**, **79**, p. 027301 (2009).

[42] D. Kameda *et al.*, Phys. Lett. **B**, **647**, pp. 93–97 (2007).

[43] M. De Rydt *et al.*, Phys. Lett. **B**, **678**, pp. 344–349 (2009).

[44] M. De Rydt *et al.*, Nucl. Instrum. Methods Phys. Res., Sect. **A**, **612**, pp. 112–121 (2009).

[45] A. Abragam: "The Principle of Nuclear Magnetism", Clarendon, Oxford (1961).

[46] D. Nagae *et al.*, Nucl. Instrum. Methods Phys. Res., Sect. **B**, **266**, pp. 4612–4615 (2008).

[47] P. Endt, Nucl. Phys. **A**, **633**, pp. 1–220 (1998).

[48] R. Brun, F. Carminati: "CERN application software group, geant3.2, CERN program library, writeup report no. w5013, 1994." (1994).

[49] V. Kellö *et al.*, Chem. Phys. Lett., **304**, pp. 414–422 (1999).

[50] S. J. Gravina, P. J. Bray, J. Magn. Reson., **89**, pp. 515–521 (1990).

[51] B. Wildenthal, Progress in Particle and Nuclear Physics, **11**, pp. 5–51 (1984).

[52] Y. Utsuno *et al.*, Phys. Rev. **C**, **60**, p. 054315 (1999).

[53] B. Brown, B. Wildenthal, Nucl. Phys. **A**, **474**, pp. 290–306 (1987).

[54] Y. Utsuno *et al.*, Phys. Rev. **C**, **70**, p. 044307 (2004).

[55] H. Ogawa *et al.*, Phys. Rev. **C**, **67**, p. 064308 (2003).

[56] A. Bohr, B. R. Mottelson: "Nuclear Structure", Vol. II, B.R. World Scientific, Singapore (1998).

[57] W. A. Richter, S. Mkhize, B. A. Brown, Phys. Rev. **C**, **78**, p. 064302 (2008).

[58] K. Yoshida, Phys. Rev. **C**, **79**, p. 054303 (2009).

[59] J. Äystö, Nucl. Phys. **A**, **693**, pp. 477–494 (2001).

[60] H. Miyatake: "$T_z = -\frac{1}{2}$ 核 ^{57}Cu の崩壊と fp 殻領域の鏡像 β 転移の研究", PhD thesis, Tohoku University (1984).

[61] T. Shinozuka *et al.*, Phys. Rev. **C**, **30**, pp. 2111–2114 (1984).

[62] H. Hama: "$f_{7/2}$ 殻 $T_z = -\frac{1}{2}$ 原子核の半減期の精密測定による鏡像ベータ転移の研究", PhD thesis, Tohoku University (1986).

[63] M. Yoshii: "イオンガイド式オンライン質量分離装置の製作とそれによる ^{57}Cu の半減期測定", PhD thesis, Tohoku University (1986).

[64] M. Yoshii *et al.*, Nucl. Instrum. Methods Phys. Res., Sect. **B**, **26**, pp. 410–418 (1987).

[65] M. Tanikawa *et al.*, Z. Phys. **A**, **347**, pp. 53–62 (1993).

[66] H. Kudo *et al.*, Nucl. Instrum. Methods Phys. Res., Sect. **B**, **126**, pp. 209–212 (1997).

[67] H. Kudo *et al.*, Phys. Rev. **C**, **57**, pp. 178–188 (1998).

[68] M. Wada: "イオントラップとレーザー分光法による ^{87}Sr の超微細構造の研究", PhD thesis, Tohoku University (1992).

[69] H. Sunaoshi: "イオントラップとレーザー・マイクロ波二重共鳴法による Sr^+ の超微細構造の研究", PhD thesis, Tohoku University (1994).

[70] A. Ozawa *et al.*, Phys. Rev. Lett., **84**, pp. 5493–5495 (2000).

[71] R. Kanungo, I. Tanihata, A. Ozawa, Phys. Lett. **B**, **528**, pp. 58–64 (2002).

[72] K. Wisshak *et al.*, Nucl. Instrum. Methods Phys. Res., Sect. **A**, **292**, pp. 595–618 (1990).

[73] R. E. Holland, F. J. Lynch, B. D. Belt, Phys. Rev. **C**, **17**, pp. 2076–2079 (1978).

[74] L. S. Kisslinger, R. A. Sorensen, Rev. Mod. Phys., **35**, pp. 853–915 (1963).

[75] R. A. Sorensen, Phys. Rev., **133**, pp. B281–B284 (1964).

[76] H. H. Güven, B. Kardon, H. Seyfarth, Z. Phys. **A**, **287**, pp. 271–285 (1978).
[77] R. Schuhmann, C. Hohenemser, Phys. Rev. **C**, **33**, pp. 2176–2178 (1986).
[78] B. Hinfurtner, E. Hagn, E. Zech, Nucl. Phys. **A**, **509**, pp. 541–549 (1990).
[79] E. Matthias, S. S. Rosenblum, D. A. Shirley, Phys. Rev., **139**, pp. B532–B539 (1965).
[80] J. Huikari *et al.*, Nucl. Instrum. Methods Phys. Res., Sect. **B**, **222**, pp. 632–652 (2004).
[81] S. Izumi *et al.*, CYRIC Annual Report 2009, pp. 19–21 (2010).
[82] H. Okuno *et al.*, Phys. Lett. **B**, **354**, pp. 41–45 (1995).
[83] H. Ueno *et al.*, Phys. Rev. **C**, **53**, p. 53 (1996).
[84] H. Izumi *et al.*, Phys. Lett. **B**, **366**, pp. 51–55 (1996).
[85] H. Ogawa *et al.*, Phys. Lett. **B**, **451**, pp. 11–18 (1999).
[86] W. J. Hiller, W.-D. Schmidt-Ott, Nucl. Instr. and Meth., **139**, pp. 331–333 (1976).
[87] K. Halbach, Nucl. Instr. and Meth., **169**, pp. 1–10 (1980).
[88] Vector Field, Ltd., UK: "OPERA-2d and OPERA-3d/TOSCA".
[89] The Los Alamos Accelerator Code Group: "Poisson Superfish".
[90] A. Yoshimi *et al.*, AIP Conf. Proc., **915**, pp. 849–852 (2007).
[91] T. Sugimoto *et al.*, Hyperfine Interact., **181**, pp. 141–144 (2008).
[92] L. Loeb: "Basic Processes of Gaseous Electronics", University of California Press, Berkeley and Los Angeles (1955).
[93] D. Nagae *et al.*, Physica **E**, **29**, pp. 580–583 (2005).
[94] M. Tanaka *et al.*, Nucl. Phys. **A**, **263**, pp. 1–11 (1976).
[95] Y. Yamamoto, K.-I. Kubo, Phys. Rev. **C**, **49**, pp. 360–371 (1994).
[96] D. Brink, Phys. Lett. **B**, **40**, pp. 37–40 (1972).
[97] M. Ishihara *et al.*, Phys. Lett. **B**, **73**, pp. 281–283 (1978).
[98] K. H. Tanaka *et al.*, Phys. Rev. **C**, **34**, pp. 580–593 (1986).
[99] Y. Yanagisawa *et al.*, Nucl. Instrum. Methods Phys. Res., Sect. **A**, **539**, pp. 74–83 (2005).
[100] K. Sugimoto *et al.*, Phys. Lett., **18**, pp. 38–39 (1965).
[101] K. Matsuta *et al.*, Phys. Rev. Lett., **86**, pp. 3735–3738 (2001).

Acknowledgment

First of all, I would like to thank everyone and every apparatus that interact me, and interaction between you and I.

I am most grateful to Professor Koichiro Asahi at Tokyo Institute of Technology and Professor Tsutomu Shinozuka at Cyclotron and Radioisotope Center, Tohoku University (CYRIC) for their insightful advice, constructive comments and continuous encouragement. Without their persistent help this thesis would not have materialized. I am very glad to have been able to study their knowledge, technology and experience. However, I could study and understand only a part of them as presented in this thesis and a track of my researches. I have to continue to study them if I hold a doctorate.

I would particularly like to thank my examiners, Professor Yasuhiro Sakemi at CYRIC, and Professor Hirokazu Tamura, Professor Kazushige Maeda, and Professor Toshio Kobayashi at Tohoku University who give insightful comments and suggestions during the examination, one and a half years, patiently.

I extraordinarily acknowledge Dr. Hideki Ueno who always shows me attitude of a genuine scientist for the nature, namely *"Never Give Up"*. Without his support the works would not have been possible.

I would like to express my gratitude to the following collaborators for their great help in the work described in Chap. 2: Dr. H. Ueno, Dr. T. Nagatomo, Professor A. Yoshimi, Dr. Y. Ichikawa, Dr. D. Kameda, Dr. E. Yagi (*RIKEN*), Professor G. Neyens, Dr. M. Depuydt, Dr. M. De Rydt, Dr. W. Vanderheijden, Dr. N. Vermeulen, Dr. P. Vingerhoets (*KU Leuven*), Professor K. Asahi, Ms. Y. Hasama (*Tokyo Institute of Technology*), Professor D. L. Balabanski (*Institute for Nuclear Research and Nuclear Energy, Bulgarian Academy of Sciences*), Dr. J. M. Daugas, Dr. L. Gaudefroy, Dr. P. Morel (*CEA*), Dr. S. Grévy, Dr. Ch. Stodel, Dr. J.-C. Thomas (*Grand Accélérateur National d'Ions Lourds (GANIL)*), Dr. L. Perrot (*Institut de Physique Nucléaire d'Orsay*), Dr. Y. Utsuno (*Japan Atomic Energy Agency*), and Dr. K. Yoshida (*Niigata University*).

I also thank the staff of GANIL for their support during the experiment. I appreciate the β-NMR apparatus, LISE and the accelerator at GANIL. This work was partly supported by the JSPS KAKENHI (22340071), by the JSPS and MAEE under the Japan-France Integrated Action Program (SAKURA), by the French-Japanese International Associated Laboratory for Nuclear Structure Problems (LIA), and also financed by the European Community FP6-Structuring the ERA-Integrated Infrastructure Initiative contract EURONS No. RII3-CT-2004-506065, by the FWO-Vlaanderen, by the IAP-programme of the Belgium Science Policy under grand number P6/23, and by Bulgarian National Science Fund, grant No. DID-02/16. The shell model calculations were carried out by using the program OXBASH coded by Professor B.A. Brown *et al*.

I am indebted to the following collaborators and staffs for their invaluable support in the work described in Chap. 3: Professor T. Shinozuka, Dr. T. Wakui (*CYRIC*), Dr. Y. Miyashita, Dr. N. Sato, Ms. S. Hoshino, Ms. M. Tateoka, Ms. A. Sasaki, Mr. H. Ouchi, Ms. S. Izumi, Ms. M. Takahashi, Mr. Hiroto Ueno (*Tohoku University*), Dr. M. Tanigaki (*KUR*), Dr. M. Wada, Dr. T. Sonoda (*RIKEN*), Mr. S. Chiba, Mr. Y. Ohmiya, Mr. N. Takahashi, Mr. S. Yokokawa, Mr. J. Suzuki, and Mr. K. Takahashi (*SHI Accelerator Service Ltd.*). I also appreciate the staff at CYRIC for their support. I thank Tohoku RF-IGISOL and the accelerator at CYRIC.

I would like to express my gratitude to the following collaborators for their generous help in the work described in Chap. 4: Professor K. Asahi, Mr. H. Miyoshi, Dr. D. Nagae (*Tokyo Institute of Technology*), Dr. H. Ueno, Professor A. Yoshimi, Dr. T. Sugimoto (*RIKEN*), Professor J. Murata, Dr. H. Kawamura (*Rikkyo University*), Dr. H. Ogawa (*National Institute of Advanced Industrial Science and Technology*), Dr. D. Kameda, Mr. J. Kaihara, Dr. T. Ito, Mr. S. Suda, Mr. S. Emori, Mr. G. Kato, Mr. G. Kijima, Mr. M. Tsukui, Mr. M. Takemura, Mr. T. Arai (*Tokyo Institute of Technology*), Professor Y. Kobayashi, Professor W. Sato, Professor H. Watanabe (*RIKEN*), and Professor W.-D. Schmidt-Ott (*Universität Göttingen*). I also thank the staff at RIKEN accelerator research facility and CYRIC for their support during the experiment. I thank RIPS, the accelerators and the all pieces of RIABR apparatuses. I acknowledge the help of Junior Research Associate scholarship from RIKEN (JRA). This work was supported by President's Special Research Grant of RIKEN.

My heartfelt appreciation goes to the following collaborators for their invaluable help in the work described in Chap. 5: Professor K. Asahi, Dr. D. Nagae, Mr. T. Arai, Mr. M. Takemura, Dr. T. Inoue, Mr. K. Takase, Mr. S. Kagami, Mr. N. Hatakeyama,

Ms. Y. Hasama, Mr. Y. Kurihara, Ms. C. Nakano, Dr. K. Suzuki (*Tokyo Institute of Technology*), Professor S. Kubono, Dr. H. Yamaguchi, Dr. Y. Wakabayashi, Mr. G. Amadio, Dr. S. Hayakawa (*CNS*), Professor J. Murata, Dr. H. Kawamura, Mr. T. Toyoda, (*Rikkyo University*), Dr. H. Ueno, Professor A. Yoshimi, Dr. T. Sugimoto, Dr. D. Kameda, and Dr. T. Nagatomo (*RIKEN*). I also thank the staff at CNS and RIKEN accelerator research facility for their support during the experiment. I thank the β-NMR apparatus, CRIB and the accelerator at RIKEN. I acknowledge the help of JRA. This work is supported by the JSPS Core-to-Core Program.

I also thank researchers, students and staffs around me: Dr. T. Okada, Ms. S. Sumita, Ms. M. Sumita, Ms. S. Umebayashi, Dr. K. Yoneda, Dr. N. Imai (*RIKEN*), Professor T. Nakamura, Dr. Y. Kondo, Dr. Y. Sato, Dr. K. Sakai (*Tokyo Institute of Technology*), Professor H. Okamura, Dr. M. Ito, Dr. H. Yoshida, Dr. K. Harada, Dr. T. Furukawa, Mr. T. Nagano, Mr. T. Takahashi, Mr. T. Hayamizu, Mr. A. Oikawa, Mr. T. Kato, Mr. T. Sato, Ms. S. Ezure, Mr. T. Ishikawa, Mr. Y. Arikawa, Mr. H. Kato, Mr. S. Ando, Ms. A. Uchiyama, Mr. T. Aoki, Mr. K. Sakamoto (*CYRIC*), Professor T. Koike, Dr. M. Ukai, Dr. T. Yamamoto (*Tohoku University*), Dr. H. H. Bertschat (*Hahn-Meitner-Institut*), Professor K. Hatanaka, and Professor M. Fukuda (*RCNP*). I thank Dr. K. Kawasaki and Van de Graaff at Tokyo Institute of Technology.

There are many persons who I have to acknowledge, because I spent long time for these works and had been supported by them. There is someone who I miss writing above, so I apologize it, and please remember my acknowledge for him or her is never changed.

Finally, I would like to express the deepest appreciation to my parents for their continuous encouragement and supports. This thesis is dedicated to them.

Osaka, November 2014 *Kenzi Shimada*